Thermochemical Conversion of Biomass: A Molecular Viewpoint

by

AnGayle Konstance Vasiliou

B.A., Wheaton College, 2005

A thesis submitted to the

Faculty of the Graduate School of the

University of Colorado in partial fulfillment

of the requirements for the degree of

Doctor of Philosophy

Department of Chemistry and Biochemistry

2011

This thesis entitled:

Thermochemical Conversion of Biomass to Biofuels: A Molecular Viewpoint

Written by AnGayle K. Vasiliou

has been approved for the Physical Chemistry program by

_____

Prof. G. Barney Ellison

_____

Prof. Veronica Bierbaum

Date: _____

The final copy of this thesis has been examined by both the signatories, and we find that both the content and the form meet acceptable presentation standards of scholarly work in the above mentioned discipline.

Vasiliou, AnGayle K. (Ph.D. Physical Chemistry)

Thermochemical Conversion of Biomass to Biofuels: A Molecular Viewpoint

Thesis directed by Professor G. Barney Ellison

This dissertation describes experiments performed to study the thermal decomposition of biomass from a molecular viewpoint. The structure of biomass consists of three major parts: cellulose, hemicellulose and lignin. Thermochemical conversion of biomass, specifically pyrolysis and gasification, yields a complex mixture of light gases, condensable vapors and aromatic tars. The goal for the gasification of biomass is to maximize the production of syngas (CO and H_2) and minimize the production of aromatic tars. This thesis provides thermochemical information particularly related to cellulose decomposition.

The current technology for the conversion of biomass to biofuels is hindered by the lack of fundamental knowledge concerning detailed mechanisms and kinetic parameters that govern the process. In order to approach this problem, this work provides such information for furan, furfural, acetaldehyde and propionaldehyde, known intermediates in the pyrolysis of cellulose.

The thermal decomposition of the aforementioned biomass molecules was formed in a microtubular reactor with pressures of 75-100 torr and up to temperatures of 1700 K corresponding to residence times of roughly 30-100 μs in the heated reactor. The biomass molecules were entrained in the carrier gases He or Ar and passed through the reactor. The thermal decomposition of the molecules occurs during transit through the heated reactor and products are cooled upon expansion into a vacuum chamber. The pyrolysis product beam was interrogated by three unique schemes: Photoionization Time of Flight Mass Spectroscopy (PIMS) using 10.5 eV light, Matrix Isolation Infrared (IR) Spectroscopy and PIMS using tunable

vacuum ultraviolet (VUV) radiation at the chemical dynamics beamline of the Advanced Light Source located at Lawrence Berkley National Laboratory in Berkley, CA. Unlike previous studies of biomass decomposition, these experiments were able to identify the initial pyrolysis products.

The first half of this thesis will deal with the thermal decomposition pathways and kinetics of furan and furfural. Earlier G2(MP2) electronic structure calculations predicted that furan will thermally decompose to acetylene, ketene, carbon monoxide, and propyne at lower temperatures. At higher temperatures, these calculations forecast that propargyl radical could result. We see all these products as well as the formation of aromatic hydrocarbons at higher concentrations. This is the first study to show radicals present in biomass decomposition. Thermal decomposition of furfural generates furan and thus follows the same mechanistic pathways as described above.

The second half of this manuscript details the thermal decomposition of acetaldehyde and three isotopologues CH_3CDO, CD_3CHO and CD_3CDO as well as benzaldehyde. As thermal decomposition products of CH_3CHO, we have identified CH_3 (PIMS), CO (IR, PIMS), H (PIMS), H_2 (PIMS), CH_2CO (IR, PIMS), CH_2=CHOH (IR, PIMS) and HCCH (IR, PIMS). The mechanism for decomposition of benzaldehyde is analogous to that of furfural with appropriate products.

The results in this thesis have reveled detailed mechanisms in the pyrolysis of biomass. These mechanisms can serve as the foundation for examining the thermal decomposition of biomass from a molecular perceptive. The conversion mechanisms that were observed will aid in the overall design of future gasifiers that produce clean syngas.

Dedicated to my parents,

You give more than one heart can handle

Thank You

Acknowledgements

I have spent almost seven years living and working in Boulder. It would be impossible to acknowledge all the people that have helped me over the years. I apologize if I miss anyone.

I first want to thank my thesis committee. Professor Veronica Bierbaum, Dr. Mark Nimlos, Dr. Donald David, Professor John Daily and Professor G.Barney Ellison.

My thesis committee has not only provided me with academic advice over the years but also served as mentors and role models. Veronica Bierbaum was one of the first people I met when I made the long trip from the east coast out to Colorado. She has served as my mentor and her kindness, brilliance and sense of humor never ceases to amaze me. I hope that I can be half the scientist she is one day. I have had the great pleasure of working with the best experimental scientist I have known in Mark Nimlos. I spent a large majority of my time early in graduate school working with Mark at NREL and learned more than I'll ever remember from him. I also owe Mark a lot of credit for my current ski skills. When I arrived in Boulder I had never been on a pair of skis but with all the group ski trips to Mark's condo in Monarch, I learned to leave my mark on the slopes. (Still don't love moguls as much as Mark but maybe I'll get there one day.) The Don, as I like to call him, has saved my instrument on more occasions than can be counted. I learned more from Don about experimental science than I could have asked for. He was always available for any question or problem I had and without a doubt was able to help me out. I can say with complete confidence that Don makes baklava as good as any Greek I know. It wasn't until a little later in graduate school that I met John Daily but he has taught me so much about "how things work" with his engineering expertise. He always pushed me to think about problems

like a chemist and like an engineer, a valuable skill that makes me a stronger scientist upon finishing my degree. I also had the privilege to get to know John on our trips out to the ALS where he showed me the best places in Berkeley to get a good cheese puff. Thanks John, I gained 5 lbs on those trips.

G.Barney Ellison. Barney, well not sure what I could possibly say that would sum up how much you mean to me. I know you hate the mushy and the thank you part of every talk but you have been the central force in making me the scientist and person I am today. I learned more asking you questions over the years than I ever learned in the classroom. You conduct yourself in the world of science in a way that others in the community should take a lesson from. All I can say is thank you and even though I am leaving the Ellison lab, you will never really be able to get rid of me because I will look to you for advice long into the future.

I can't say enough about the interaction and opportunity that working at CU provides. I learned so much from Dr. Carl Lineberger, Dr, Veronica Bierbaum, Dr. Mathias Weber, Dr. Veronica Vaida, Professor Charles DePuy and their research groups past and present.

I also have had the privilege of having many collaborators during my time in graduate school, which has helped me along the way. I thank them all but especially must thank Professor John Stanton for all his helpful discussions and advice.

I would like to thank the CIRES machine shop who were always available for advice or an emergency fix. Ken Smith, Jim Kastengren and Craig Joy thank you for all your help. I also must acknowledge everyone in the chemistry stockroom as well as the chemistry staff.

I also would like to thank Dr. Mark Jarvis, Dr. David Robichaud, Dr. Calvin Mukarakate, Professor Tony Dean and Dr, Hans-Heinrich Carstensen all of whom I met through my work at NREL.

The Ellison lab redefines the relationship between co-workers and friends. Every person I have worked with over the years has been a valuable asset in my intellectual growth but also in personal growth over the years. When I entered the lab Dr. Alan Maccarone and Dr. Xu Zhang took me under their wings and taught me everything they could about the Matrix; I could not have asked for better teachers. Dr. Tim D'Andrea, you always had time for a question no matter how busy you were. You always made me laugh and became a great friend over the years. Dr. Krzysztof "The Pole" Piech, what can I say about you my crazy friend. The lab was just not the same after you left. It was so quiet. You are one of my favorite people in the world and I learned so much from you during your time in Boulder. You always made me laugh and I will never forget NY with all my favorite BFFs. Luis Cuadra-Rodriguez, once you graduated and moved to CA, it was like an era had ended in the Ellison lab. I leaned on you more than you could know over the years. You are so kind and generous and I am honored to call you my friend. It was a pleasure and privilege to work with you. A special thanks to Dr. Stephanie Villano and Dr. Nicole Eyet for their guidance in the early days of graduate school.

The current Ellison lab members, you are the most amazing group of people I know. Beth Reed Adam Scheer, Jong Hyun, Kim Urness and Tom Ormond. Adam we started graduate school around the same time and I enjoyed working with you over the years. I know that you will do great things in the future and climb many mountains. Tom, I have no doubt that you will be a great experimentalist and do amazing research. You have the talent and drive to be very successful in the world of science. I wish you all the best luck on your future research. Jong, better known as Jonger. Your presence in lab is enough to cheer anyone up on a bad day. You have become a great friend over the years, and I have been honored to watch you and your family grow over the years. You work so hard in lab and taught me so much over the years. Kim, the lab is in great hands with you. Your Type-A personality has amazed me over the years. I know you are going to do great science in the next few years. You're smart, humble, and inquisitive, all qualities, which I admire in you. I can't thank you enough for all the science you helped me with. I could always count on you as a fellow lab mate and more importantly a friend. Our fearless post-doc, Beth, you are amazing and have been more help to me while writing my thesis than I have words for. From when I met you back in Davis to date you have become a great friend. Thank you for always being there for me. You are one of the strongest people I have met and I love all the talks we have enjoyed together.

My time in Boulder has been unforgettable. I have met lifelong friends that I am so grateful for. Thank you Michelle, Sarah Amy G., Jess, Galen, Brenna, Patty, Amy S., Steve, Alex, Javier, Carolynn, Paul, Scott, Rachelle, David, J'aime, Kirsten, Orli, Phil, Bennifer, Alison, Aly, Jenny Nicole C., Leticia and all the others I may have forgotten. I view your friendship as my greatest, accomplishment.

I wouldn't be here if it weren't for my family. My whole life you have been a driving force of love that made me think I could accomplish anything. My siblings, Missy, Gretchen, William- our relationship is a gift I am thankful for everyday. Each of us different and unique in our own way but the same in how much we appreciate and love each other. I look to you for advice and guidance and I am so proud to have you as my best friends. Uncle Billy, it was you that took me out on walks and showed me how beautiful nature is. If not for these walks I might have never found my love of science and the great outdoors. Thank you.

Mom and Dad, I dedicated the thesis to you- I think that about sums it up! Mom, you are the strongest women I know and have showed me what it means to persevere and succeed. You have always been my role model. Dad, what is there to say, your little girl with curl is all grown up. You have pushed me to be my best since I can remember and never let me give up. You have a solution to ever problem and never hesitate to listen and give me advice. You both have encouraged my "free spirit" personality even when it was driving you both a little crazy. I love you so much.

The greatest experience I have had in Colorado is meeting my future husband, Logan. When I moved out here almost seven years ago, I never thought I would find my prince. Logan, you are my world and I love you more than I can express with words. I can't imagine going forward with all of life adventures without you. I'm excited to share all the moments of the future with my one and only.

Lastly, I want to acknowledge all those that have moved on, that helped make me the person I am today.

Table of Contents

List of Tables

List of Figures

Chapter I

Introduction

1.1 Background

Biomass is the most likely renewable energy source for liquid transportation fuel to significantly replace existing fossil based fuels. Consequently there is a growing interest in using lignocellulosic materials as feedstock for the production of biofuels. The European Union has developed a plan[1] in which one-fourth of its transportation fuel would be derived from biofuels by 2030. Likewise, the United States Department of Energy has a vision[2] for producing 30% of the US transportation fuel from biomass. In order to reach these ambitious goals, it is likely that a variety of technologies will need to be developed. Further, technologies that can utilize a variety of feedstocks (agricultural residues, forest residues, energy crops, municipal waste, etc.) will be necessary.

For the reasons explained above thermochemical conversion technologies in particular gasification combined with catalytic fuel synthesis is worth strong consideration. In this approach, biomass is gasified at reduced pressures to produce primarily molecular hydrogen and carbon monoxide better known as syngas. A complete picture of the gasification process can be seen in Figure 1.1. Unfortunately, gasification/fuel synthesis using biomass has proved more difficult than initially thought because of the greater production of tars, which can deactivate the catalysts

used for synthesis. As a result, expensive gas clean up steps are required to prepare the syngas for catalytic conversion. A second approach would involve designing the gasification step so that fewer tars are produced. In order for this second approach to be feasible the chemical mechanisms and kinetics that lead to the formation of tars must be better understood.

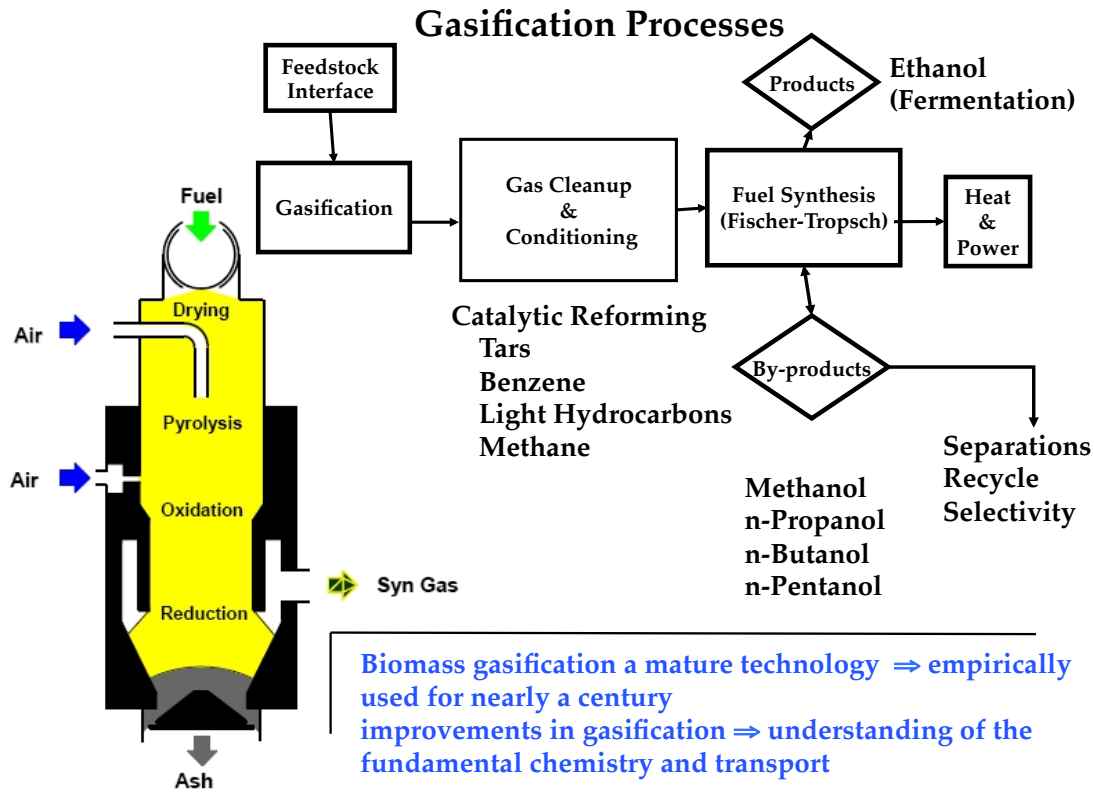

Figure 1.1 Overview of the gasification Process.

Since polysaccharides make up the bulk of biomass, the mechanisms of their decomposition and conversion to tars is of great importance in gasification. Many of these polymers such as cellulose or hemilcellulose, decompose to sugars, furans, furfural and aldehydes. This mixture of "primary" pyrolysis products can then further crack to form aromatic species. However the mechanisms and kinetics of these reactions are hugely unknown. Cellulose is a polymer of glucose (1,4-β-D-glucopyranose). The major idea of biomass gasification is to find conditions where the polysaccharides can be thermally decomposed to mostly yield H_2 and CO.

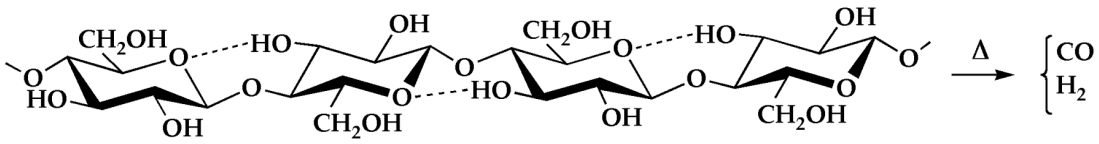

This is a complicated process and this work aims to tackle the chemical mechanisms that are involved.

Previous research[3-5] has observed that the pyrolysis of cellulose leads to the production of levoglucosan (1,6-anhydroglucopyranose), as well furans, furfurals and other aldehydes. This process is shown in Figure 1.2. It is believed that the cleavage of cellulose chains results in the formation of levoglucosan. This monosaccharide then rearranges and dehydrates to produce furan, furfural and 5-hydroxymethylfurfural. This is a conjectured pathway and the microscopic steps are unknown.

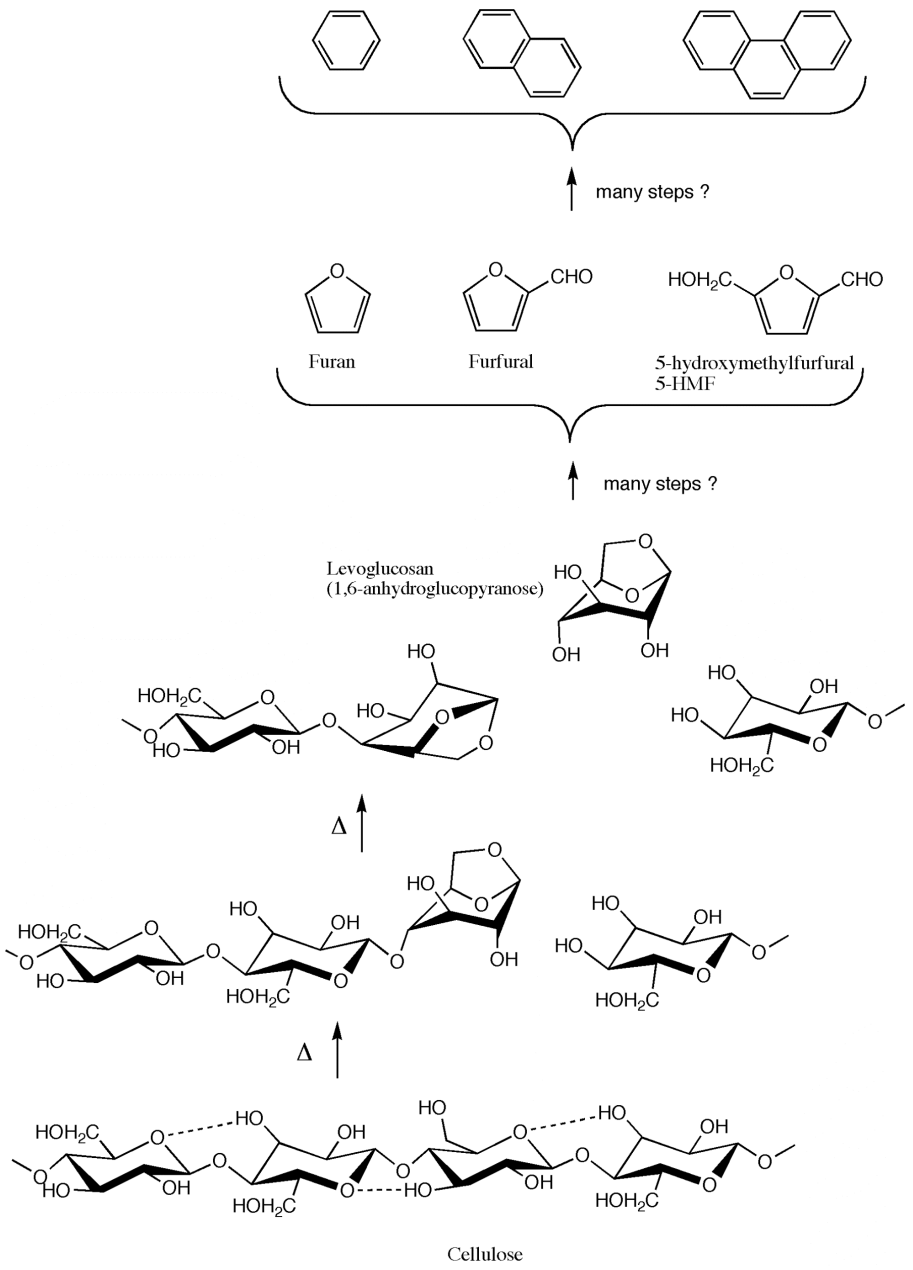

Figure 1.2 A schematic sketch of predicted thermal decomposition of Cellulose

1.2 Introduction to Biomass Gasification

Biomass gasification is a mature technology that has been empirically used for nearly a century. Thermochemical processing[6-8] is used to convert solid biomass into clean liquid fuels

and chemicals. Biomass is plant material such as agricultural crops, trees, and grasses. Composed of the structural polymers cellulose, hemicellulose, and lignin, along with a variety of volatile compounds called extractives, biomass provides a significant source of hydrocarbons. Cellulose and hemicellulose are polymers of sugars. Lignin is a three dimensional polymer of phenolic ethers. Thermochemical processing involves heating the feedstock under controlled conditions. The three main approaches are direct combustion for heat generation, gasification to generate syngas, and pyrolysis used to produce liquids. (Here the term pyrolysis is used as the industrial meaning as the process that produces liquids. The normal definition is heating in the absence of oxygen and that will be our use henceforth.) One aspect that all thermal methods share is the use of heat to break the chemical bonds of the large structural biopolymers into smaller semi-volatile or volatile units and char.[9,10] Heating first raises the feedstock to the boiling temperature of liquid water, which must be completely vaporized before further heating occurs. As the temperature rises above about 500 K, thermal decomposition begins to occur. The gaseous decomposition products are then driven to the surface and become available to react in the gas phase. The physical problem of heating, drying, and pyrolyzing is extremely complex. It involves conduction and convection in porous media, decomposition chemistry and subsequent gas phase chemistry. There are also possible catalyst effects as the gaseous products flow through already charred outer layers of the solid. Local heating rates can vary by several orders of magnitude. Biomass heating results in a mix of gaseous volatile compounds and semi-volatile compounds that liquefy into tars and solid char. It has long been the goal of those studying thermochemical processing to be able to predict both the primary decomposition products and their subsequent reaction chemistry. But no experiments to date have been able to resolve the chemistry on a time scale and with speciation accuracy that would provide detailed kinetics

information. As a result, workers who have studied the decomposition kinetics have been forced to settle for developing simple global mechanisms. An example of this often cited in the literature is the Diebold mechanism[11] for cellulose.

Diebold's Cellulose Decomposition Scheme

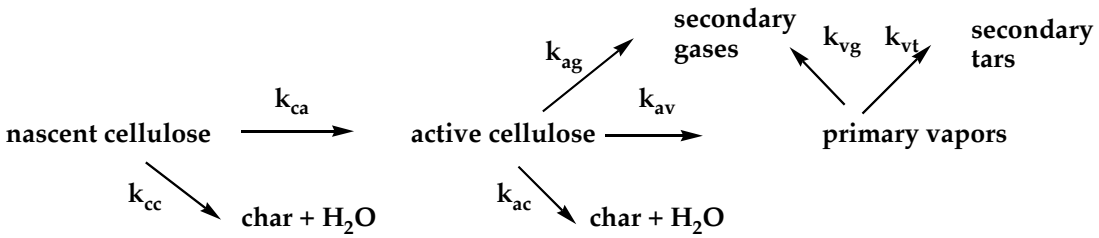

This model and other similar mechanism constitute the current state of the art.[10,12]

Cellulose which makes up 40-50% by mass of biomass is a linear polymer of cellobiose (1,4-dimer of glucopyranose). The sugars long chains that then cross link via weaker hydrogen bonding.[13,14] The cross-links break readily upon heating. In the literature the term "activated cellulose" has been described as the state where most of the bonds have been broken. Upon further heating 1,4-β-glycosidic linkages between glucose molecules begin to break, as well as other bonds producing a large spectrum of compounds. The Diebold mechanism and others like it can be used to estimate overall decomposition rates. In Figure 1.3 the mass fraction verses time for the species identified by the Diebold model are shown. In this model the initial stock is converted to active cellulose in about 10 μsec. The mirotubular reactor is able to examine the

thermal decomposition products on timescales of μs, which allows us to get a first look at the decomposition products. The rate limiting steps are then conversions from the active form into stable gases, semi-volatiles that subsequently condense to tars and chars.

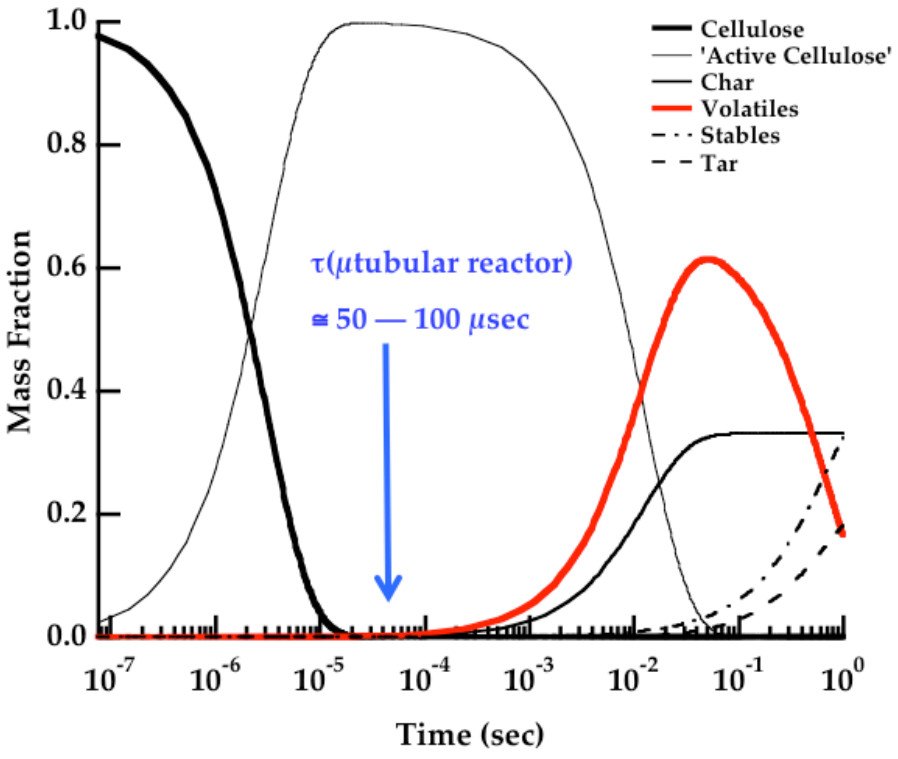

Figure 1.3 A simulation of the Kinetics of biomass decomposition

1.3 Scope of Thesis

This thesis details the laboratory studies of furan, furfural, benzaldehyde and acetaldehyde. Three techniques were used to study the thermal decomposition of each molecule. The thermal decomposition for each molecule is discussed in detail as well as subsequent products.

Chapter II describes the pyrolysis source to thermally decompose each molecule, as well as each experimental method that was used to probe products formed after pyrolysis. Chapters III, IV and V describe in detail the thermal decomposition pathways and conclusions from furan, furfural, benzaldehyde and acetaldehyde.

References for Chapter I

(1) Biofuels in the European Union: *A Vision for 2030 and Beyond*; **2006**.

(2) In U. S. Department of Energy, Office of the Biomass Program (OBP) 30 x 30 Workshop, http://www.30x30workshop.biomass.govtools.us/, L'Enfant PlazaHotel, Washington, D. C., August 1-2, **2006**; L'Enfant Plaza Hotel, Washington, D. C., August 1-2, 2006.

(3) Evans, R. J.; Milne, T. A.; Soltys, M. N. *Journal of Analytical and Applied Pyrolysis,* **1986**, *9*, 207.

(4) Evans, R. J.; Milne, T. A. *Energy & Fuels*, **1987**, *1*, 123.

(5) Evans, R. J.; Milne, T. A. *Energy & Fuels*, **1987**, *1*, 311.

(6) *A Survey of Biomass Gasification*; Reed, T. B., Ed.; Solar Energy Research Institute: Golden, CO, 1979; Vol. **II** *Principles of Gasification*.

(7) Bridgewater, A. V. *Fuel* **1995**, *74*, 631.

(8) Yaman, S. *Energy Conversion and Management* **2004**, *45*, 651.

(9) Shafizadeh, F. *J. Anal. Appl. Pyrolysis* **1982**, *3*, 283.

(10) Antal, M. J.; Varhegyi, G.; Jakab, E. *Ind. Eng. Chem. Res.* **1998**, *37*, 1267.

(11) Diebold, J. P. *Biomass & Bioenergy* **1994**, *7*, 75.

(12) Antal, M. J.; Varhegyi, G. *Ind. Eng. Chem. Res.* **1995**, *34*, 703.

(13) O'Sullivan, A. C. *Cellulose* **1997**, *4*, 173.

(14) Matthews, J. F.; Skopec, C. E.; Mason, P. E.; Zuccato, P.; Torget, R. W.; Sugiyama, J.; Himmel, M. E.; Brady, J. W. *Carbohydr. Res.* **2006**, *341*, 138.

Chapter II

Experimental

2.1 Introduction

The ultimate goal of the research was to study the thermal decomposition pathways for furan furfural, benzaldehyde and acetaldehyde. In all studies the thermal decomposition was done in a microtubular reactor or hyperthermal nozzle or simply nozzle, that thermally dissociates the precursor in a supersonic jet. The experimental details of the nozzle will be described in detail later, as well as the three primary techniques used to probe the molecular beam: photoionization time-of-flight mass spectrometry (PIMS) using 10.5 eV light, matrix isolation spectrometry and PIMS using tunable vacuum ultraviolet (VUV) radiation at the chemical dynamics beamline at the advanced light source. A secondary technique that will also be discussed in brief is Resonance Enhanced Multiphoton Ionization or REMPI used in analysis of benzaldehyde.

2.2 Microtubular Reactor

The microtubular reactor is used for the thermal decomposition of molecules. The current design is an elaborate recreation of the original design by Peter Chen[1]. The reactor can be interfaced with a photonionzation time-of-flight mass spectrometer (TOF), REMPI or helium cooled cryostat for matrix isolation studies [2]. All products of thermal decomposition then can be analyzed through the mass spectra and vibrational spectra produced.

One of the benefits of the reactor is the short residence times which allows us to eliminate problems one might face in traditional vacuum pyrolysis experiments,[3,4] such as secondary reactions. Since often we produce radicals in thermal decomposition experiments, it is important to reduce secondary reactions as much as possible. The two main types of secondary reactions that we want to avoid are recombination and disproportionation. Recombination reactions involve two radicals coming together to form a closed shell species:

$$Cl\bullet + Cl\bullet \rightarrow Cl\text{-}Cl \text{ or } R\bullet + R\bullet \rightarrow R\text{-}R.$$

In general the internal energy gained by new bond formation is removed through a collision with the rare gas. Disproportionation reaction involves two radicals reacting to form two new thermodynamically stable products:

$CH_3\text{-}CH_2\bullet + CH_3\text{-}CH_2\bullet \rightarrow H_2C = CH_2 + CH_3 - CH_3$ or more generically

$R\bullet + R\bullet \rightarrow A + B$

If we consider the disappearance rate for the radical:

$$\frac{-d[R\bullet]}{2dt} = k^{II}[R\bullet]^2 \qquad \textbf{(2.1)}$$

where, k^{II} is defined as the bimolecular rate constant. Solving this differential equation with an initial concentration of $R\bullet = R_0$ where R_0 is initial number density of radicals at t = 0, leads to an expression for the half life of the radicals in the heated region of the reactor:

$$t_{\frac{1}{2}}(R\bullet) = \frac{1}{k^{II}[R_0]}$$

(2.2)

According to equations 2.1 and 2.2, producing more radicals makes them react faster. In general rate constants for radical-radical reactions are diffusion controlled. Recall that in traditional vacuum pyrolysis tube experiments the residence time is on the order of tens of ms to complete pyrolysis, which would allow the radicals too much time to react away. Our pyrolysis reactor has a much lower residence time, on the order of 50-100 μs, with about 10^{13} radicals per pulse which allows the radicals to exit the reactor and avoid secondary collisons.[2]

2.2.1 Reactor Description

The goal of the microtubular reactor is to thermally decompose the precursor molecule and produce a clean, sufficient source of desired products. The reactor achieves this by pulsing gases through a hot SiC tube at near supersonic velocities. Figure 2.1 shows a cross-sectional view of the reactor. A commercial solenoid valve (Parker Hannifin Series 9 General Valve) is mounted on a copper flange to eliminate heat transfer from hot SiC tube to valve. The heated portion of the SiC tube is 28 mm in length with an inner diameter (ID) of 1 mm and and outer diameter (OD) of 2mm. The SiC tube sits tightly in a drilled hole in the center of copper flange so that the valve orifice looks directly down the SiC tube. The back end of the valve is quarter inch stainless steel tubing that is attached to a manifold that provides the gas flow through pulsed valve into SiC tube. The SiC tube is resistively heated to temperatures up to 1700 K. The restive heating is provided through a pair of graphite discs, one at each end of tube with each clamped by a molybdenum clip. The molybdenum clips are each mounted to a copper wire. One end of

the wire is grounded while the other is attached to a variac. The SiC temperature is monitored using a Type C thermocouple from Omega (tungsten/rhenium 26% W in one wire and 5% W in the other wire) The Type C thermocouple is spot welded to a piece of tantalum foil, which is then wrapped around the SiC tube with tantalum wire. A Love controller is used to monitor the potential difference in the two thermocouple wires, which the controller than converts to a temperature reading. An alumina radiation shield encloses the SiC tube, thermocouple and other heating components. The alumina shield and components fit tightly into the copper flange mentioned above.

The entire reactor assembly then slides into a vacuum-sealed stainless steel cylinder (ID 35 mm and OD 45 mm) with a hollow wall for water-cooling. The housing cylinder and SiC tube are evacuated to approximately 10^{-6} Torr through the exit end of cylinder. This exit end of cylinder is mounted to the photoionization vacuum chamber in TOF experiments or to a cryostat vacuum shroud for matrix isolation experiments.

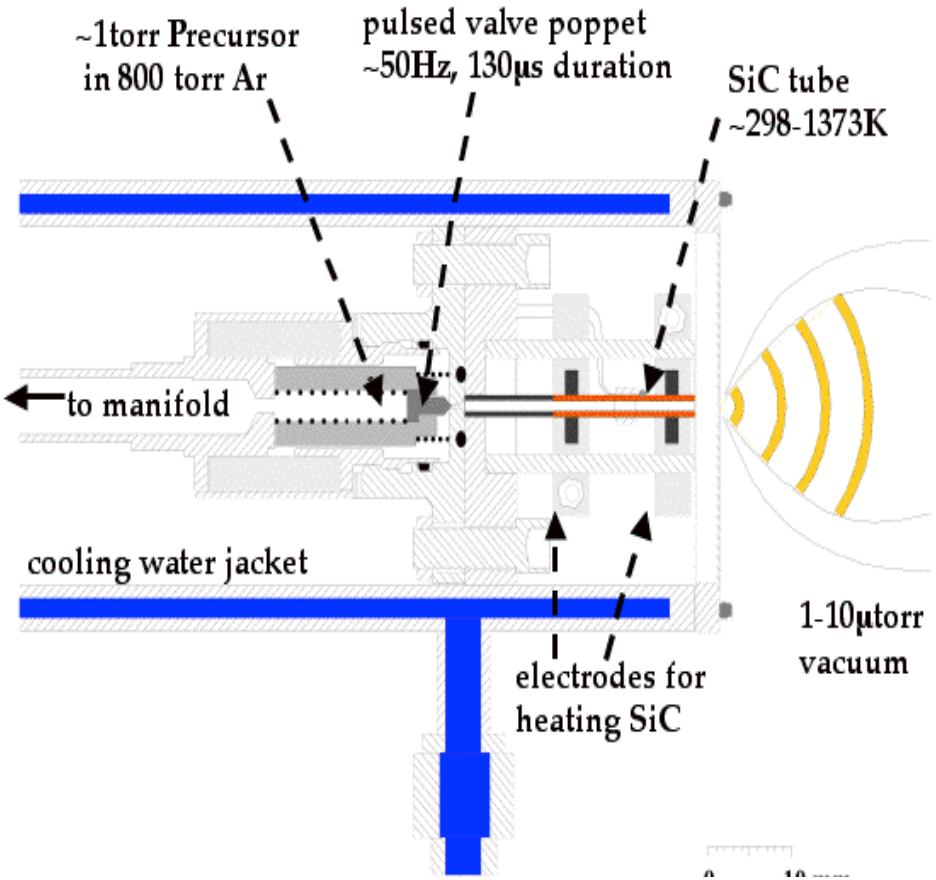

Figure 2.1 Cross Sectional schematic of reactor assembly

2.2.2 Description of Flow

The flow through the SiC tube has the following characteristics. As gas passes through the valve, it chokes at the valve orifice behind the poppet and then expands into the tubular reactor. The friction and heat transfer that occurs in the SiC tube also causes the flow to choke at the exit of the tube.[5] If we assume the flow within the tube is entirely within the continuum regime it can be described by the Navier-Stokes equations. Computational fluid dynamics (CFD) can be used to simulate the flow. Daily et al. have used CFD to model the flow specific to our reactor.[5] The CFD simulations indicate that there is a sonic plane near the exit of the reactor tube. Based on the temperature, pressure and velocity at the sonic plane, an estimate of the flow rate at the sonic plane can be made. The CFD simulations estimate a residence time for gases traveling through the SiC tube between 50-75 μs. As discussed in the previous section this is very important in order to avoid bimolecular collisions that quench desired thermal decomposition products.

The flow then exists the SiC tube into a vacuum chamber where it forms an under expanded jet. In the continuum limit the flow can be described in Fgure 2.2.[6] Along the centerline the flow is isentropic (zone of silence) until a strong shock wave, the Mach disk, is formed. In our specific case, the vacuum chamber is at such low pressures that the flow rapidly transitions into free molecular, or collisionless flow and a Mach disk never forms.

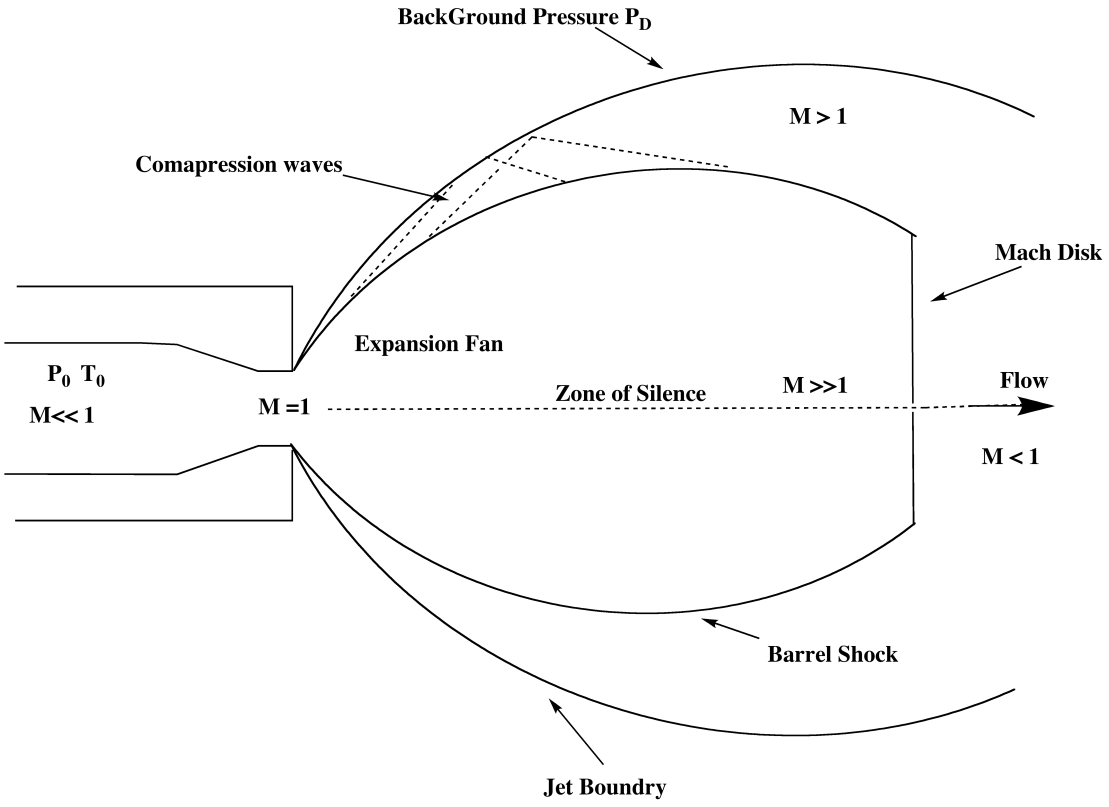

Figure 2.2 Supersonic Under expanded Jet[6]

In the continuum region of the expansion, one-dimensional isentropic relations can be used to define the temperature (T), Pressure (P) and density (n) along the streamline can be described as follows:[7]

$$\frac{T}{T_0} = \left(1 + \frac{\gamma - 1}{2} M^2\right)^{-\gamma/(\gamma-1)} \qquad \textbf{(2.3)}$$

$$\frac{P}{P_0} = \left(1 + \frac{\gamma - 1}{2} M^2\right)^{-\gamma/(\gamma-1)} \tag{2.4}$$

$$\frac{n}{n_0} = \left(1 + \frac{\gamma - 1}{2} M^2\right)^{-\gamma/(\gamma-1)} \tag{2.5}$$

where M is the Mach number defined as:

$$M \equiv \frac{V}{a} = \sqrt{\frac{V}{\gamma \frac{R}{W} T}} \tag{2.6}$$

α is local speed of sound, γ is the ratio of specific heats (C_p/C_V) and for ideal gases is known as the adiabatic constant. *V* is defined as the velocity, R is gas constant and W is molecular weight. P_0 and T_0 are the total or stagnation pressure and temperature, which are the values that P and T would have if the flow were isentropically decelerated to zero velocity. For a sharp edged orifice, these would be P and T in the upstream chamber. Conversely, in our case we must estimate their values using the isentropic relations. If for example, if the sonic plane temperature is 1500 K, the effective total temperature is 2000 K assuming argon in the carrier gas.

If we apply the first Law of Thermodynamics where h is the total enthalpy

$$h_0 = h + \frac{V^2}{2}$$

(2.7)

and introducing the specific heat at constant pressure ($c_p = (\gamma/\gamma - 1)R/W$), then

$$V = \sqrt{\frac{2R}{W}\left(\frac{\gamma}{\gamma - 1}\right)(T_0 - T)}$$

(2.8)

If $T_0 >> T$, then the velocity approaches an asymptotic limit.

$$V_\infty = \sqrt{\frac{2R}{W}\left(\frac{\gamma}{\gamma - 1}\right)T_0}$$

(2.9)

In order to exploit these relationships requires that the Mach number be known as a function of distance from the reactor exit. We can use the correlation,[8]

$$M = 1.0 + A\left(\frac{x}{d}\right)^2 + B\left(\frac{x}{d}\right)^3$$

(2.10)

for $0 > \left(\frac{x}{d}\right) > 1.0$, and

$$M = \left(\frac{x}{d}\right)^{\gamma-1}\left[C_1 + \frac{C_2}{\left(\frac{x}{d}\right)} + \frac{C_3}{\left(\frac{x}{d}\right)^2} + \frac{C_4}{\left(\frac{x}{d}\right)^3}\right]$$

(2.11)

for $\left(\frac{x}{d}\right) > 0.5$.

The empirical constants A, B and C can be found in Miller,[6] x is defined as the distance on centerline downstream of the SiC exit and d in our case is the orifice diameter of the SiC tube. It's important to note that Mach number is not a function of the thermodynamic state.

All the above relations are valid for continuum flow upstream of the Mach disk. An empirical relation for the location of the Mach disk is given by[9]:

$$\frac{x_M}{d} \cong 0.67\left(\frac{P_0}{P_D}\right)^{1/2}$$

(2.12)

where; P_D is the pressure in the vacuum chamber into which the expansion flows. For the PIMS and matrix experiment the typical pressure ratios (10^4–10^5 Torr), this expression predicts that in our instruments the Mach Disk is far from the SiC tube exit. This information is essential in order to know that we are probing the molecular beam within the continuum region before collisions within the beam can occur.

2.3 Photoionization Time of Flight Mass Spectrometry

Photoionization Time of Flight Mass Spectrometry (PIMS-TOF) is used to characterize and optimize the molecular beam exiting the SiC tube. The first step in a precursor is to determine the optimal temperature for thermal decomposition of a precursor that yields the highest concentration of products.

A mixture of the precursor gas in helium is prepared in a manifold and pulsed into the SiC tube. The molecular beam is then skimmed approximately 3-5 mm after exiting the SiC tube and then travels 40 cm downstream and intersects with a 10.49 eV (118.2 nm) laser beam generated by frequency tripling of the third harmonic (354.6 nm, 30 mJ/pulse) of a Nd:YAG. The molecular beam from the SiC tube intercepts the laser beam at a right angle. The tripling cell consist of a gas mixture of 4 Torr Xe/40 Torr Ar. All species in the molecular beam that have an ionization energy (IE) below 10.49 eV will be photoionized. In general most organic molecules have IEs below 10.49 eV; a few notable exceptions are CO, HCCH and major constituents of air: N_2, O_2, Ar and water. The new ions are injected by a positively biased repellar plate into the flight tube, and accelerated into the drift zone by a strong electric field. At the end of the flight tube, the ions are reflected back down to the detector by two positively biased reflector plates. The ion signal at the detector is recorded on an oscilloscope, which is interfaced to a computer. Many pulses (100-1,000) are needed to obtain a mass spectra with good signal-to-noise ratios. The flight tube is kept at a higher vacuum (10^{-7} Torr) then the remainder of PIMS instrument to prevent damage to ion optics. A schematic of the PIMS-TOF instrument can be seen in Figure 2.3.

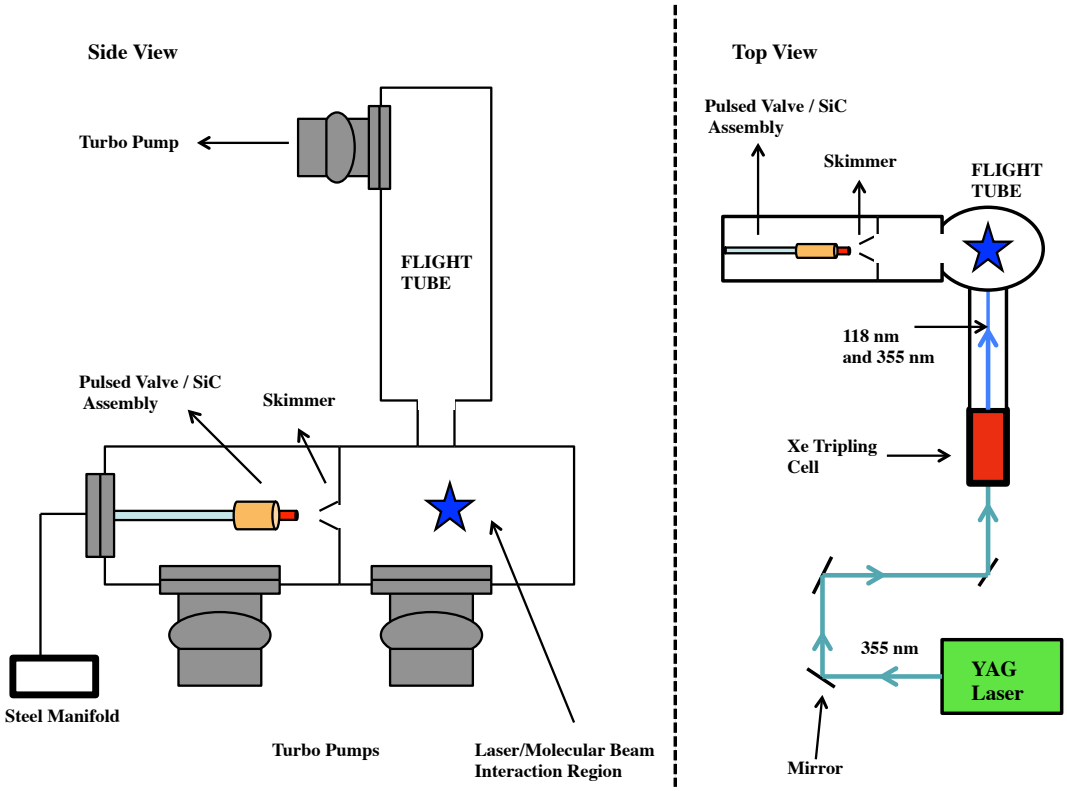

Figure 2.3 A schematic of PIMS-TOF experiment seen from side (left) and top (right) views. A gas mixture is prepared in the steel manifold then is pulsed through general valve into SiC tube. The gas pulse exits the SiC tube and passes through skimmer, then interacts with 10.49 eV laser beam shown as blue star in above figure. The newly generated ions are then accelerated and steered into the flight tube. The top view of PIMS-TOF experiment shows that has 335 nm light passes through tripling cell it is converted into 118 nm light.

2.3.1 Reflectron

A brief description of the reflectron is needed since it was used in both PIMS experiments in Colorado as well as experiments done at ALS. The basic principle of TOF spectrometry are based on energy conservations laws. Figure 2.4 is a schematic of the reflectron component in the time of flight tube. After the ions are created in the interaction region they are injected into the TOF chamber (Jordan TOF Products, Inc.) where a repeller plate (A1) with a positive bias accelerates the ions in the forward direction. The ions then travel through an extraction grid (A2), before passing through a final grounded plate (A3) into the flight chamber. The ions at this point have all been accelerated to the same kinetic energy. The ions then drift through the chamber until they reach a series of plates or reflectron where they are decelerated, turned around and reaccelerated. Once the ions leave the reflectron they travel toward the microchannel plate detector (MCP) biased at a negative voltage. The current that is created by ions at MCP is converted to voltage by an oscilloscope in order to monitor the signal. The above description does not describe the energy distribution that occurs in the reflectron; for this information refer to the instruction manual from Jordan TOF products, Inc.[10]

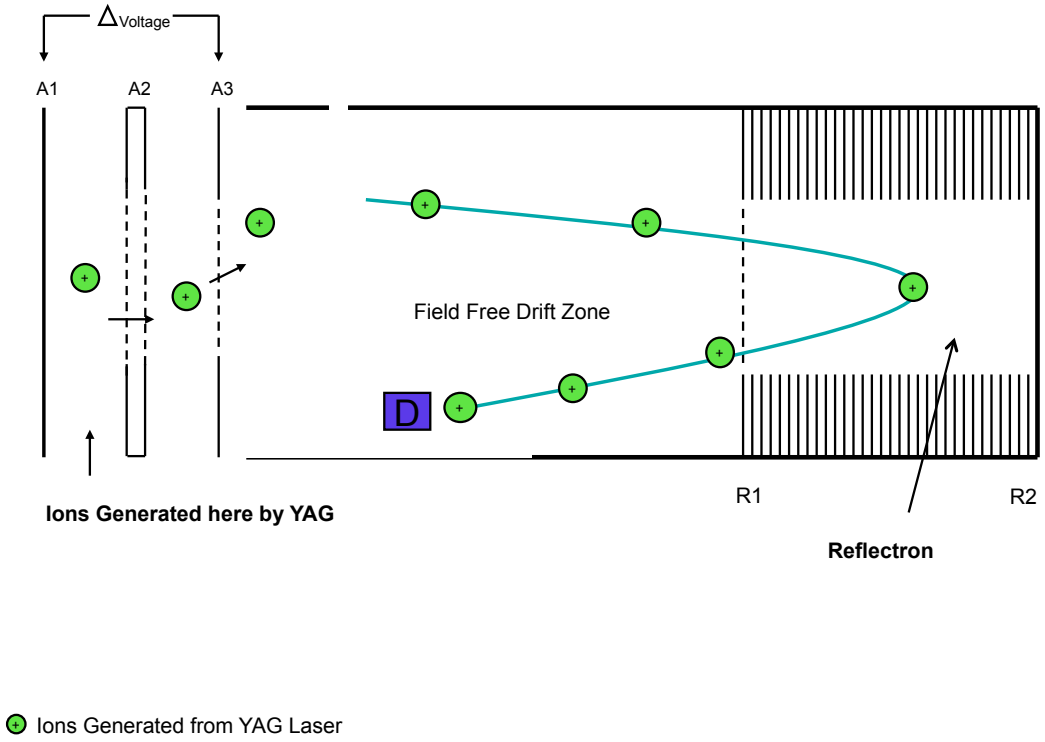

Figure 2.4 A schematic of the reflectron time of flight and interaction region. The ions are first accelerated by a positively biased repeller plate (A1) enter extraction grid (A2) where once exiting pas through final grounded plate (A3) into the drift chamber. The ions drift through chamber until they reach the reflectron where they are decelerated turned around and then re-accelerated toward MCP detector (D).

2.3.2 Time of Flight Theory

This section will discuss basic principles of time of flight mass spectrometry. Previous work provides a more in depth explanation and mathematical derivations than will be given in this work.[11] All TOF instruments share the simple idea that ions are accelerated to the same final energy down the flight tube and their arrival time reflect their mass.[12] There are three regions in a TOF experiment which are needed to derive an expression for flight time, t, in terms of mass to charge ratio: The first is the ionization region between the repeller plate (A1) and extraction grid (A2), the second region is between the extraction and final acceleration grid (A3), and the third is the drift region between ground plate (A3) and MCP detector. The total flight time can be defined as the sum of time spent in each individual region.

$$t = t_1 + t_2 + t_3 \tag{2.13}$$

The time spent in each individual region, t_1 , t_2 , and t_3 depends on the velocity and distance traveled by the ion. For example the velocity of ions leaving the first region, v_1 , depends on the voltage of the repeller plate, the mass to charge ratio of ions $\left(\frac{m}{q}\right)$, the distance the ions are created from the start of extraction grid and the initial velocity of ions. When the values for *t* in each region are known they can be substituted into equation 2.13, giving a relationship between $\left(\frac{m}{q}\right)$, and time:

$$\frac{m}{q} = At^2 \tag{2.14}$$

In equation 2.14 it is clear that a relationship between mass and time can be made. The constant A is a complicated parameter that optimizes the relationship between mass and time[12]. (Evans.)

2.4 Matrix Isolation

Discovered in George C Pimentel's lab in 1954, the matrix isolation technique has been widely used in many areas of research. As early as the 1950's matrix isolation was being developed as a valuable technique that could powerfully coupled with infrared spectroscopy, the same holds true today.[13]

A matrix can be described as a continuous solid phase in which desired molecules are embedded. The desired molecules are said to be isolated in the host matrix. All matrix experiments in this work use argon as the host matrix material and the desired species are frozen within the argon matrix, see Figure 2.4. Argon will not absorb in the IR, which means that only desirable absorbers will be detected using FTIR.

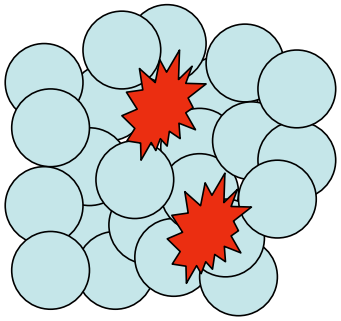

Figure 2.5 A cartoon of a typical matrix. The light blue represents the host argon atoms and the red represents trapped target molecules within the argon matrix. This cartoon is not to scale.

2.4.1 Matrix Isolation Instrument Design

The reactor housing is mounted to a vacuum shroud of a two-stage APD closed-cycle He cryostat, approximately 20 cm away from a CsI window, also known as the matrix window. A 1:1000 torr mixture of the precursor molecule to argon is prepared in a 1 L glass manifold. The manifold is connected to back of the vacuum-sealed stainless steel chamber housing the reactor and SiC tube. The valve controller (General Valve, Iota One) determines the dosing rate through the SiC tube. The pressure drop in the 1 L manifold is monitored by a capacitance manometer.

The matrix window (a 2.0 cm diameter and 4 mm thick CsI window) is mounted inside a stainless steel holder that screws into the cooling finger of the cryostat. The cold finger is reported to reach 10-20 K at maximum cooling.[14] A radiation shield is placed over the cold finger to prevent warming of the cold CsI window from both the heated SiC tube and room temperature vacuum chamber housing cold finger. The radiation shield has two opposing

openings facing the surface of the SiC window. These windows allow not only dosing from the SiC tube but also permit the IR light from a commercial FTIR spectrometer (Nicolet Magna 550) to penetrate matrix window. A schematic of the cryostat cold finger can be seen in Figure 2.6.

The cryostat includes two major parts: the cold finger as described above and a compressor. In the compressor section of the cryostat, ultra high purity helium is compressed then cooled using a heat exchanger.[14] A charcoal filter cleans the gas of both oil and moisture. The cooled He then flows from the compressor through stainless steel hoses into the cryostat that contains the cooling finger. The typical operating temperature for the cold finger is 30 K. Figure 2.7 is photo that contains both the cryostat head containing cold finger with reactor mounted and cryostat compressor positioned on the rolling blue cart.

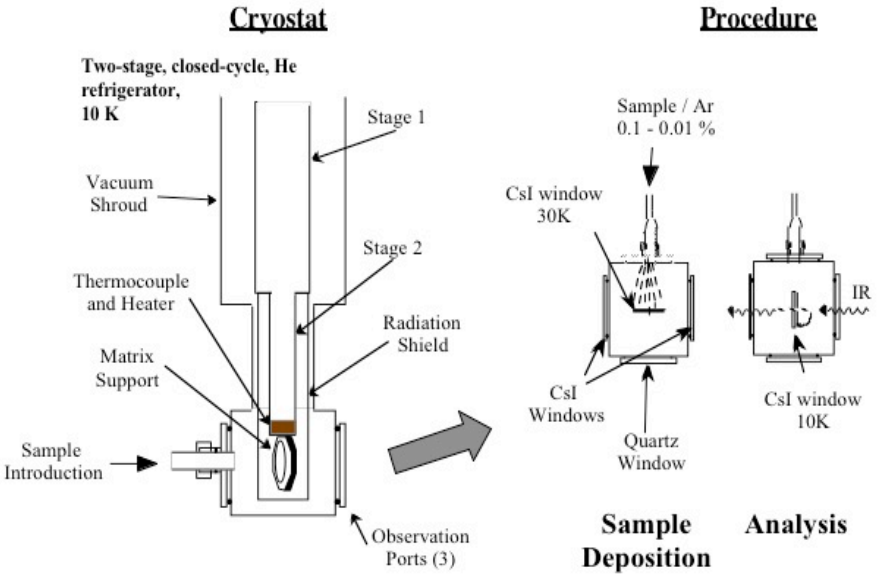

Figure 2.6 Schematic of thecold finger of cryostat and procedure for dosing and analyzing CsI window.

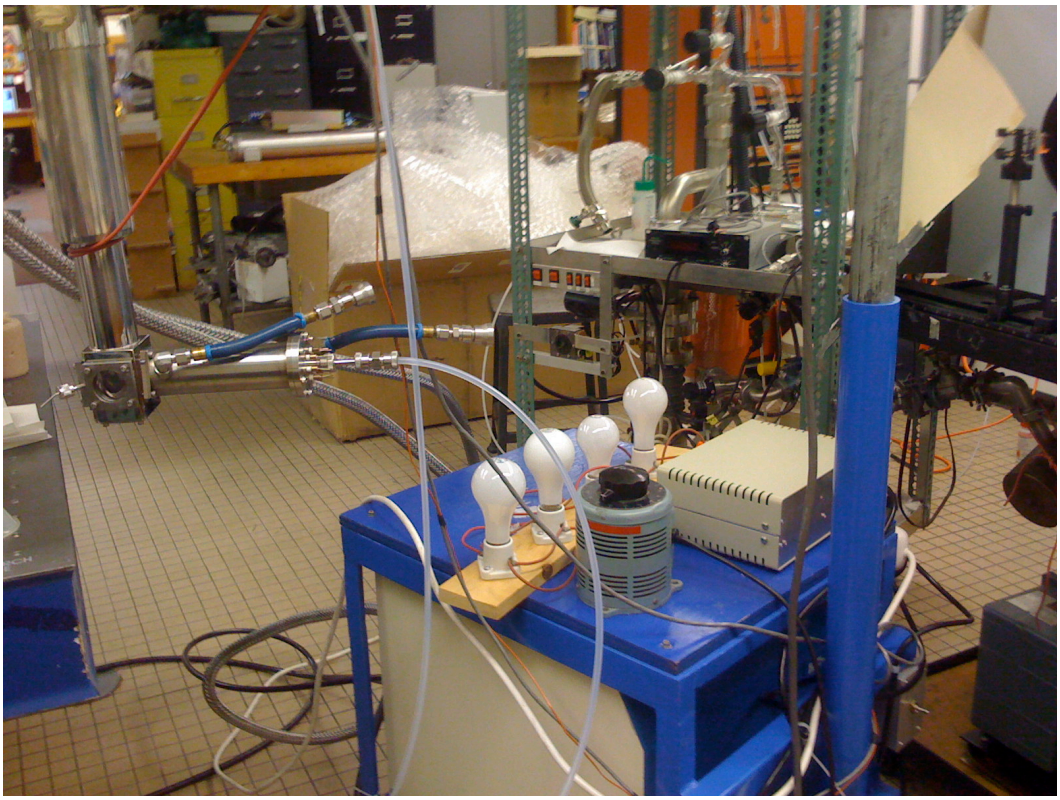

Figure 2.7 A photo of the reactor in the stainless housing mounted to the APD cryostat head containing the cold finger. Compressor piece of cryostat is mounted inside the rolling blue cart.

2.4.2 Fourier Transform Infrared Spectroscopy (FTIR)

Matrix isolation is coupled with FTIR in order to probe the molecular vibrations of target molecules in the matrix. The advantage to using a commercial FTIR is the accessibility of the mid-IR across a broad range (4000 to 500 cm^{-1}). It is the mid IR region of the electromagnetic spectrum where most molecular vibrations occur. No two molecules have identical infrared spectra, which makes FTIR a very favorable diagnostic tool in determining products from thermal decomposition of precursor molecules.

The commercial spectrometer used to analyze matrices operates on the principle of interferometry. This principle simply states that light has wave characteristics and multiple waves of light can interfere with each other both destructively and constructively. The major component of the spectrometer is the Michelson Interferometer, which is shown in Figure 2.8.

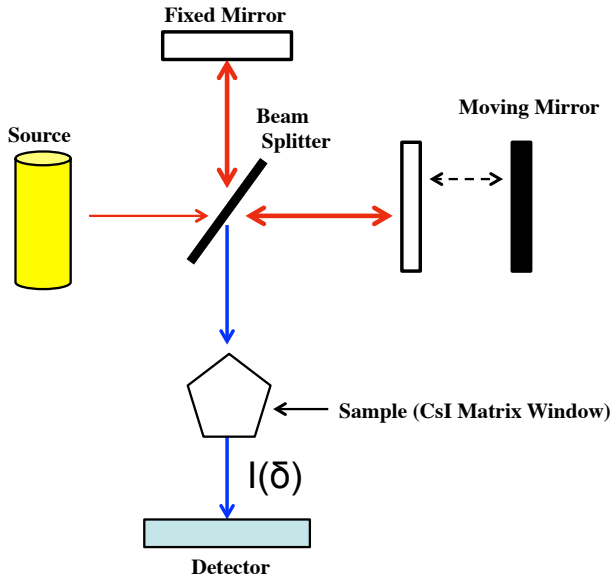

Figure 2.8 A schematic of the Michelson Interferometer in FTIR

The light from the source (a hot SiC rod) travels to a KBr beam splitter, where some light is reflected towards a moving mirror and some light transmitted towards the fixed mirror. The reflected and transmitted amount of light is determined by the properties of the beam splitter. Light incident on the moving mirror returns to the beamsplitter. The light that hit the fixed mirror is reflected back to the beamsplitter. The optical path difference of the two light beams can be defined as δ. Since the starting light is monochromatic the intensity of the two interfering light beams at the beamsplitter is:

$$I(\delta) = R(\sigma)\cos(2\pi\delta\sigma)$$

(2.15)

where R(σ) is a collection of parameters that describe Intensity and optical properties, σ is the wavenumber of light. To describe the actual situation, in which the hot SiC source approximates a blackbody emitter and produces many different frequencies, equation 2.15 needs to be integrated over all wavenumbers:

$$I(\delta) = \int_{-\infty}^{+\infty} R(\sigma)\cos(2\pi\delta\sigma)d\sigma$$

(2.16)

Equation 2.16 in its graphical would yield an interferogram and does not contain any useful spectral features. In order to produce the desired intensity vs. wavenumber spectrum equation 2.16 is Fourier transformed to give:

$$R(\delta) = \int_{-\infty}^{+\infty} I(\sigma)\cos(2\pi\delta\sigma)d\sigma$$

(2.17)

which now gives an expression that is more familiar, intensity as function of wavenumber.

When using FTIR as a diagnostic tool it is important to understand how weak an IR transition can be detected. Beer's law relates the path length (z), infrared cross section (σ), and the concentration of absorbers:

$$I(v) = I_0\,(v)e^{-n\sigma(v)z}$$

(2.18)

Where I_0 is the light intensity before the sample and I is the light intensity after passing through sample. The integrated IR intensity[15] commonly termed A, is defined as the integral of IR absorption cross section over the bandwidth:

$$A \equiv \int dv\sigma(v) = (nz)^{-1} \int dvln|I_0\,(v)/I(v)|$$

(2.19)

Commercial spectrometers such as the one used in this work measure optical density defined as:

$$OD(v) = log_{10}|I_0\,(v)/I(v)|$$

(2.20)

The most useful expression for the integrated IR intensity is:

$$A = \frac{\ln\,(10)}{nz} \int_{IR\ Band} dvOD(v)$$

(2.21)

where the IR signal is integrated over the bandwidth (cm^{-1}). A typical range for A values is 75 km mol^{-1} for strong transitions and 0.01 km mol^{-1} for weak transitions. If we consider an absorber with a small IR intensity of 0.05 km mol^{-1} and require a signal to noise ($s/n \propto n^{1/2}$) of 10, then the concentration of desired absorbers is:

$$n = \frac{(\frac{S}{n})\ln(10)}{Az} \int_{IR\ Band} dvOD(v)$$

(2.22)

A good approximation is that OD is not a function of *v* over the bandwidth of an IR transition. In the matrix the bandwidth is on the order of 1 cm^{-1}. Therefore equation 2.22 can be rewritten as:

$$n = \frac{(\frac{S}{n})\ln(10)}{Az} \Delta vOD$$

(2.23)

The detection limit of the FTIR spectrometer is on the order of 10^{-4} cm^{-1}; this is a measured value for ΔvOD.

Previous work[16-18] demonstrated that approximately 10^{18} desired absorbers or target molecules are deposited on the CsI window in one hour. The thickness of the matrix after one hour is estimated to be 0.02 cm resulting in a target molecule concentration of about 100 μmol cm^{-1}. A typical matrix experiment involves dosing over a 2-3 hour period. Since in one hour matrices of at least 0.01 cm thick are readily prepared, the required value for n is expected to be:

$$n = \frac{(\frac{S}{n})\ln(10)}{Az} \int_{IR\ Band} dvOD(v)$$

$$= \frac{10(\ln(10))}{\left(\frac{0.05km}{mol}\right)\left(10^5 \frac{cm}{km}\right)(10^{-2}\ cm)} (10^{-4})(6.02\ x10^{23} \frac{molecules}{mol})$$

(2.23)

Therefore we require a matrix at least 0.01 cm thick with a radical concentration of 50 μmol cm^{-1}, to detect a weak transition in our FTIR. As stated above, the minimum spectrometer requirements are easily met with our reactor.

2.5 Chemical Dynamics Beamline and Synchrotron Radiation

A large number of experiments done involving acetaldehyde were performed at the Advanced Light Source (ALS) located at the Lawrence Berkeley National Lab, in Berkeley, CA. The ALS is a third generation-synchrotron and a national user facility that is used by scientists around the world. The experiments done at the ALS were identical to the PIMS experiments done in Colorado except that instead of only one photon energy of 10.49 eV, the ALS provides "continuously" tunable VUV radiation with high photon fluxes from approximately 8 eV to above 20 eV. Most physical chemists are familiar with lasers, however fewer are acquainted with synchrotron light sources. The goal of this section is to give the reader a brief overview of how synchrotron radiation is generated. If a more detailed description is required the reader is directed to the ALS homepage: http://www-als.lbl.gov.

Synchrotron radiation is the name given to the radiation that occurs when

particles accelerate in a curved path or orbit. In a classical picture any particle that moves in a curved path or is accelerated in a straight path will emit electromagnetic radiation. The ALS synchrotron is known as an electron accelerator. The electrons are accelerated to 99.999994% the speed of light with a 1.9 GeV of energy. Figure 2.9 is an overview of the synchrotron at the ALS. The rest of this section will describe the important components of the synchrotron that produce electrons going nearly the speed of light with 1.9 GeV of energy.[19]

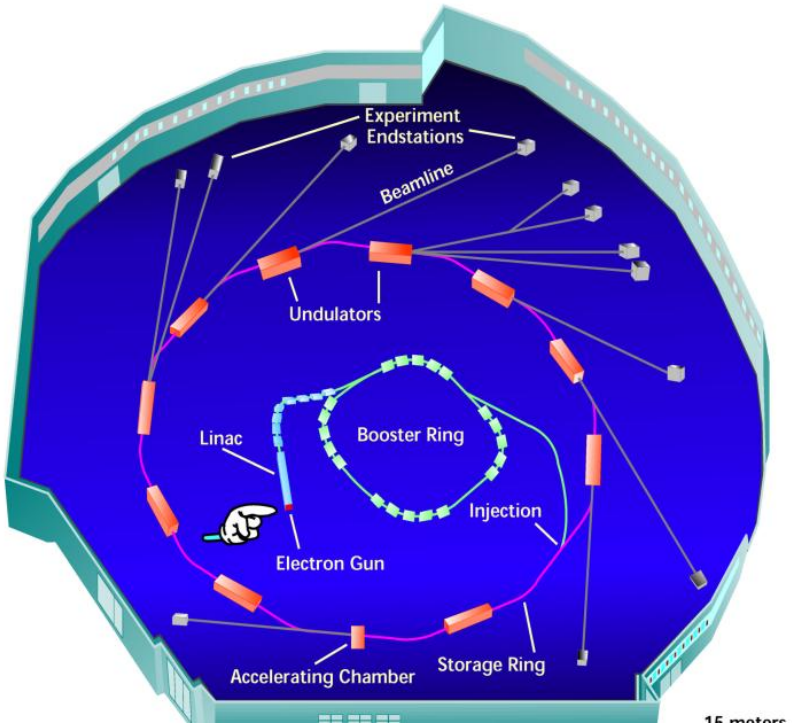

Figure 2.9 Overview of ALS syncrohtron[20]

The electrons start their journey at the electron gun and linac. The electron gun is a barium aluminate cathode, which emits electrons when heated. The electrons are then accelerated by the main anode to about 120 keV and enter the Linac or linear accelerator. The ALS linac is a traveling wave design, where the electrons can be thought of as "surfing" the electric field down

the linac. By the time the electrons reach the end of linac, they have a kinetic energy of 50 MeV, and are going nearly the speed of light. This is still less than 3% of the final energy of the electrons. The electrons will gain most of their energy in the booster ring.

The booster ring has two sections. The first section consists of quadruple magnets to keep the electron beam focused and dipole magnets, used to turn the electrons. As stated above, an accelerating electron gives off radiation (energy), so if the booster ring only had the two magnets the electron beam would lose energy, which is not desired. The second section of the booster ring, radio frequency cavity, fixes this problem. The radio frequency cavity or RF system, supplies the power to the ALS in the form of microwaves. A waveguide channels the power from a UHF transmitter providing about 30 kilowatts of RF power. It runs at 500 MH and has a peak voltage of 250 keV. This voltage is much lower than what is needed to accelerate electrons to their final energy of 1.5 GeV in one shot, but the ALS is a ring. A common analogy used at the ALS is a playground merry-go-round. To make it spin quickly, it could be given one great push or it could be given many small timed pushes. The RF cavity provides millions of small pushes per second. In this way the electrons attain an energy of 1.5 GeV. In the booster ring, the radiation losses make the electron lose about 100 keV per turn once they have 1.5 GeV of energy. The 250 keV that the RF cavity provides is more than enough to get the electron moving. Once the electrons reach an energy of 1. 5 GeV, which takes less one than second and the electrons have gone around the booster ring 1.3 million times, then are traveling at 99.999995 % the speed of light. The electrons are then ejected into the storage ring, the largest component of the ALS with a diameter of 63 meters.

The storage ring is very similar to the booster ring. In the storage ring the electrons are accelerated to 1.9 GeV using a pair of RF cavities working on the same principle as described in

the booster ring. The storage ring is not a circle but rather a dodecagon, with 12 straight sections, where insertion devices are placed.

The pair of RF cavities that keeps the electrons speeding around the ring occupies one of the straight sections in the storage ring. Another section is used for the injection of electrons from the booster ring to the storage ring. All other sections are occupied by insertion devices, which direct the electrons to each beamline at the ALS. Insertion devise can be thought of as the porthole, which allows scientists to access the electrons produced by the synchrotron. Beamline 9.0.2, the chemical dynamics beamline,[20] where the experiments on acetaldehyde were conducted, uses an undulator as an insertion device. The undulator uses multiple magnets arranged in a period structure to accelerate the electrons in a well-defined path, causing the emission of light. The undulator at beamline 9.0.2 is approximately 14 feet long and weighs about 50,000 lbs. The properties of the light emitted, for example wavelength, is dependent on the period of the undulator. For the acetaldehyde experiments done at ALS the undulator was set to emit light between 8 eV to 16 eV for photoionization studies.

References for Chapter II

(1) Chen, P.; Chupka, W.A.; Berson, J.A. *J.Phys. Chem.* **1986**, *90*, 2319.

(2) Zhang, X.; Friderichsen, A.V.; Nandi, S.; Ellison, G.B.; David, D.E.; McKinnon, J.T.; Lindeman, T.G.; Dayton, D.C.; Nimlos, M.R. *Rev Sci. Instrum.* **2003**, *74*, 3077.

(3) Meyer, B. *Low Temperature Spectroscopy*; Elsevier: New York **1971**.

(4) Norrish, R.G.W.; Porter, G. *Nature* **1949**, *164*, 658.

(5) Daily, J.W.; Guan, Q.; Vasiliou, A.K.; Nimlos, M.R.; Ellison, G.B. *Int. J. Chem. Kin.* (to be submitted)

(6) Miller, D.R. *In Atomic and Molecular Beam Methods*, edited by Scoles, G.; Oxford University Press, New York, **1988**, Vol. 1.

(7) Shapiro, A. *The Dynamics and Thermodynamics of Compressible Fluid Flow*, The Ronald Press CO., **1953**, Vol 1.

(8) Anderson, J. *AIAA Journal* **1972,** *10,* 112.

(9) Bier, K.; Schmidt, B.; *Z. Angew* **1961**, *13*, 493

(10) *Instruction Manual AREF Time of Flight Power Supply from Jordon TOF products, Inc*.; Grass Valley,

(11) Guilhaus, M. *J. Mass Spectrom*. **1995,** *30*, 1519.

(12) Evan, U.; Dick. D. *Rev. Sci. Instrum.* **2000**, 71, 4415.

(13) Whittle, E.; Dows, D.A.; Pimentel, G.C.; *J. Chem. Phys*. **1954**, *22*, 1943

(14) Nandi, S.; *PhD. Thesis*, University of Colorado, **2001**

(15) Smith, M.H.; Rinsland, C.P.; Fridovich, B.; Rao, K.N. Intensities and Collision Broadening Parameters from Infrared Spectra. In Molecular Spectroscopy: A Modern Research; Academic Press, **1985**, Vol III

106 (16) Nandi, S.; Blanksby, S.J.; Zhang, X.; Nimlos, M.R.; Dayton, D.C.; Ellison, G.B. *J. Phys. Chem. A*. **2002**, , 7547.

(17) Jachnowitz, E.B.; *PhD Thesis*, University of Colorado, **2004.**

(18) Maccarone, A.T.; *PhD Thesis*, University of Colorado, **2007**

(19) http://www-als.lbl.gov/

(20) http://www.chemicaldynamics.lbl.gov/btw.html

Chapter III

Furan

3.1 Introduction

Furanyl compounds are important intermediates in the thermochemical decomposition of biomass. For instance, furan, **1**, furfural, **2** and 5-hydroxymethylfurfural, **3,** have been detected during the pyrolysis of plant material[1-4] (Figure 3.1). These species are largely thought to evolve from the thermal decomposition of the polysaccharides that are the principal components of plant cell walls. Separate pyrolysis experiments with these polysaccharides[5-7], cellulose and hemicellulose, appear to bear this out. The structures of glucose, **4**, and xylose, **5**, are also shown.

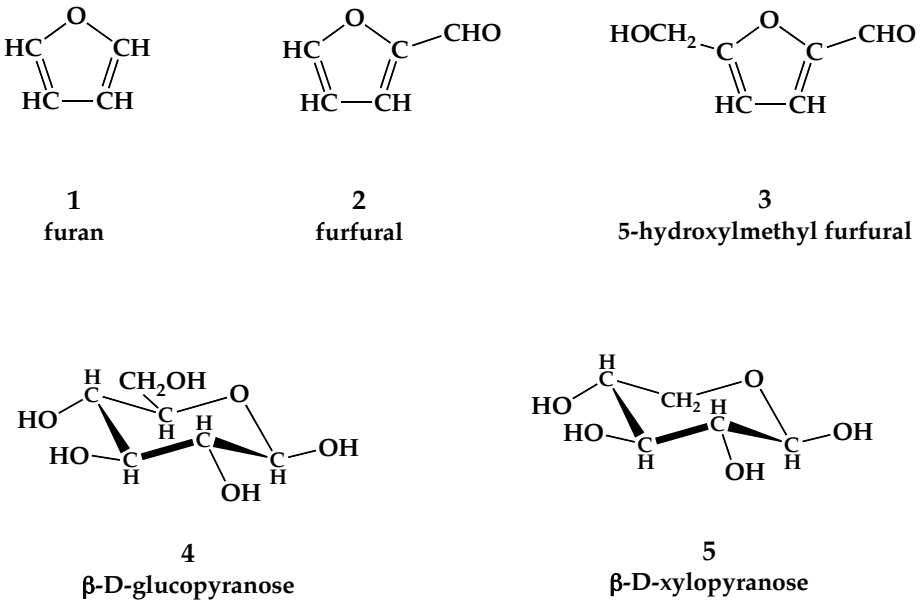

Figure 3.1 The structures of several biomass monomers.

Although these molecules have been measured during biomass pyrolysis, which is typically conducted at 700 — 900 K, their contribution to high temperature conversion processes is not clear. Consider biomass gasification, which can be followed by catalytic synthesis to produce a variety of transportation fuels. During gasification for fuel synthesis, the biomass is typically heated to between 1000 K and 1250 K, using H_2O (steam) as a carrier gas.[8]

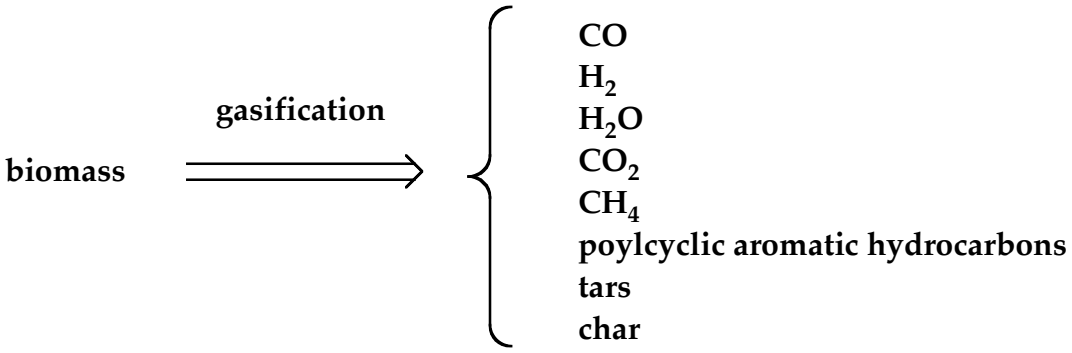

(3.1)

Clean syngas [CO and H_2] is the desired product from this process, though in reality CO_2, CH_4, polycyclic aromatic hydrocarbons (PAH), tars and char are also produced (3.1). As an example of fuel synthesis, the CO and H_2 can be catalytically combined to produce ethanol, as depicted in (3.2).

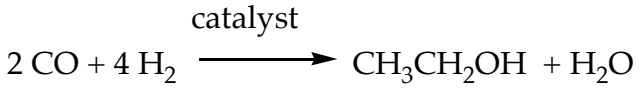

(3.2)

This approach for renewable fuel synthesis is nearly economically competitive for a variety of fuel feedstocks.[8]

In order to minimize tar formation during biomass gasification, a better understanding of formation reaction mechanisms is needed. Specifically, it is desirable to understand the mechanism for the formation of PAHs. Since the polysaccharides comprise up to 70% of plant cell walls, it is necessary to understand how their decomposition leads to the formation of PAHs.

It is likely that furans play an important role in PAH formation from sugars since these aromatic species appear to result from dehydration reactions of carbohydrates. Experimental measurements (*vide infra*) of the thermal decomposition of furan show that small hydrocarbon molecules,[9-14] such as acetylene, ketene and propyne are formed. In addition, some shock tube studies show that benzene can be produced.[14] This earlier work on the thermal decomposition of furan used techniques that were not effective for detecting radicals, which will likely play an important role in the formation of aromatic compounds.

We surmise that there is a link between carbohydrates and the formation of aromatic hydrocarbons. When heated: 1) carbohydrates dehydrate to a mixture of furanyl compounds, 2) furanyl species further decompose into smaller molecular fragments, which 3) ultimately recombine in less than 1 msec to form aromatic molecules. In this paper the connection between the simplest furanyl species, furan (**1** in Fig. 3.1) and aromatic compounds will be investigated. Results will be presented for pyrolysis of furan, **1**, in a heated, microtubular reactor:[18] C_4H_4O (furan) + $\Delta \rightarrow$ products. The resulting products are measured using vacuum-ultraviolet photoionization mass spectrometry (PIMS) and matrix isolation infrared spectroscopy (IR). The combination of these approaches has been successfully used in the past[16,19-21] to detect radicals and measure their infrared spectra. In this paper it will be shown that, along with the closed shell molecules measured earlier, furan decomposes to produce propargyl (CH_2CCH) radicals. We

have also observed the formation of benzene and other aromatic species from the thermal cracking products of furan.

3.2 Experimental Methods

The high temperature microtubular flow reactor described in chapter 2 section 2.2[18] (Figures 3.2 and 3.3) was used to decompose the simple biomass molecule furan (**1** in Figure 3.1). Thermal cracking products are produced by pulsing C_4H_4O (furan) seeded in an inert gas (roughly 1 – 2 atm) through a resistively heated silicon carbide tube at high temperature (up to 1700 K) into a vacuum chamber (about 10^{-5} Torr). The valve fires at a nominal rate of 10–50 Hz and is open for roughly 250 μsec. The gas is injected into the tube through a small orifice where the flow is choked, controlling the mass flow rate. The residence time in the heated section of the tube is roughly 65 μsec, which combined with low sample density, avoids radical-radical reactions following thermal decomposition. The tube flow chokes at the exit and expands supersonically in an under expanded jet to a vacuum at 10^{-5} Torr. This free jet expansion rapidly cools the radicals down to about 40 K (rotationally)[22] within approximately a tube diameter and eliminates any further reactions. Two independent spectroscopic techniques were used to monitor the output of the hyperthermal nozzle. The nozzle in Figure 3.2 uses a fixed-frequency (λ_0 = 118.2 nm) photoionization mass spectrometer to detect the species emerging from the reactor. Figure 3.3 shows the high temperature nozzle configured in a different way in which the beam impinges onto a 20 K CsI window forming a matrix for IR detection. The combination of high nozzle wall temperature (up to 1700 K) and short residence time allows for a high yield of radicals (approximately 10^{13} radicals $pulse^{-1}$).

The photoionization TOF mass spectrometer that was used in these experiments was previously described in chapter II section 2.3 and only a brief description is provided here.[13] The output reactor is pulsed into a vacuum chamber (10^{-5} Torr) and then directed through a skimmer (3 mm ID) into an ionization vacuum chamber (10^{-7} Torr), where radicals are ionized using vacuum ultraviolet photons (118.2 nm or 10.487 eV with 0.5 μJ/pulse at 10-30 Hz). The mass spectra are collected using a reflectron TOF mass spectrometer (Jordan). The positive ions are detected by a channeltron and the spectra are collected with a digital oscilloscope (Tektronix 500 MHz) interfaced to a computer. Typically, averaging of 100 to 1000 pulses is needed to obtain mass spectra with reasonable signal-to-noise and since the laser is pulsed at 10 Hz, scans are collected in 1-2 minutes. As a result, mass spectra at several temperatures can be obtained in 20 to 30 minutes. These experiments are much faster than the matrix isolation experiments, which require about 4 to 6 hours for an experiment at a single temperature.

The photoionization mass spectrometer was calibrated prior to all experiments discussed in this work. Using NO or $CH_3CH{=}CH_2$, or $C_6H_5CH_3$ as calibrants with well-characterized cracking patterns, the flight times ranging from 10 to 100 μs were used to construct a calibration curve. The calibration process is repeated during and at the end of each experiment to assure that significant drift did not occur in the TOF electronics or PIMS instrument. All peaks in the resulting mass spectra are accurate to within ± 0.2 amu.

In Figure 3.3 the microtubular reactor was mounted to the vacuum shroud of an APD two stage closed-cycle helium cryostat, approximately 2.5 cm away from the cryogenic CsI window (Chapter II section 2.4). Gas mixtures were created by seeding a precursor in argon. The precursor vapor was collected by de-gassing the precursor liquid at room temperature. The hyperthermal nozzle was operated with approximately a 1.3 ms pulse width and a stagnation

pressure of 1.2 atm, with a 1.2 L stagnation reservoir. The pressure drop in the stagnation reservoir was measured using a capacitance manometer to determine the gas throughput. Radicals were deposited on a CsI salt window cryogenically cooled to 20 K. The infrared spectrum of the sample was measured using a Nicolet Magna 550 Fourier transform infrared spectrometer with a mercury/cadmium/telluride (MCT-A or B) detector. The APD cryostat is equipped with a pair of CsI side windows through which the IR beam from the instrument passes.

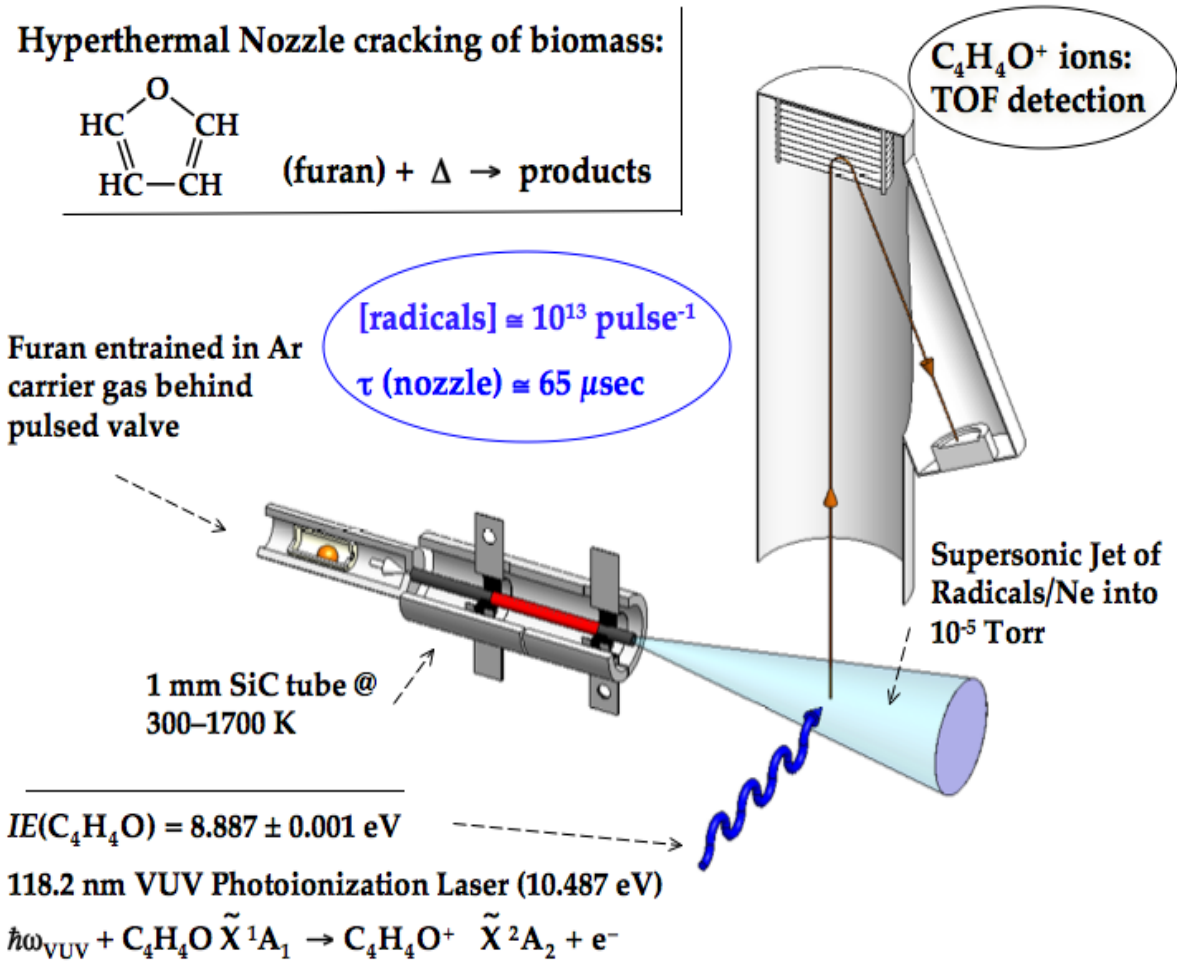

Figure 3.2 Schematic view of the reactor for thermal cracking of biomass samples with PIMS detection.

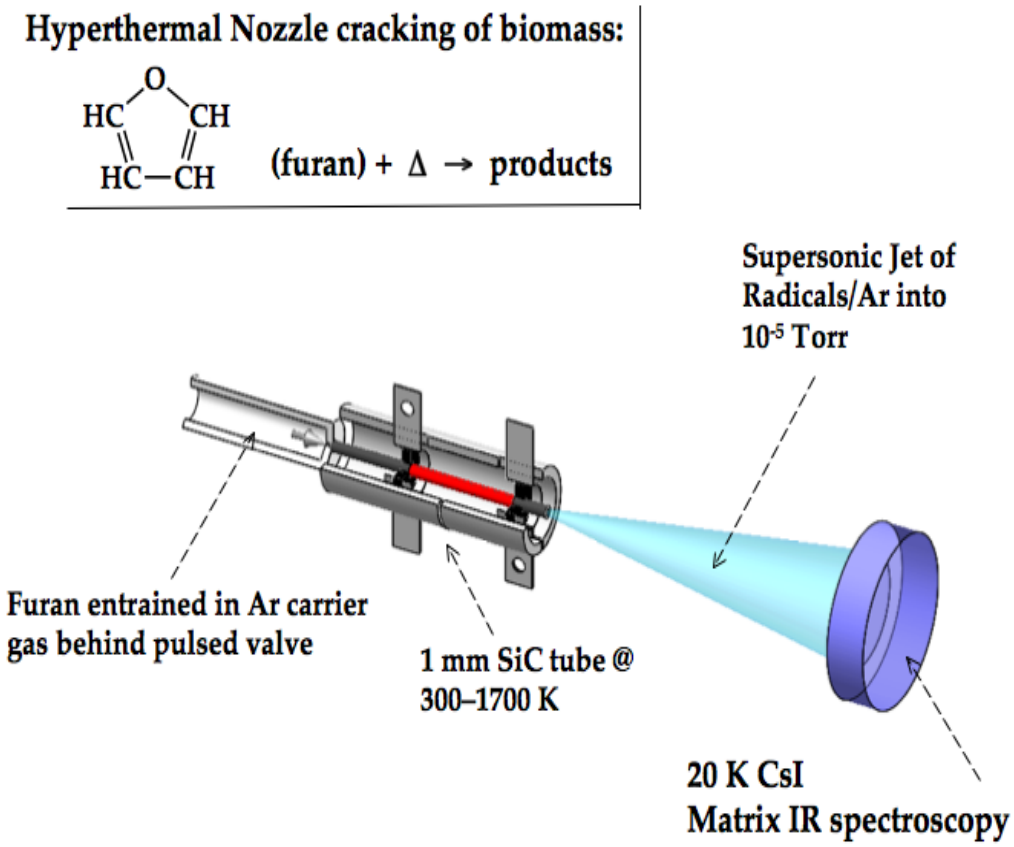

Figure 3.3 Schematic view of the reactor for thermal cracking of biomass samples with IR detection.

3.3 Results: Thermal Decomposition of Furan

The high temperature, microtubular reactor is an appealing device to study the thermal decomposition of isolated biomass targets in rare gases. Because the nominal residence time of the entrained furan in the hot nozzle is roughly 65 μsec, we are able to monitor the early fragmentation products. The hot nozzle in Figures 3.3 and 3.4 with PIMS and matrix IR detection permits us to examine the early thermal cracking products.

The thermal decomposition of furan has been studied in flow tubes[9,13], shock tubes,[11,12,14] and by IR homogeneous pyrolysis.[10] A summary of these results is collected in Table 3.1 These studies have been conducted over a wide range of pressures (1 mTorr — 20 atm) and temperatures (500 K — 3000 K) and it is commonly agreed that there are two major decomposition channels.

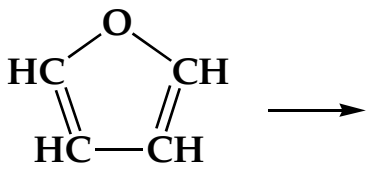

a) $CO + CH_3C{\equiv}CH$

b) $CH_2{=}C{=}O + HC{\equiv}CH$

(3.3)

The thermochemistry of these two pathways is well known.[24,25]

$\Delta_{rxn}H_{298}(C_4H_4O, \text{furan} \rightarrow CO + CH_3C{\equiv}CH) = 26.1 \pm 0.3 \text{ kcal mol}^{-1}$ **(3.4a)**

$\Delta_{rxn}H_{298}(C_4H_4O, \text{furan} \rightarrow CH_2{=}C{=}O + HC{\equiv}CH) = 51.3 \pm 0.5 \text{ kcal mol}^{-1}$ **(3.4b)**

Table 3.1
Previous Measurements of the thermal decomposition of furan.

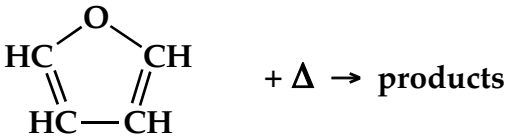

Apparatus	Conditions	Notes
Very Low Pressure Pyrolysis (VLPP)[9]	1050—1270 K @ 1mTorr EI mass spectrometry	$CO + C_3H_4$
Shock Tube[14]	1050—1460 K GC/FID	major channels: $CH_2{=}C{=}CH_2$, C_4H_6, C_2H_4, CH_4, C_4H_4, C_4H_2,
Flow tube[13]	960—1085 K @ 1 Torr	$CO + C_3H_4$
Shock Tube[12]	1100—1700 K@ 20 atm UV, FTIR	$CO + C_3H_4$, $HCCH + CH_2CO$
Shock Tube[11]	500—3000K @ 600 Torr laser-schlieren densitometry TOF-MS	major channels: $HCCH + CH_2CO$ $C_3H_4 + CO$ Below 1700 K: $C_3H_4 + CO$ dominates
IR homogeneous pyrolysis[10]	GC-MS/FID, FTIR, EPR CO_2 10.6 μm irradiation of 7 Torr SF_6 followed by heating *via* rapid inter- and intramolecular relaxation. Hot SF_6 heats furan.	major channels: $HCCH+CH_2CO$ $C_3H_4 + CO$

In Figure 3.4 are shown the PIMS spectra of the decomposition products of furan in a high temperature, supersonic nozzle. At lower nozzle temperatures we observe decomposition products that are consistent with the shock tube temperatures reported by Fulle *et al.*[11] (900 K – 1500 K) and others in Table 3.1. The bottom trace in Figure 3.4 is the mass spectrum that results when furan (1 Torr C_4H_4O entrained in 2 atm He) transits the nozzle at room temperature (300 K). Photoionization with 118.2 nm VUV light produces the parent ion, m/z 68 $C_4H_4O^+$, and its isotope peak, m/z 69. The (69/68) isotope ratio is measured to be 5%. The *IE*(furan) was measured[26] to be 8.887 ± 0.001 eV; even though C_4H_4O is ionized by 10.487 eV photons, no fragmentation of the parent ion $C_4H_4O^+$ is observed. When the wall temperature of the SiC nozzle is raised to 1500 ± 100 K, product ions at m/z 40 and 42 are observed which arise from ionization[27-29] of C_3H_4 and CH_2CO. Increasing the wall temperature to 1650 ± 100 K leads to an increase in the $C_3H_4^+$ and CH_2CO^+ signals and new features at m/z 39 and m/z 41 are detected. The band at m/z 41 is consistent with the ketene isotope peak. The (41/40) isotope ratio is calculated to be 3% for $C_3H_4^+$. We believe that the signal at m/z 39 is CH_2CCH^+ and it is a diagnostic for the presence of the propargyl radical. The *IE*(CH_2CCH) has been measured by fixed frequency photoelectron spectroscopy and by ZEKE spectroscopy[30] to be 69953 ± 10 cm^{-1} (8.674 ± 0.001 eV). [Because the *IE*(HCC) = 11.645 ± 0.0014 eV,[31] it is unlikely that the VUV laser could ionize the CH_3CC radical.] As with the case of furan, photoionization of CH_2CCH by 118.2 nm photons does not induce fragmentation (even though the VUV laser is 1.8 eV above the threshold to ionize propargyl radical). Notice that some of the thermal cracking products of furan cannot be photoionized by the 10.487 eV VUV laser in Figure 3.4: H atom *IE*(H) = 13.5984 ± 0.0001 eV, acetylene[31] *IE*(HC≡CH) = 11.4006 ± 0.0006 eV, and carbon monoxide[32] *IE*(CO) = 14.0141 ± 0.0003 eV.

Figure 3.5 shows the PIMS spectra for appearance of decomposition products from furan as the temperature of the nozzle is increased. At wall temperature of 1350 ± 100 K features for both $C_3H_4^+$ m/z 40 and CH_2CO^+ m/z 42 appear. At 1500 ± 100 K, faint signals for m/z 39 and m/z 41 are observed. The m/z 41 feature is 5% as intense as the $C_3H_4^+$ m/z 40 signal and is likely the isotope peak. As the wall temperature of the nozzle is steadily increased to 1650 ± 100 K, the m/z 39 peak (propargyl radical) steadily grows.

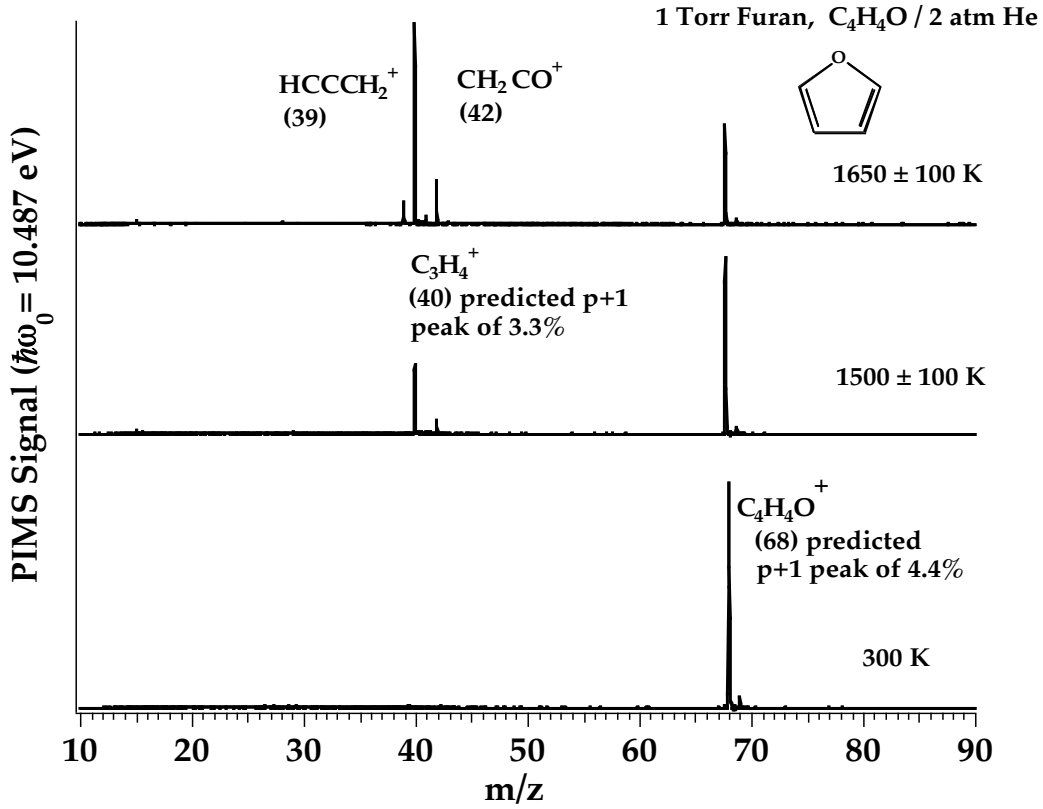

Figure 3.4 PIMS spectra of the decomposition products of furan in a high temperature, supersonic nozzle. The bottom trace is the mass spectrum that results when furan (1 Torr C_4H_4O entrained in 2 atm He) transits the nozzle at room temperature (300 K).

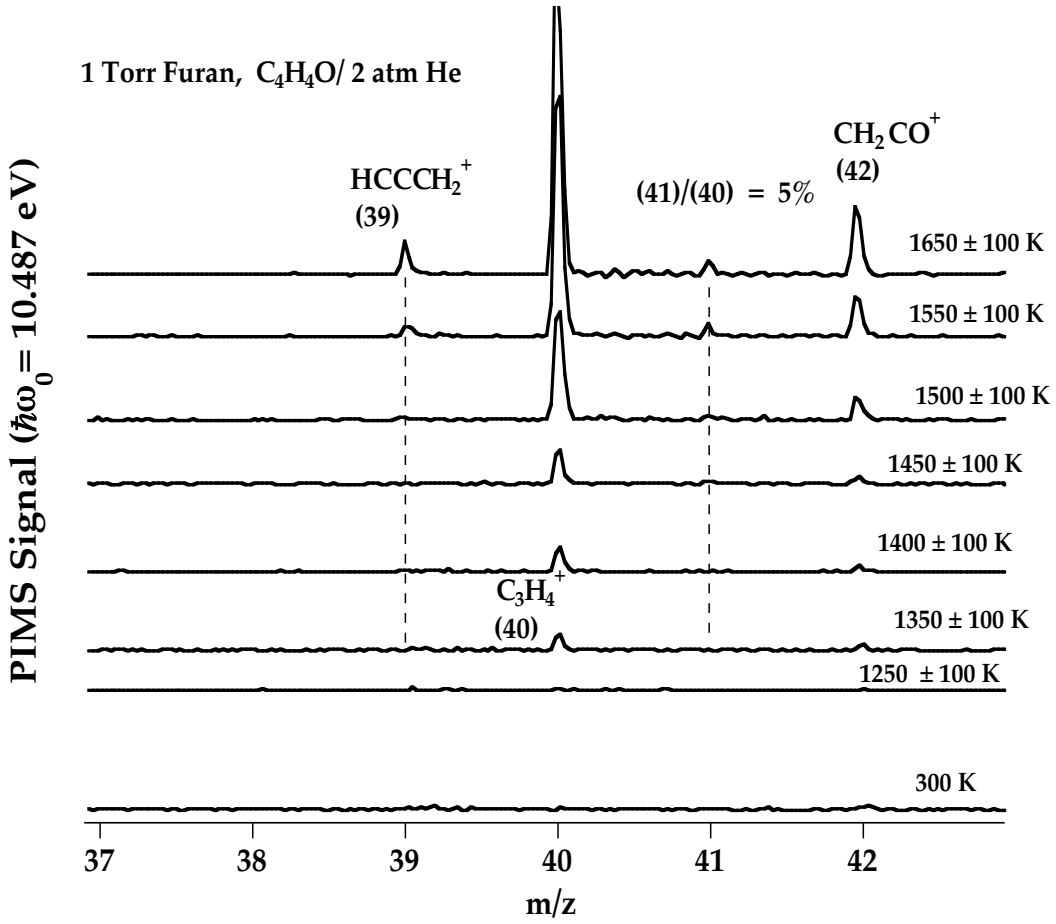

Figure 3.5 PIMS spectra for appearance of decomposition products as the wall temperature of the reactor is increased.

If the concentration of furan is raised (10 Torr C_4H_4O entrained in 2 atm He) bimolecular reactions are observed; see Figure 3.6. In addition to the parent $C_4H_4O^+$ feature at m/z 68, all of the peaks present in Figures 3.4 and 3.5 are present (39, 40, 41, and 42). New features at m/z 78 ($C_6H_6^+$), m/z 94 ($C_6H_5OH^+$) and m/z 104 ($C_6H_5CH{=}CH_2^+$) are now present.[33-35] The spectra in Figure 3.6 were produced by a contaminated nozzle (see background signals around m/z 39-43 in the 300 K trace). But it is clear that the features at m/z 78, 94, and 104 are growing in as the nozzle is heated. These species [probably benzene (78), phenol (94), and styrene (104)] certainly arise from bimolecular reactions among decomposition products of furan.

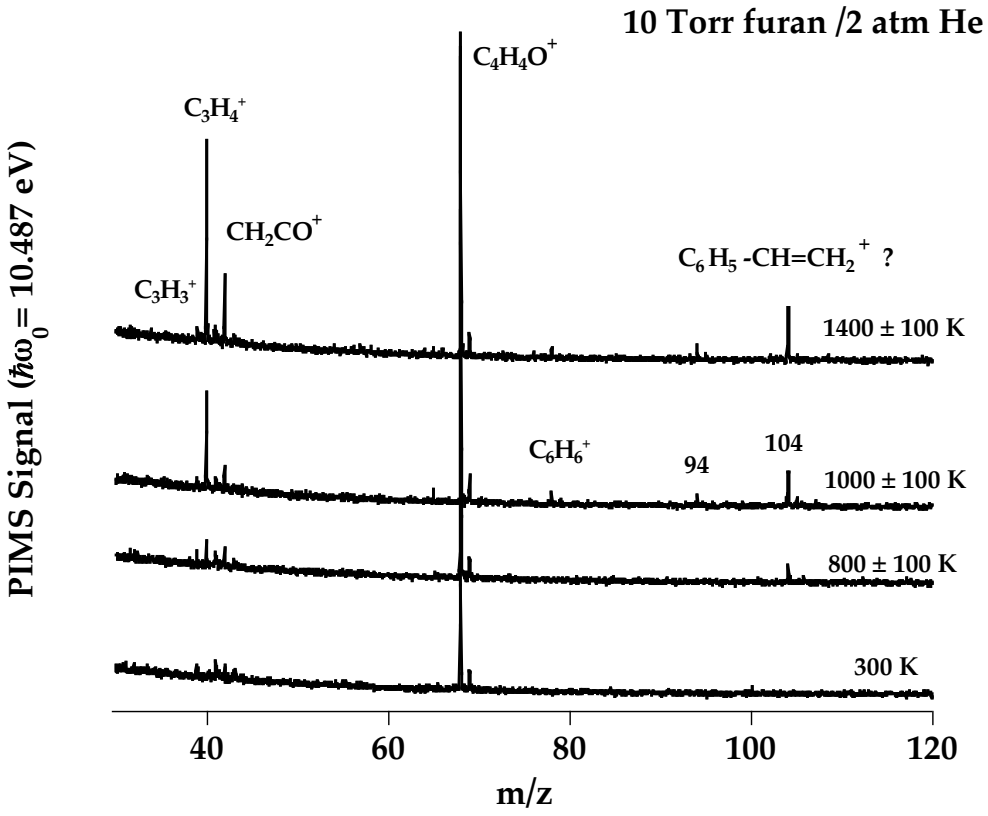

Figure 3.6 PIMS spectra of the decomposition products of higher concentrations of furan (10 Torr C_4H_4O entrained in 2 atm He) in a high temperature, reactor.

The PIMS spectra in Figures 3.4 - 3.6 are very informative but they only identify molecular products by m/z, the mass-to-charge ratio. Isomers are always a problem and some important molecules (CO and HCCH) cannot be detected by the 118.2 nm VUV laser. In Figure 3.7 are shown the infrared spectra of the decomposition products of furan at 1500 ± 100 K. This scan reveals CH peaks for CH_3CCH, HCCH, furan (C_4H_4O), and CH_2=C=O. The presence of the propargyl radical is revealed by the intense $\nu_1(CH_2CC\text{-}H)$ stretch[16] at 3309 cm^{-1}.

In Figure 3.8 is the infrared spectrum of the decomposition products of furan at 1500 ± 100 K in the mid-IR region. Carbon monoxide (both isotopomers ^{12}CO and ^{13}CO) and CH_2=C=O are clearly present.(See Appendix A for details on ketene synthesis). Figure 3.9 is the infrared spectrum of the decomposition products of furan at 1500 ± 100 K over the finger-print region. Distinctive bands of CH_2=C=O and HC≡CH can be identified as decomposition products.

One of the shock tube studies[14] reports CH_2=C=CH_2 as a cracking product of furan. It is possible that the PIMS signal at m/z 40 could be evidence of allene rather than CH_3CCH. The IR spectrum of allene is well known but the IR spectra in Figures 3.7 - 3.9 show no bands of CH_2=C=CH_2. Both the PIMS traces and IR spectra provide convincing evidence of both CH_3CCH (propyne) and CH_2CCH (propargyl radical). One might suspect that propyne is thermally cracking at higher temperatures to produce propargyl: $CH_3CCH + \Delta \rightarrow CH_2CCH + H$. The bond energies of methylacetylene have been measured[36] and DH_{298}(H-CH_2CCH) is known to be 90 kcal mol^{-1}. Consequently it is very unlikely that the hyperthermal nozzle could induce propyne to dissociate to CH_2CCH + H. The bottom trace in Figure 3.10 compares the matrix IR spectrum of CH_3C≡CH heated to 1500 K with a sample of methylacetylene that was deposited at room temperature. The spectra are identical. The strong C-H stretching mode for CH_3CCH is

identified at 3322.8 cm^{-1}. The insert at the top of the spectrum is an expanded scan of the region about $\nu_1(CH_3CC\text{-}H)$. There is no detectable signal for the intense $\nu_1(CH_2CC\text{-}H)$ stretch[16] of propargyl radical at 3309 cm^{-1}. A similar attempt to observe thermal cracking at 1500 ± 100 K of d_3-methylacetylene, $CD_3CCH + D \rightarrow CD_2CCH + D$, with the PIMS in Figure 3.2 also failed. When d_3-metylacetylene is passed through the nozzle at 300 K or 1500 K, the PIMS only detects the parent species, $(CD_3CCH)^+$ m/z 43, and no signals from d_2-propargyl, $(CD_2CCH)^+$ m/z 41, are observed.

To further confirm that propargyl radical is a direct product of furan decomposition, a 1:1 mixture of CD_3CCH and C_4H_4O was passed through the SiC nozzle at temperatures of 300, 1300 ± 100, and 1600 ± 100 K. The resulting PIMS spectra are shown in Figure 3.11; intense features at m/z 43 $(CD_3CCH)^+$ and m/z 68 $(C_4H_4O)^+$ are evident at room temperature. One expects the isotope for CD_3CCH and furan to be 3.2% and 4.4%. The measured ratios are (44/43) = 3% and (69/68) = 5%.

As the nozzle temperature is raised to 1300 K, fragmentation of the CD_3CCH/furan mixture commences. At 1600 ± 100 K, the inset shows that new bands at m/z 39 $(CH_2CCH)^+$, 40 $(CH_3CCH)^+$, 41, and 42 $(CH_2{=}C{=}O)^+$ are observed. The feature at m/z 41 could be CD_2CCH^+ or the isotope peak related to the CH_3CCH cracking product of furan. The (41/40) ratio in the 1600K scan in Figure 3.11 is measured to be 4%. The CH_3CCH (41/40) isotope ratio is expected to be 3.2%. We conclude that the peak at m/z 41 is the isotope peak belonging to CH_3CCH, which results from cracking of furan.

The IR spectra in Figure 3.10 and the PIMS spectra of Figure 3.11 are consistent. Heating $CH_3C{\equiv}CH$ to 1500 K does not produce the propargyl radical, CH_2CCH. Consequently CH_2CCH, m/z 39, in Figure 3.4 is a direct decomposition product of furan itself.

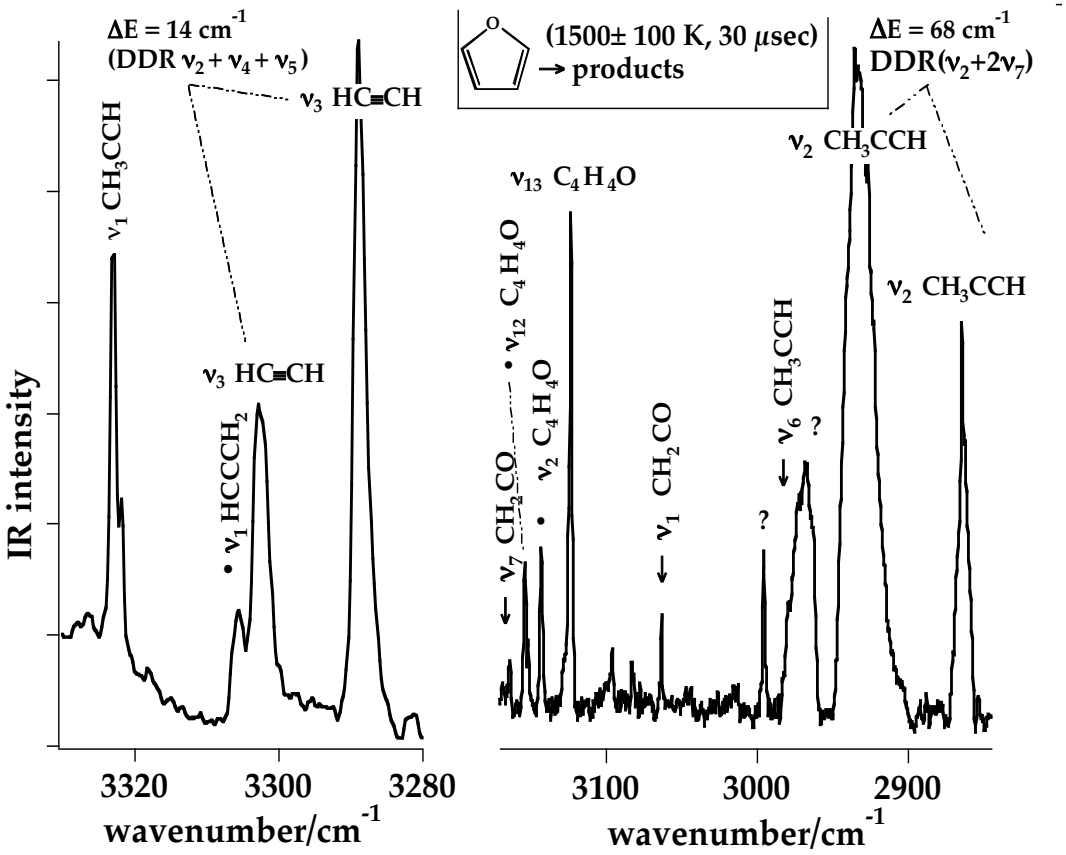

Figure 3.7 Infrared spectrum of the decomposition products of furan at 1500 ± 100 K. The presence of the propargyl radical is revealed by the intense $\nu_1(CH_2CC\text{-}H)$ stretch[16] at 3309 cm^{-1}.

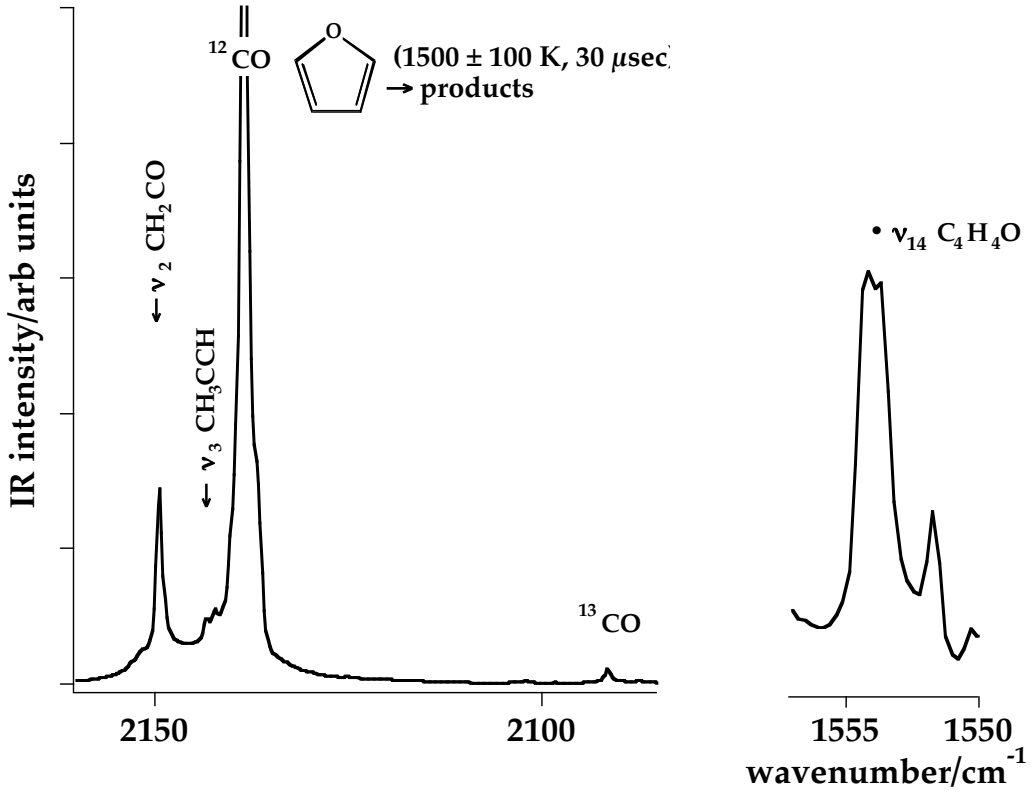

Figure 3.8 Infrared spectrum of the decomposition products of furan at 1500 ± 100 K. Both ketene and carbon monoxide (^{12}CO and ^{13}CO) are clearly present.

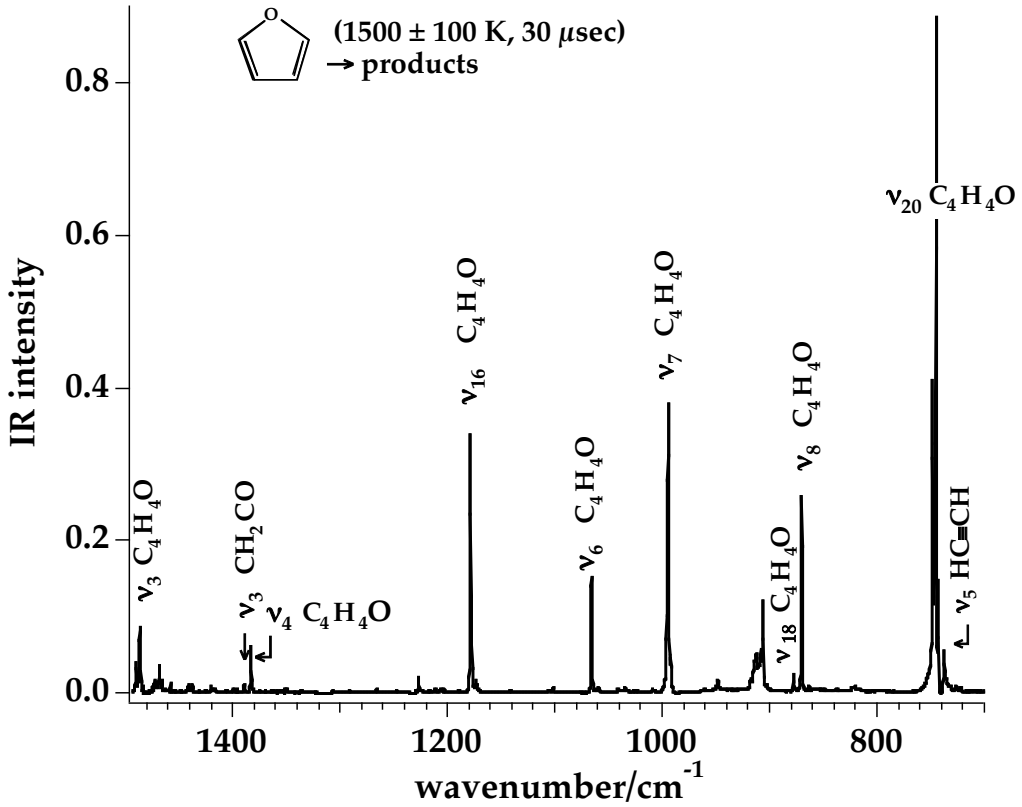

Figure 3.9 Infrared spectrum of the decomposition products of furan at 1500 ± 100 K. Distinctive bands of CH_2=C=O and HC≡CH can be identified.

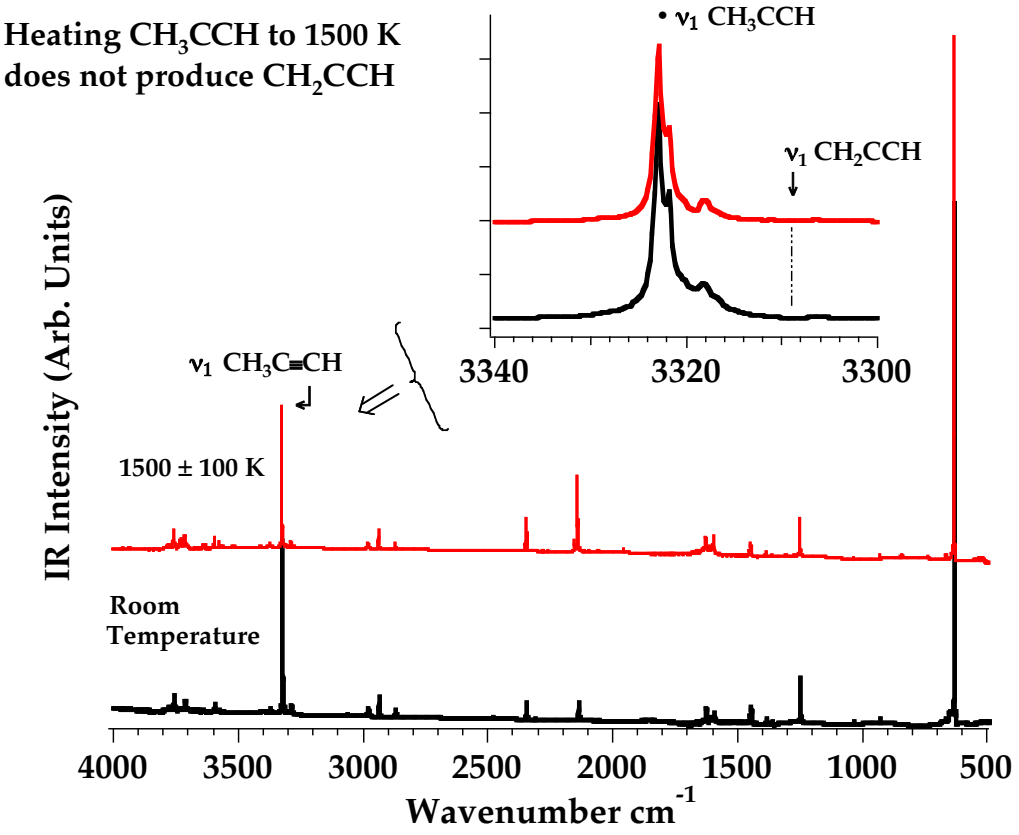

Figure 3.10 The bottom trace in this figure compares the matrix IR spectrum of $CH_3C \equiv CH$ heated to 1500 K with a sample of methylacetylene that was deposited at room temperature. The spectra appear identical.

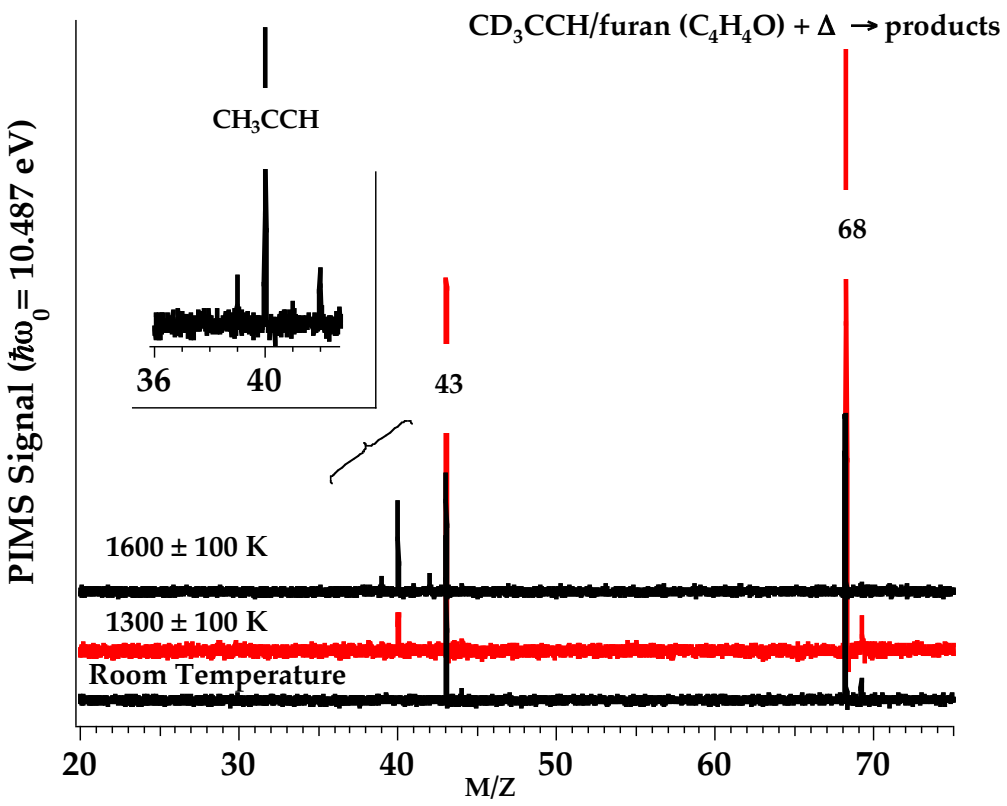

Figure 3.11 PIMS spectra of a 1:1 mixture of CD_3CCH and C_4H_4O passed through the SiC tube at temperatures of 300, 1300 ± 100, and 1600 ± 100 K.

3.4 Discussion and Conclusions

These experiments have enabled us to identify the initial thermal cracking products of furan. Using a high-temperature nozzle as a tubular reactor, we have demonstrated that furan thermally cracks to produce (CO + CH_3CCH) and (HCCH + CH_2CO). When the wall temperature reaches 1350 ± 100 K, all of these species are detected by both the PIMS and IR spectrometers of Figures 3.2 and 3.3. At a higher temperature of 1550 ± 100 K, furan (C_4H_4O) begins to produce the propargyl radical (CH_2CCH) as well. Because the residence time of the furan in the tubular reactor is roughly 65 μsec, we believe that (CO + CH_3CCH), (HCCH + CH_2CO), and the CH_2CCH radical are the primary products from cracking of C_4H_4O. Increasing the backing pressure of the carrier gas by an order of magnitude leads to the formation of aromatic hydrocarbons such as benzene and styrene (Figure 3.6). It is well established[37-47] that propargyl radicals dimerize to produce C_6H_6. In an earlier study with this apparatus,[16] CH_2CCH radicals were observed to form C_6H_6; both PIMS and IR spectroscopy were used to confirm that C_6H_6 was benzene.

The unimolecular dissociation pathways of furan have been studied by *ab initio* electronic structure methods. Figure 3.12 is a composite summary of the potential energy surface for the decomposition of furan at 0 K. This figure is adapted from Sendt *et al.*[48] and results from G2(MP2) calculations. The energies for C-H rupture (shown in blue) or C-C cleavage (shown in red) are predicted to be 122 and 89 kcal mol^{-1}. Both C-H bond energies to produce the α-C_4H_3O and β-C_4H_3O furyl radicals (of $^2A'$ symmetry) are much larger than C-H bond energy of benzene itself.[49] Consequently it is predicted that all of the fragmentation processes of furan ensue following rearrangement to either the α-carbene (which directly fragments to HCCH +

CH_2=C=O) or the β-carbene. The β-carbene isomerizes to buta-2,3-dienal, CH_2=C=CH-CHO, which decomposes to CO + CH_3CCH.

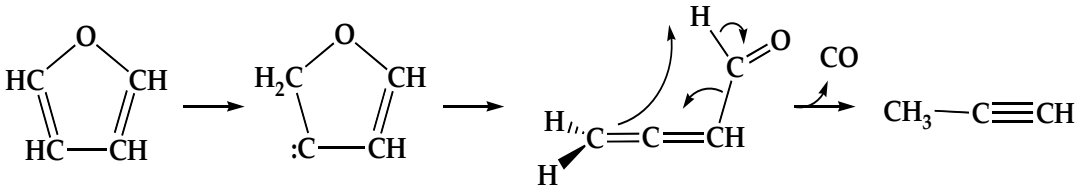

(3.5)

The propargyl radical (CH_2CCH, $\tilde{X}\ ^2B_1$) could result from the intermediate aldehyde in (3.5). It is predicted[48] that the C-C bond energy of buta-2,3-dienal is about 3 eV, DH_{298}(CH_2=C=CH-CHO → CH_2CCH + CHO) = 74 kcal mol^{-1}. Following the 65 μsec thermal cracking of furan in the tubular reactors we observe all but one of the direct products predicted[48] by the G2(MP2) calculations: HCCH, CH_2CO, CH_3CCH, CO, CH_2CCH and HCO. With the exception of the formyl radical, all other species have been identified by mass spectrometry and infrared spectroscopy. One would not expect[24] the formyl radical to survive for very long in the hot tubular reactor. The DH_{298}(H-CO) is only 15.6 ± 0.1 kcal mol^{-1}so HCO is easily dissociated. Consequently it is expected that the following reactions occur: CH_2=C=CH-CHO → $CH_3C{\equiv}CH$ + CO + H.

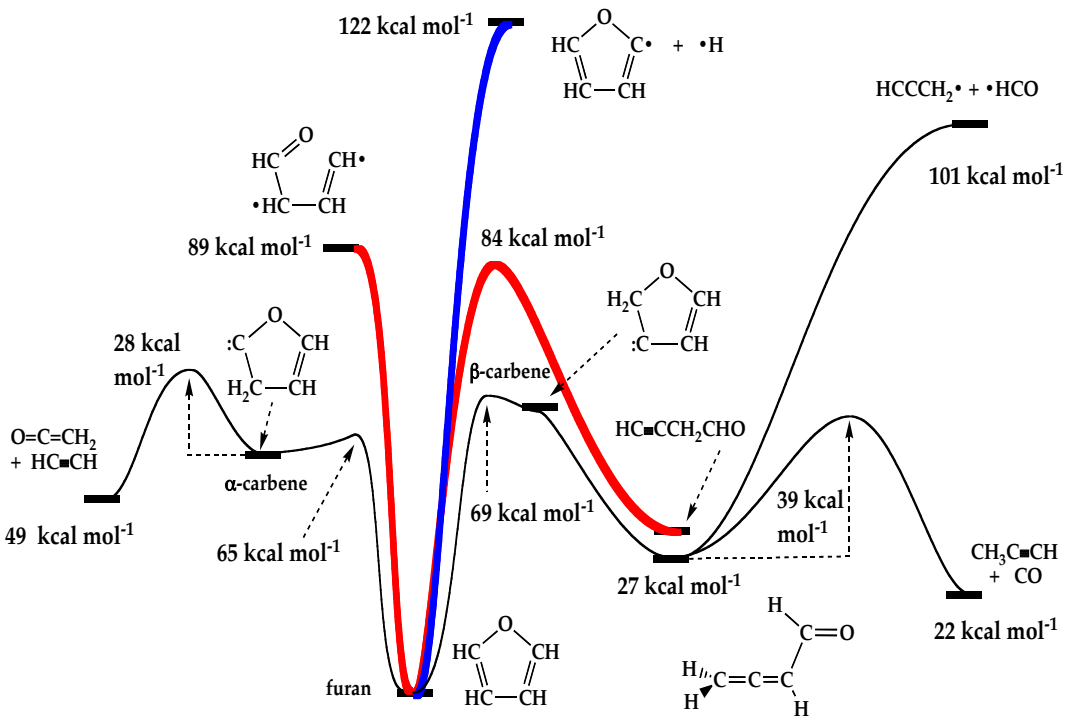

G2(MP2) Energetics at 0 K adapted from calculations of Sendt *et al.*, *J. Phys. Chem. A*, 104, 1861 (2000)

Figure 3.12 Potential energy surface for the decomposition of furan at 0 K. These are G2(MP2) calculations and this figure is adapted from Sendt *et al.*[48]

Our experimental results demonstrate that the first thermal dissociation products of furan (**1** in Figure 3.1) are (CO + CH_3CCH) and (HCCH + CH_2=C=O). At higher temperatures, furan also cracks to generate the propargyl radical. At low pressures in the tubular reactor, these molecules are all prompt products from furan and are formed in less than 100 μsec. At higher pressures in the tubular reactor, radicals such as CH_2CCH react further to produce complex aromatic gasification products such as C_6H_6 (benzene) and $C_6H_5CH=CH_2$ (styrene).

References for Chapter III

(1) Beaumont, O. *Wood and Fiber Science* **1985**, *17*, 228.

(2) Piskorz, J.; Radlein, D.; Scott, D. S. *J. Anal. Appl. Pyrolysis* **1986**, *9*, 121.

(3) Evans, R. J.; Milne, T. A. *Energy & Fuels* **1987**, *1*, 123.

(4) Evans, R. J.; Milne, T. A. *Energy & Fuels* **1987**, *1*, 311.

(5) Shafizadeh, F.; Lai, Y. Z. *J. Org. Chem.* **1972**, *37*, 278.

(6) Shafizadeh, F.; McGinnis, G. D.; Philpot, C. W. *Carbohydr. Res.* **1972**, *25*, 23.

(7) Shafizadeh, F.; Lai, Y. Z.; McIntyre, C. R. *J. Appl. Polymer Sci.* **1978**, *22*, 1183.

(8) Phillips, S. D. *Ind. Eng. Chem. Res.* **2007**, *46*, 8887.

(9) Grela, M. A.; Amorebieta, V. T.; Colussi, A. J. *J. Phys. Chem.* **1985**, *89*, 38.

(10) Hore, N. R.; Russell, D. K. *New J. Chem.* **2004**, *28*, 606.

(11) Fulle, D.; Dib, A.; Kiefer, J. H.; Zhang, Q.; Yao, J.; Kern, R. D. *J. Phys. Chem. A* **1998**, *102*, 7480.

(12) Organ, P. P.; Mackie, J. C. *J. Chem. Soc. - Faraday Trans.* **1991**, *87*, 815.

(13) Bruinsma, O. S. L.; Tromp, P. J. J.; Nolting, H.; Moulijn, J. A. *Fuel* **1988**, *67*, 334.

(14) Lifshitz, A.; Bidani, M.; Bidani, S. *J. Phys. Chem.* **1986**, *90*, 5373.

(15) Friderichsen, A. V.; Shin, E. J.; Evans, R. J.; Nimlos, M. R.; Dayton, D. C.; Ellison, G. B. *Fuel* **2001**, *80*, 1747.

(16) Jochnowitz, E. B.; Zhang, X.; Nimlos, M. R.; Varner, M. E.; Stanton, J. F.; Ellison, G. B. *J. Phys. Chem. A* **2004**, *109*, 3812.

(17) Rohrs, H. W.; Wickham-Jones, C. T.; Berry, D.; Ellison, G. B.; Argrow, B. M. *Rev. Sci. Instrum.* **1995**, *66*, 2430.

(18) Zhang, X.; Friderichsen, A. V.; Nandi, S.; Ellison, G. B.; David, D. E.; McKinnon, J. T.; Lindeman, T. G.; Dayton, D. C.; Nimlos, M. R. *Rev. Sci. Inst.* **2003**, *74*, 3077.

(19) Friderichsen, A. V.; Radziszewski, J. G.; Nimlos, M. R.; Winter, P. R.; Dayton, D. C.; David, D. E.; Ellison, G. B. *J. Am. Chem. Soc.* **2001**, *123*, 1977.

(20) Nandi, S.; Arnold, P. A.; Carpenter, B. K.; Nimlos, M. R.; Dayton, D. C.; Ellison, G. B. *J. Phys. Chem. A* **2001**, *105*, 7514.

(21) Nandi, S.; Blanksby, S. J.; Zhang, X.; Nimlos, M. R.; Dayton, D. C.; Ellison, G. B. *J. Phys. Chem. A* **2002**, *106*, 7547.

(22) Chen, P.; Colson, S. D.; Chupka, W. A.; Berson, J. A. *J. Phys. Chem.* **1986**, *90*, 2319.

(23) Brown, A. L.; Dayton, D. C.; Nimlos, M. R.; Daily, J. W. *Energy & Fuels* **2001**, *15*, 1276.

(24) Blanksby, S. J.; Ellison, G. B. *Acct. Chem. Res.* **2003**, *36*, 255.

(25) Pedley, J. B.; Naylor, R. D.; Kirby, S. P. *Thermochemistry of Organic Compounds*, 2 ed.; Chapman and Hall: New York, 1986. The 298 K enthalpies of formation are: CO (-26.42 ± 0.04 kcal mol^{-1}), CH_3CCH (44.2 ± 0.2 kcal mol^{-1}), HCCH (54.3 ± 0.2 kcal mol^{-1}), and CH_2CO (-11.4 ± 0.4 kcal mol^{-1}).

(26) Herzberg, G. H. *Molecular Spectra and Molecular Structure: Electronic Spectra and Electronic Structure of Polyatomic Molecules*; D. Van Nostrand: Princeton, New Jersey, 1967; Vol. III.

(27) Baker, C.; Turner, D. W. *Proc. Roy. Soc. (London)* **1968**, *308*, 19. *IE*(CH_3CCH) = 10.37 ± 0.01 eV

(28) Hall, D.; Maier, J. P.; Rosmus, P. *Chem. Phys.* **1977**, *24*, 373.

(29) Niu, B. H.; Bai, Y.; Shirley, D. A. *J. Chem. Phys.* **1993**, *99*, 2520. *IE*(CH_2CO) = 9.6191 ± 0.0004 eV

(30) Gilbert, T.; Pfab, R.; Fischer, I.; Chen, P. *J. Chem. Phys.* **2000**, *112*, 2575.

(31) Lau, K. C.; Ng, C. Y. *Acct. Chem. Res.* **2006**, *39*, 823.

(32) Erman, P.; Karawajczyk, A.; Rachlewkallne, E.; Stromholm, C.; Larsson, J.; Persson, A.; Zerne, R. *Chem. Phys. Lett.* **1993**, *215*, 173.

(33) Chewter, L. A.; Sander, M.; Müller-Dethlefs, K.; Schlag, E. W. *J. Chem. Phys.* **1987**, *86*, 4737. $IE(C_6H_6) = 9.24372 \pm 0.00005$ eV

(34) Lipert, R. J.; Colson, S. D. *J. Phys. Chem.* **1990**, *94*, 2358. $IE(C_6H_5OH) = 8.508 \pm 0.001$ eV

(35) Dyke, J. M.; Ozeki, H.; Takahashi, M.; Cockett, M. C. R.; Kimura, K. *J. Chem. Phys.* **1992**, *97*, 8926. $IE(C_6H_5CH{=}CH_2) = 8.464 \pm 0.001$ eV

(36) Robinson, M. S.; Polak, M. L.; Bierbaum, V. M.; DePuy, C. H.; Lineberger, W. C. *J. Am. Chem. Soc.* **1995**, *117*, 6766. $DH_{298}(H\text{-}CH_2CCH) = 90 \pm 3$ kcal mol^{-1}; enthalpy of formation (298K) (CH_2CCH) = 82.5 ± 3.0 kcal mol^{-1}

(37) Alkemade, U.; Homann, K. H. *Zeitsch. Phys. Chem.* **1989**, *161*, 19.

(38) Morter, C. L.; Farhat, S. K.; Adamson, J. D.; Glass, G. P.; Curl, R. F. *J. Phys. Chem.* **1994**, *98*, 7029.

(39) Atkinson, D. B.; Hudgens, J. W. *J. Phys. Chem. A* **1999**, *103*, 4242.

(40) Fahr, A.; Nayak, A. *Int. J. Chem. Kinetics* **2000**, *32*, 118.

(41) Scherer, S.; Just, T.; Frank, P. *Proc. Comb. Inst.* **2000**, *28*, 1511.

(42) Miller, J. A.; Klippenstein, S. J. *J. Phys. Chem. A* **2001**, *105*, 7254.

(43) DeSain, J. D.; Taatjes, C. A. *J. Phys. Chem. A* **2003**, *107*, 4843.

(44) Miller, J. A.; Klippenstein, S. J. *J. Phys. Chem. A* **2003**, *107*, 7783.

(45) Shafir, E. V.; Slagle, I. R.; Knyazev, V. A. *J. Phys. Chem. A* **2003**, *107*, 8893.

(46) Tang, W. Y.; Tranter, R. S.; Brezinsky, K. *J. Phys. Chem. A* **2005**, *109*, 6056.

(47) Tang, W. Y.; Tranter, R. S.; Brezinsky, K. *J. Phys. Chem. A* **2006**, *110*, 2165.

(48) Sendt, K.; Bacskay, G. B.; Mackie, J. C. *J. Phys. Chem. A* **2000**, *104*, 1861.

(49) Ervin, K. M.; DeTuri, V. F. *J. Phys. Chem. A* **2002**, *106*, 9947. $D_0(C_6H_5\text{-}H) = 111.3 \pm 0.5$ kcal mol^{-1} and $DH_{298}(C_6H_5\text{-}H) = 112.9 \pm 0.5$ kcal mol^{-1}

Chapter IV

Furfural and Benzaldehyde

4.1 Introduction

As was the case with furan in the previous chapter furfural is an important compound readily accessible from biomass. Furfural is one of the most widely distributed furans in nature, and can be obtained easily from agricultural materials that contain high concentrations of hemicellulose.[1-20] Hemicellulose is a branched, low molecular weight polymer composed of five carbon sugars. (Figure 4.1) About 150 sugar molecules polymerize to create hemicellulose which is in great contrast to cellulose, which contains only anhydrous glucose. Furfural first gained chemical notice when in 1922 the Quaker Oats Company began mass-producing it from oat hulls.[21] This opened new interest in the chemistry of furfural for production.[22]

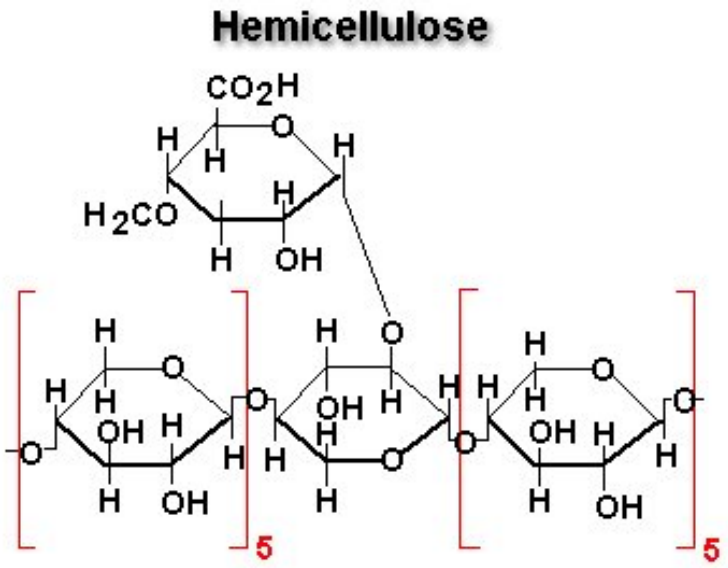

Figure 4.1 Generic structure for Hemicellulose

The reaction for the formation of furfural from hemicellulose currently is well understood in carbohydrate chemistry.[23-25] The reaction involves hydrolysis of pentosan into pentoses (mainly xylose) at temperatures of 473-523 K and in the presence of acid. Pentose undergoes a triple dehydration giving furfural[26] (Figure 4.2).

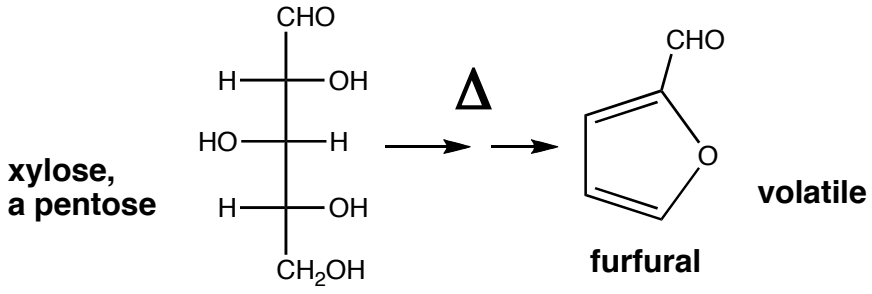

Figure 4.2 Conversion of Xylose to Furfural

Since it is well known that furfural is a thermal decomposition product of

Xylose,[25, 27-28] the experiments in this chapter explore the thermal fragmentation of furfural itself, which is not well understood.

The chemistry of furfural is well developed, and is even the subject of a recent book.[29] Furfural has also been the topic of several spectroscopic studies.[30-36] Although furfural has been the subject of several studies, to date there is little work that focuses on the direct thermal decomposition pathway in the gas phase. Two current works in the literature explore the thermal decomposition of furfural. The first is a 1932 study by Hurd *et al,*[22] and the second is a 1987 study by Grela *et al.*[37-38] Hurd *et al.* speculated that the products from the pyrolysis of furfural were furan and carbon monoxide. Greal *et al.* found vinylketene as the primary product using mass spectrometry.

Benzaldhyde is similar in structure to furfural and because of this it was explored in addition to furfural to see if a general decomposition pathway could be found.

4.2 Experimental Methods

The high temperature microtubular flow reactor described in chapter 2 section 2.2 (Figure 4.4) was used to decompose furfural. Thermal cracking products are produced by pulsing C_4H_4O-CHO (furfural) seeded in an inert gas (roughly 1 – 2 atm) through a resistively heated silicon carbide tube at high temperature (up to 1700 K) into a vacuum chamber (about 10^{-5} Torr). The valve fires at a nominal rate of 10–50 Hz and is open for roughly 250 μsec. The reader is refereed to Chapter III Section 3.2 for the experimental details. The same furan pyrolysis procedure was used for furfural.

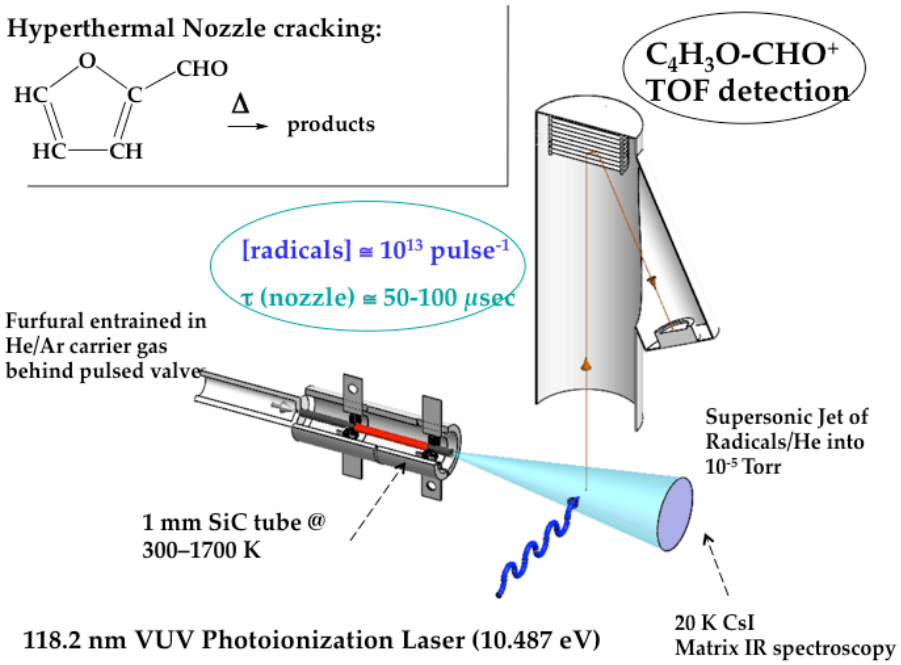

Figure 4.3 Schematic of Experimental set-up used to thermally decompose Furfural

4.3 Results

In Figure 4.3 are shown the PIMS spectra of the decomposition products of furfural. The bottom trace in Figure 4.3 is the mass spectrum that results when furfural (1 Torr C_4H_3O-CHO entrained in 2 atm He) transits the nozzle at room temperature (300 K). Photoionization with 118.2 nm VUV light produces the parent ion, m/z 96 C_4H_3O-CHO^+, and its isotope peak, m/z 97. The (97/98) isotope ratio is measured to be 6%. The *IE*(furfural) was measured to be 9.22 ± 0.01 eV; as the wall temperature of the nozzle is raised fragmentation of the parent ion C_4H_3O-CHO^+ is observed, with the loss of the hydrogen on the aldehyde group yielding C_4H_3O-CO^+ ion. When the wall temperature of the SiC nozzle is raised to 1300 ± 100 K, product ions at m/z 68 and 40 are observed which arise from ionization of C_4H_4O and CH_3CCH. Increasing the wall temperature to 1600 ± 100 K leads to an increase in the $C_3H_4^+$ and CH_3CCH^+ signals and new features at m/z 39, m/z 41 and m/z 42 are detected. The band at m/z 41 is consistent with the methylacetylene isotope peak. The (41/40) isotope ratio is calculated to be 3% for $C_3H_4^+$. The signal at m/z 39 is CH_2CCH^+ and is a diagnostic for the presence of the propargyl radical. The peak at m/z 42 belongs to the ketene ion: CH_2=C=O^+. Figure 4.4 is presented again from chapter 3 to show the thermal cracking of furan.

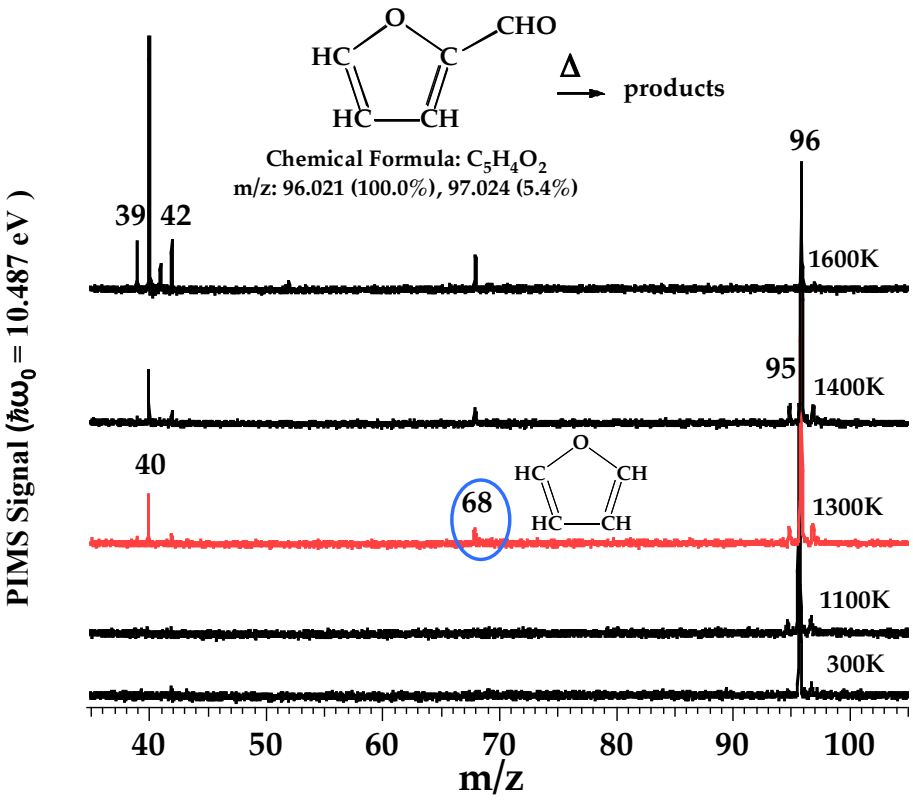

Figure 4.3 The bottom trace is the mass spectrum that results when furfural (1 Torr C_4H_3O-CHO entrained in 2 atm He) transits the nozzle at room temperature (300 K).

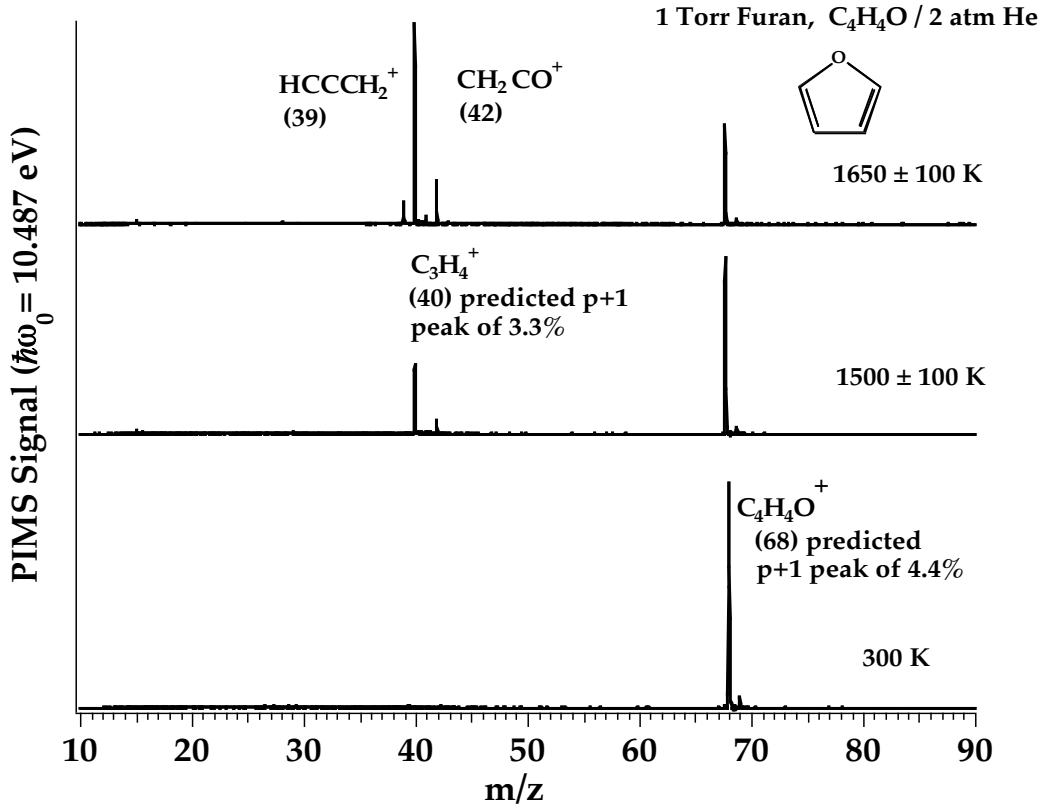

Figure 4.4 PIMS spectra of the decomposition products of furan in a high temperature supersonic nozzle. The bottom trace is the mass spectrum that results when furan (1 Torr C_4H_4O entrained in 2 atm He) transits the nozzle at room temperature (300 K).

The PIMS spectra in Figures 4.3 and 4.4 indicate that furfural decarbonlaytes to product furan, which subsequently decomposes as earlier observed:[39]

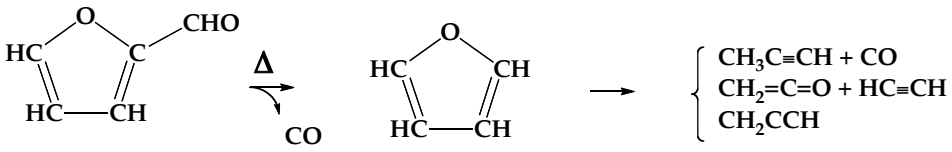

(4.1)

Figure 4.5 shows the PIMS spectra for the decomposition of d1-furfural with the deuterium in the aldehyde position. (C_4H_3O-CDO) d1-furfrual was synthesized. For details refer to Appendix B. The bottom trace in Figure 4.5 is the mass spectrum that results when d1-furfural (1 Torr C_4H_3O-CDO entrained in 2 atm He) transits the nozzle at room temperature (300 K). Photoionization with 118.2 nm VUV light produces the parent ion, m/z 97 C_4H_3O-CHO^+, and its isotope peak, m/z 98. The (98/97) isotope ratio is measured to be 6%. As the wall temperature of nozzle is raised fragmentation of the parent ion C_4H_3O-CDO^+ is observed, with the loss of the deuterium on the aldehyde group yielding the C_4H_3O-CO^+ ion. When the wall temperature of the SiC nozzle is raised to 1300 ± 100 K, product ions at m/z 69 and 41 are observed which arise from ionization of deutrated furan C_4H_3DO and deuterated methlyacetylene C_3H_3D. Increasing the wall temperature to 1600 ± 100 K leads to an increase in the $C_4H_3DO^+$ and $C_3H_3D^+$ signals and new features at m/z 39, m/z 40, m/z 42 and m/z 43 are detected.

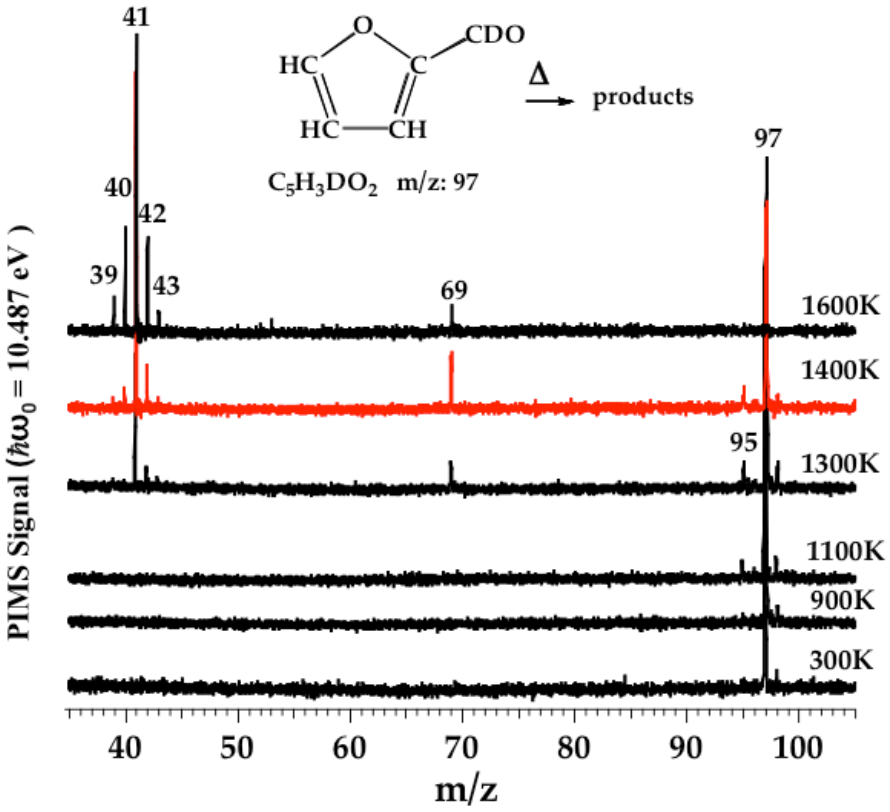

Figure 4.5 PIMS spectra of the decomposition products of d1-furfural.The bottom trace is the mass spectrum that results when D1-furan (1 Torr C_4H_3O-CDO entrained in 2 atm He) transits the nozzle at room temperature (300 K).

Figure 4.6 shows the PIMS spectra for the decomposition products from d1-furfural at a wall temperature of 1300 ± 100 K. As observed earlier furan decomposes via three different pathways. Knowing this becomes important when trying to determine if the deuterium was initially in the alpha (deuterium on carbon adjacent to oxygen) or beta (deuterium on second carbon away from oxygen) position on the furan ring. Initial deuterium location on the furan ring will dictate what products are seen. The PIMS spectrum in Figure 4.6 has features for $C_3H_3D^+$ m/z 41, CH_2CO^+ m/z 42, $CDHC{=}O^+$ m/z 43, $C_3H_2D^+$ m/z 40 and CH_2CCH^+ m/z 39. Figures 4.7 and 4.8 show the decarbonylation of d1-furfural to furan with the deuterium in the alpha and beta positions, respectively, and by followed the appropriate products.

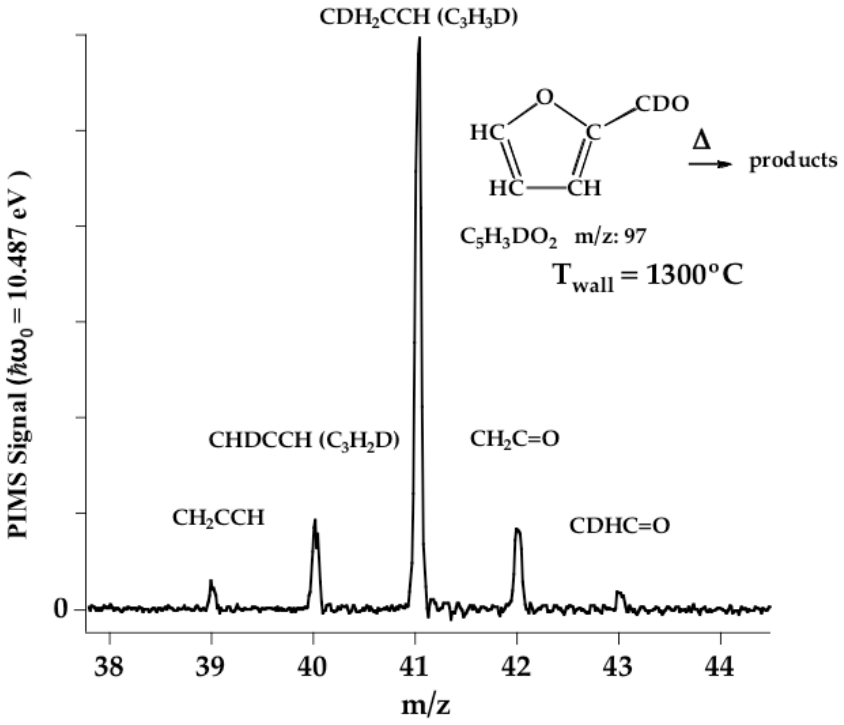

Figure 4.6 PIMS spectra of d1-fufural showing product peaks from thermal decomposition at 1300°C.

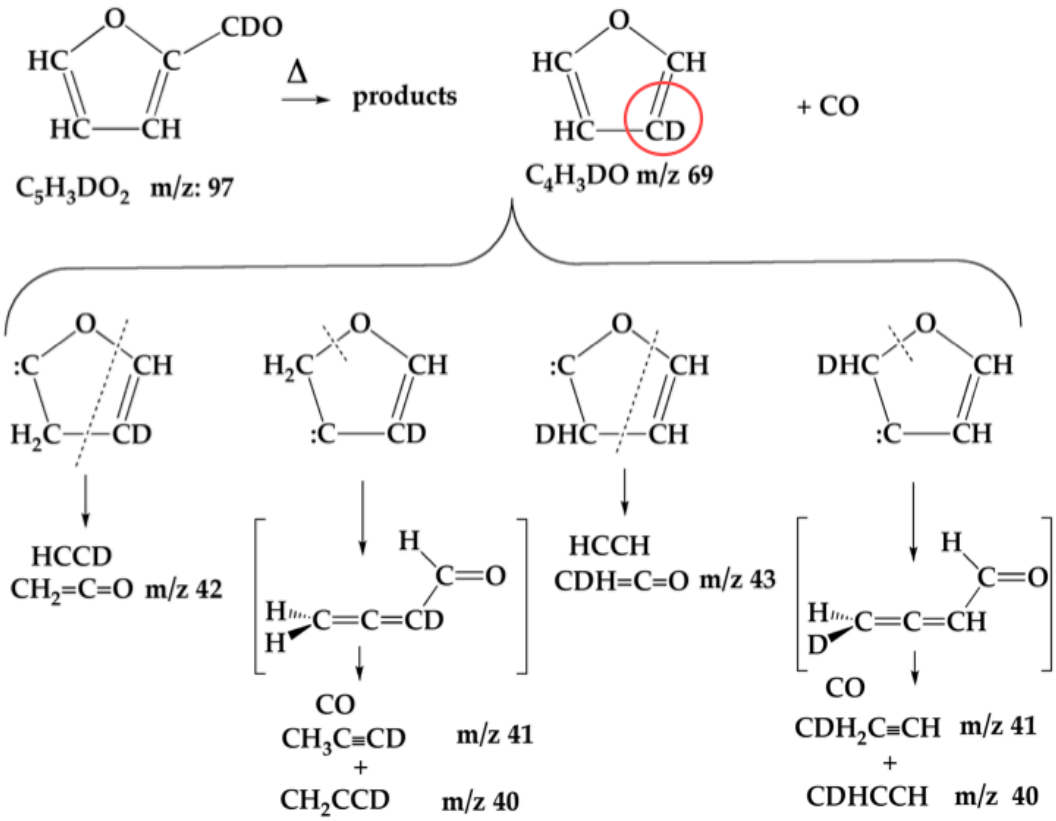

Figure 4.7 Thermal decomposition of d1-furfural to d1-furan. The above pathway shows the products that result when the deuterium atom from d1-furfural finishes on the β-carbon (circled in red) in furan.

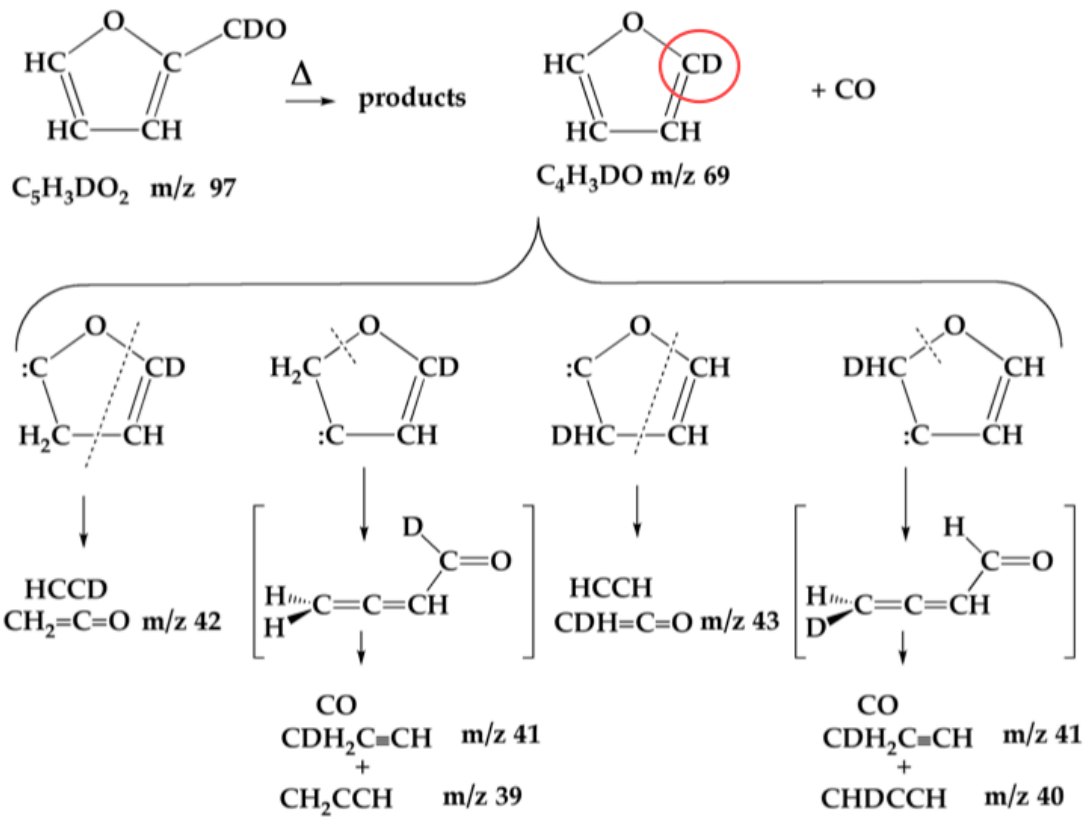

Figure 4.8 Thermal decomposition of d1-furfural to d1-furan. The above pathway shows the products that result when the deuterium atom from d1-furfural finishes on the α-carbon (circled in red) in furan.

The PIMS spectra in Figures 4.3 - 4.6 are very informative but they only identify molecular products by m/z, the mass-to-charge ratio. Matrix infrared spectroscopy was used to support the findings from the PIMS spectra. Furfural is a nonlinear molecule and will have 3N-6 vibrational degrees of freedom or 27 modes, with a cis and trans form. It was important to identify as many parent bands in furfural as possible in order to distinguish them from decomposition products of furfural. In Figure 4.9 the infrared spectra of parent furfural at 300 ± 100 K in the mid-IR is presented to show the congestion of the IR spectra of furfural. In Figure 4.10 the C=O stretching region and out-of-plane mode in furfural and d1-furfural are clearly resolved.

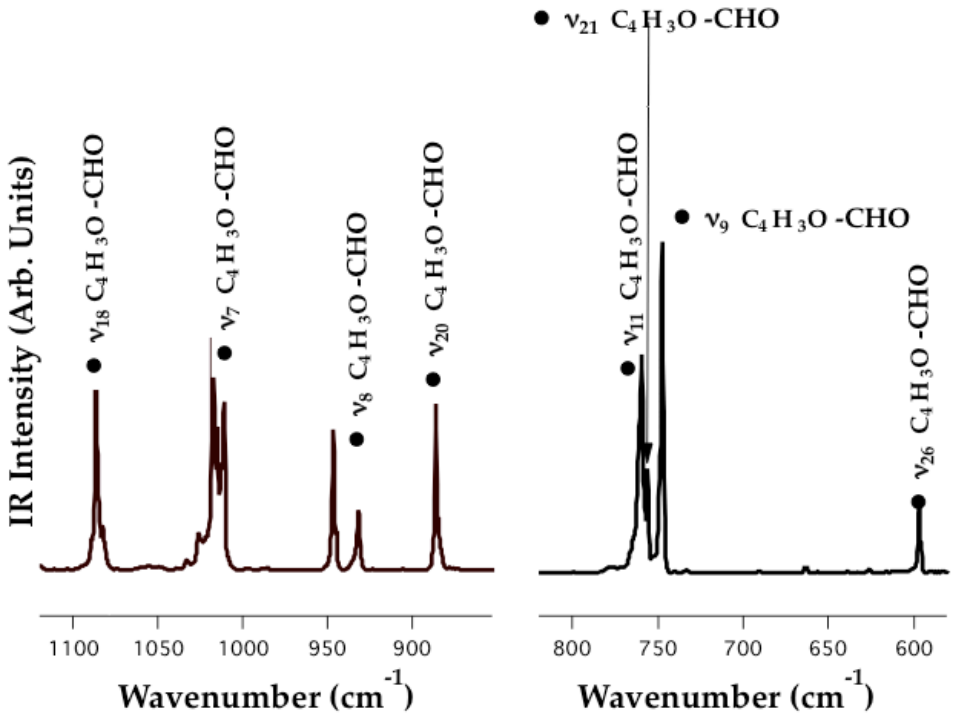

Figure 4.9 Matrix IR spectra at room temperature for furfural. Only a portion of the parent IR bands are shown although most were detected and assigned. Furfural has 27 active modes (3N-6, where N is number of atoms) in IR and a cis and trans form, making the IR spectrum very congested**.**

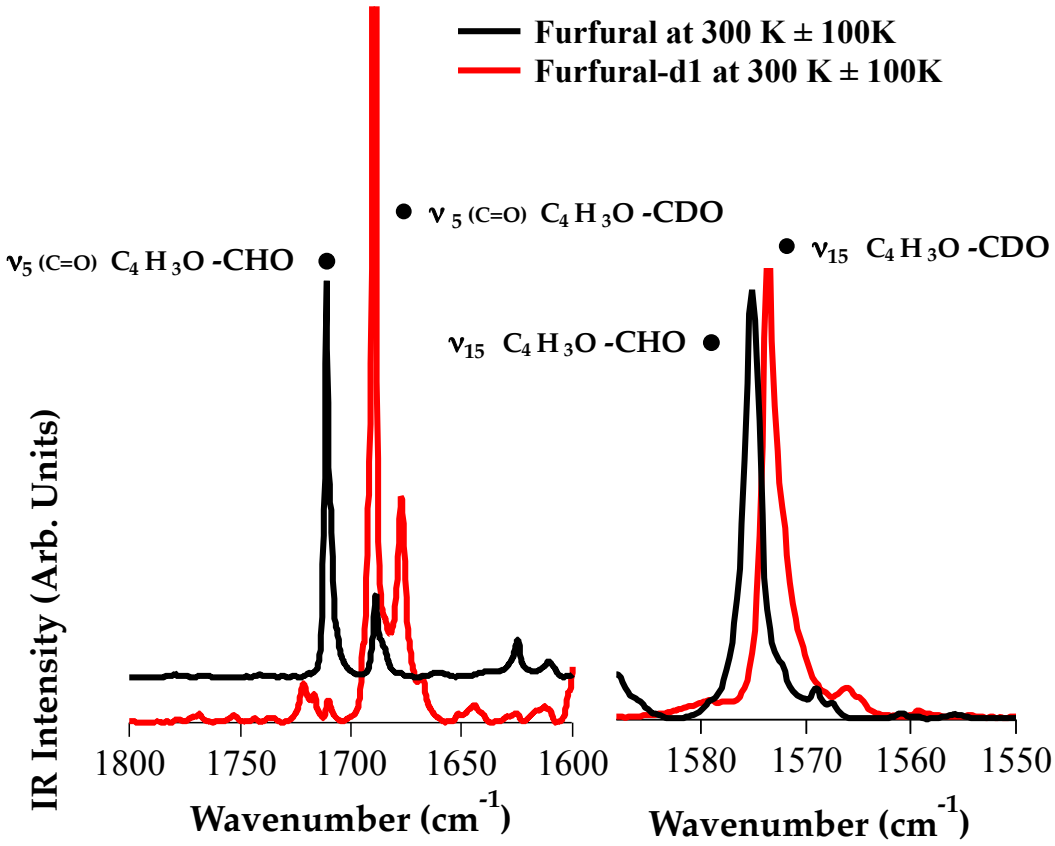

Figure 4.10 IR spectra comparing the ν5 and ν15 modes in furfural to those of d1-furfural. As expected the two modes are slightly off set with the d1-furfural bands lower in frequency. Recall that simple harmonic motion can be described by $\nu \propto \sqrt{(k/\mu)}$, where ν is the frequency for vibration, k is the force constant and μ is the reduced mass. H and D atoms will have the same force constant and only differ in mass. Since deuterium has a greater atomic weight than hydrogen, ν will be smaller (i.e., lower energy frequency) , which is evident in the above figure.

In Figure 4.11 and 4.12 are the infrared spectra of the decomposition products of furfural at 1300 ± 100 K. Figure 4.11 shows the CH in plane bends for furfural (C_4H_4O). Figure 4.12 reveals the decomposition products of furan with distinctive bands for CH_2=C=O and CH_3CCH clearly present. Recall from the PIMS spectra in Figures 4.3-4.6 that when furfural thermally decomposes to furan (m/z 68 or m/z 69) peaks for methylacetyelene (m/z 40 or m/z 41) are also present; as furan is formed in the hot reactor a portion immediately decomposes to subsequent products. Because of this we were unable to isolate furan only in the matrix before it decomposed to appropriate products.

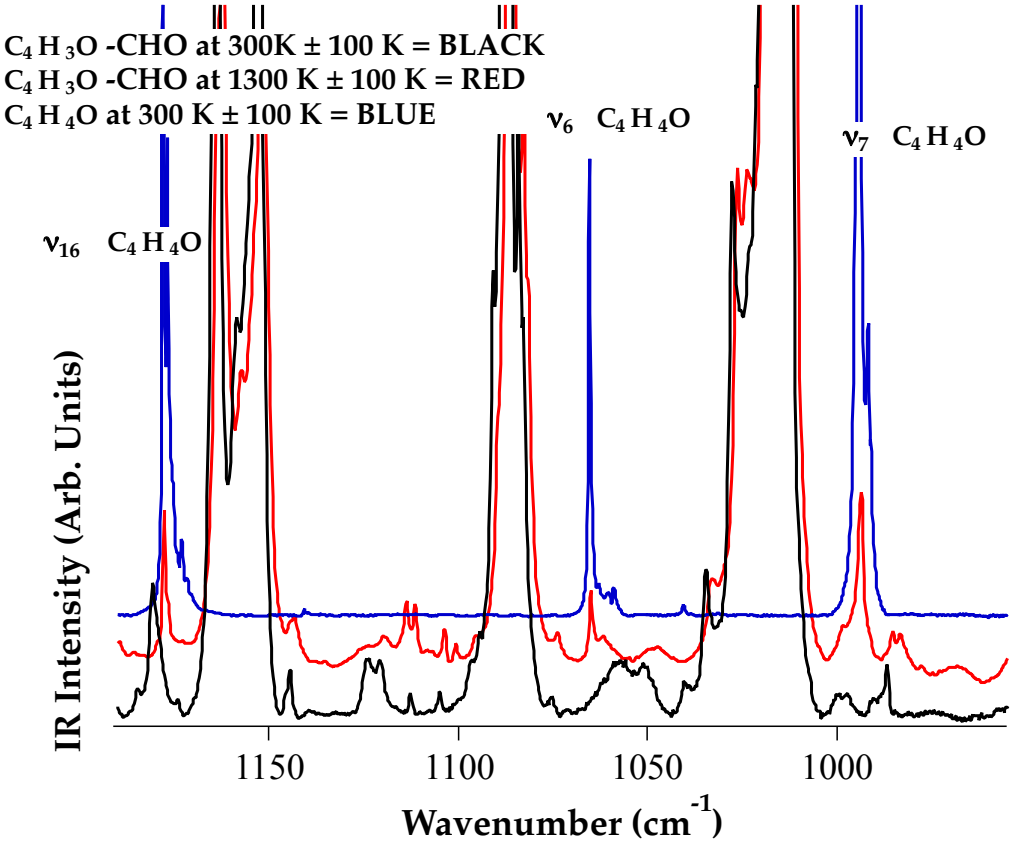

Figure 4.11 Infrared spectrum of the decomposition product furan from furfural**.**

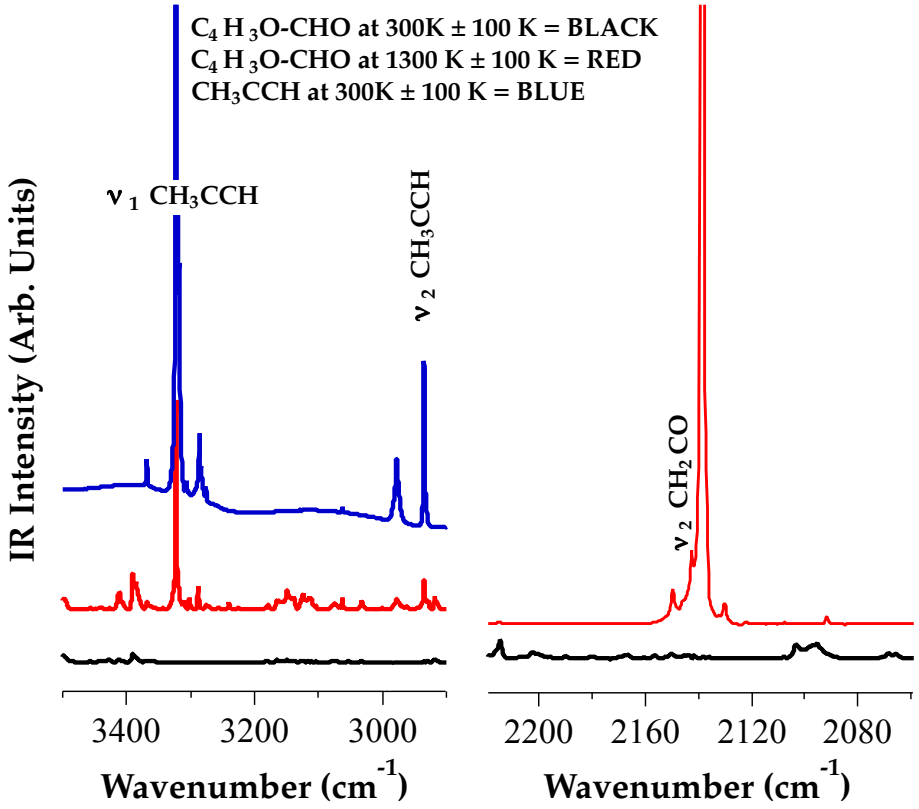

Figure 4.12 IR spectra of the decomposition products methylacetylene CH_3CCH and ketene $CH_2=C=O$ from furfural at 1300 K.

Benzaldehyde was studied with the microtubular reactor because it is similar in structure to furfural and thus should mechanistically decompose in a similar manner, however, the primary product is benzene (C_6H_6) rather than furan. Benzene, unlike, furan should not further crack because the lowest energy bond in benzene is the C-H bond at 112.9 ± 0.6 kcal/mol[40] which is beyond the energy range of the microtubular reactor. In Figure 4.13 are shown the PIMS spectra for the decomposition of benzaldehyde. The bottom trace in Figure 4.13 is the mass spectrum that results when benzaldehyde transits the nozzle at room temperature (300 K). Photoionization with 118.2 nm VUV light produces the parent ion, m/z 106 C_6H_5-CHO^+, and its isotope peak, m/z 107. The *IE*(benzaldehyde) was measured[41] to be 9.50 ± 0.02 eV; as the wall temperature of the nozzle is raised fragmentation of the parent ion C_6H_5-CHO^+ is observed, with the loss of the hydrogen on the aldehyde group yielding C_6H_5-CO^+ ion. When the wall temperature of the SiC nozzle is raised to 1300 ± 100 K, a product ion at m/z 78 appears.

Resonance-enhanced multiphoton ionization (REMPI) was used to confirm that m/z 78 is benzene. In REMPI, a photon from a tunable laser resonantly excites a ground electronic state (S_0) of a molecule to an excited vibronic level in the S_1 state. An additional photon is then absorbed to ionize the electronically excited molecule. The 1+1 REMPI used for benzaldehyde experiments has been described previously in detail.[42] Benzene is ideal for 1+1 REMPI because the lowest singlet-singlet ($S_1 \leftarrow S_0$) transition is near 259.1 nm (4.7 eV). A second photon of 4.7 eV is adequate to reach the ionization potential of benzene at 9.24 eV.

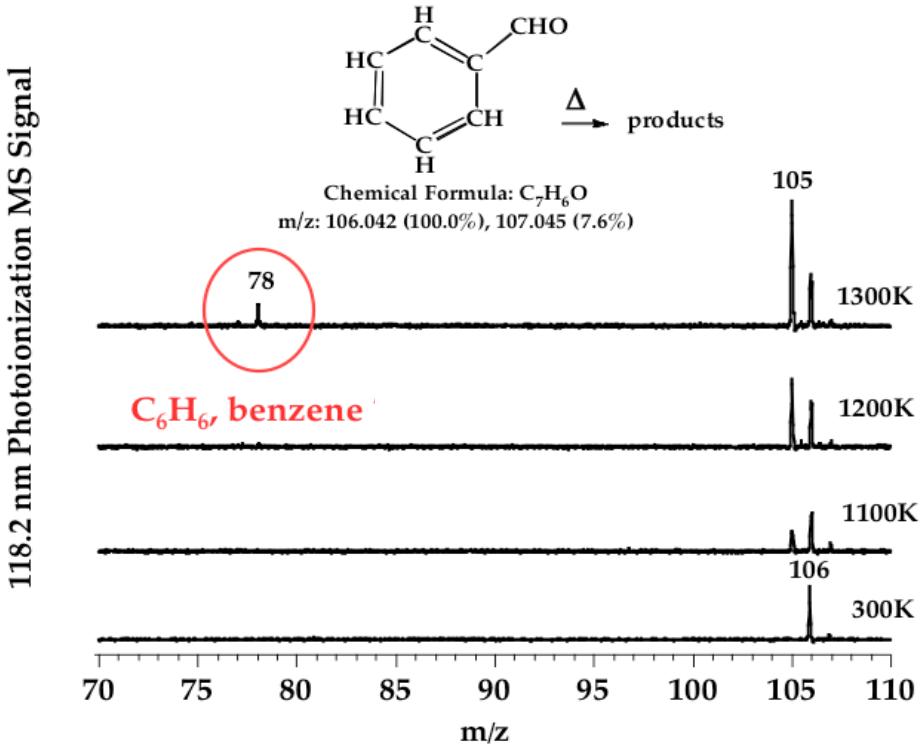

Figure 4.13 The bottom trace is the mass spectrum that results when benzaldehyde transits the nozzle at room temperature (300 K). As was the case with furfural decomposing to furan, benzaldehyde decomposes to benzene.

Figure 4.14 shows the REMPI mass spectra obtained at different wavelengths for benzaldehyde pyrolysis at different temperatures. The bottom trace in Figure 4.14 is taken at 475 K on a strong resonance of benzene, 259.05 nm. As expected no signal for benzene is present at this temperature. The middle trace in Figure 4.14 is a scan at 1475 K tuned approximately 1 nm off the benzene resonance and there is no signal for benzene, which should be present at this temperature from thermal cracking of benzaldehyde. The top trace shows the REMPI mass spectrum at 1475 K with light tuned on a strong benzene resonance and a strong signal at m/z 78, benzene, dominates the mass spectrum. In Figure 4.15, the REMPI spectrum of the m/z 78 species observed in benzaldehyde pyrolysis at 1475 K is compared to the REMPI spectrum of a prepared benzene standard from 258-268 nm. The excellent agreement between the two spectra is definitive proof that m/z 78 is benzene. The peak at 259.1 nm is the well-known $^1B_{2u}$ (ν_6 ν = 1) ← $^1A_{1g}$ (ν_6 ν = 0) benzene transition.[43-45] All other features in Figure 4.14 spectra closely match a previous assignment of benzene transitions.[45]

A final confirmation that the pyrolysis of benzaldehyde results in benzene is presented in the matrix IR spectra shown in Figure 4.16, it is clear that the new peaks that grow in at 1275 K belong to ν_4, ν_{12}, and ν_{13} of benzene.

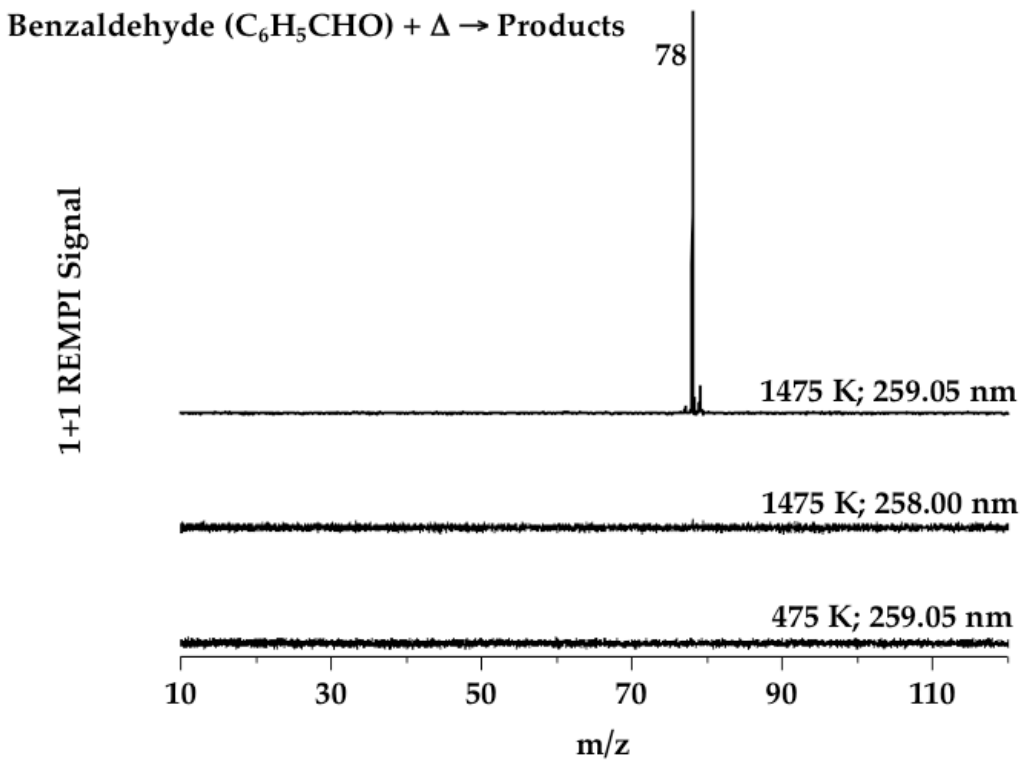

Figure 4.14 Resonance-enhanced multiphoton ionization TOF mass spectra of benzaldehyde pyrolysis at 1475 K at different wavelengths.

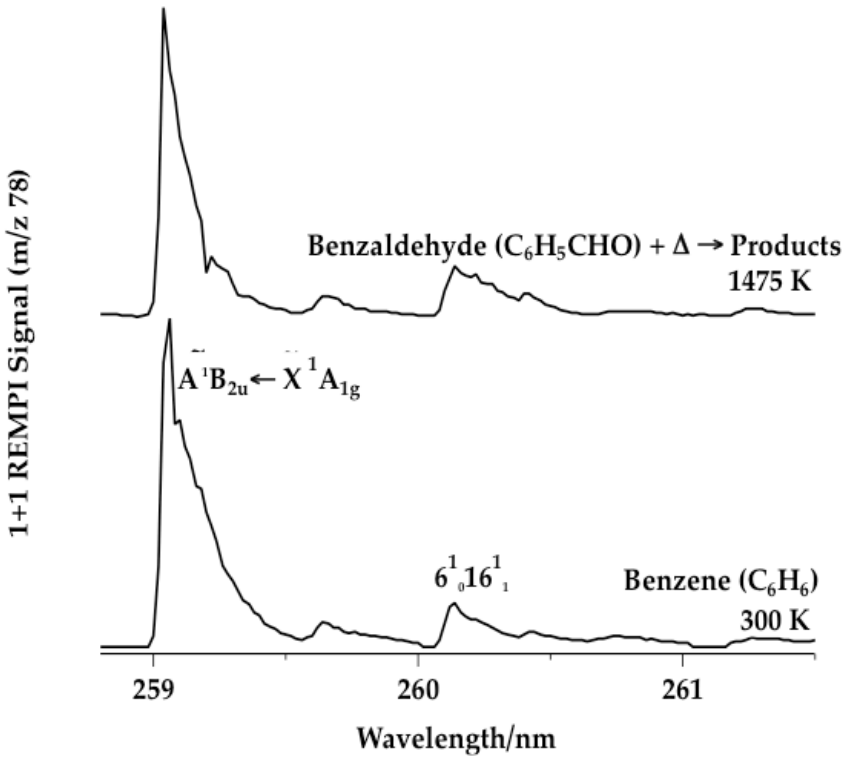

Figure 4.15 Upper curve 1+1 REMPI ionization scan of m/z 78 observed from benzaldehyde pyrolysis at 1475 K recorded with a 0.02 nm step size. The bottom curve is a 1+1 REMPI ionization scan of m/z 78 for the benzene standard recorded with 0.05 nm step size. Assignments of the $^1B_{2u}$ (ν_6 ν = 1) ← $^1A_{1g}$ (ν_6 ν = 0) transitions are based on the work by Atkinson and Parmenter[46]

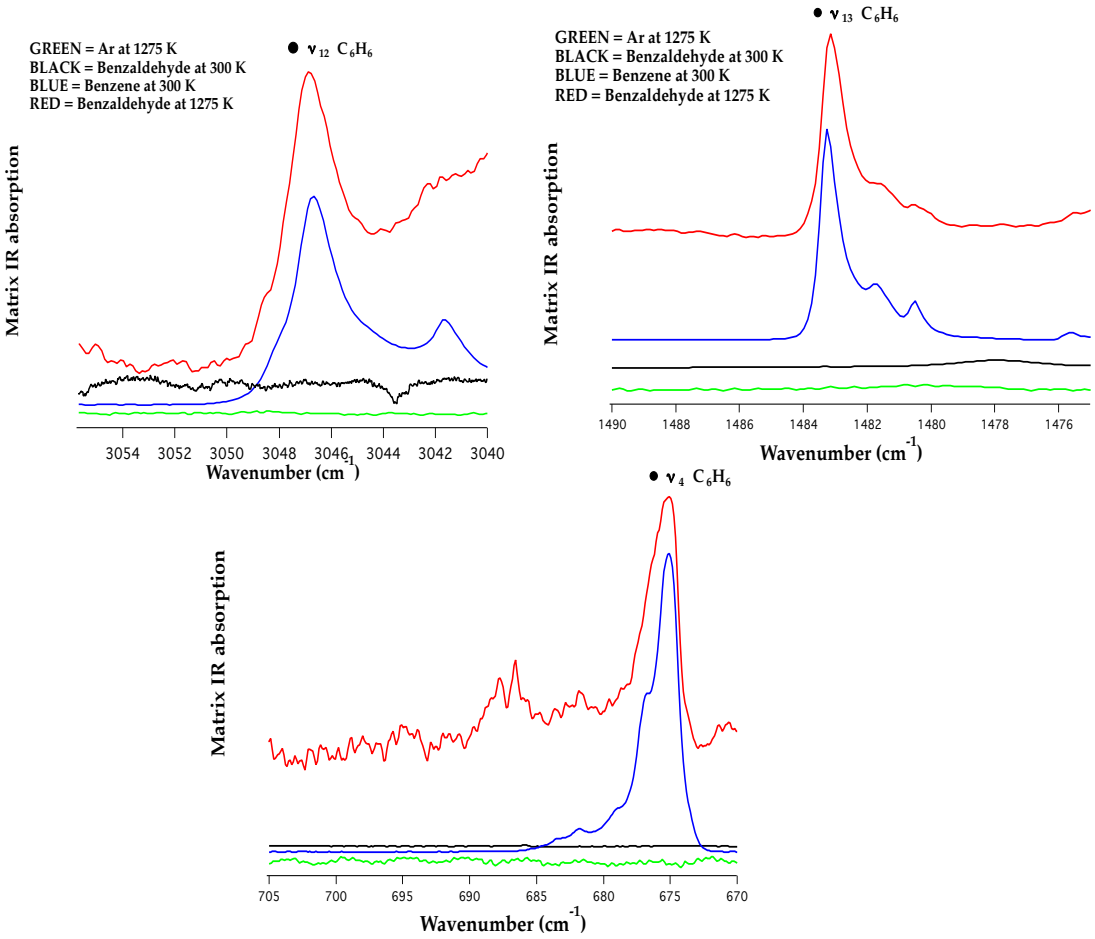

Figure 4.16 Infrared spectra of the decomposition product benzene from benzaldehyde**.**

4.4 Discussion and Conclusions

These experiments have enabled us to identify the initial thermal cracking products of furfural and benzaldehyde. Using a high-temperature nozzle as a tubular reactor, we have demonstrated that furfural thermally cracks to produce furan which subsequently cracks to form: CO + CH_3CCH, HCCH + CH_2CO and propargyl radical (CH_2CCH). D1-furfural was found to thermally crack to produce d1-furan that further cracks to form appropriately labeled products. All of these species are detected by both the PIMS and IR spectrometers in Figures 4.2 - 4.12. In the case of d1-furfural the product furan can have the deuterium in the alpha or beta position. It was no possible to distinguish between a C-D stretch in the α-furan or the β-furan product. Therefore the PIMS spectra were used to determine if d1-furfural decarbonlaytes to α-furan, β-furan or a combination of the two. This is an important mechanistic detail in the decomposition of furfural because it establishes where the aldehydic hydrogen on furfural ends up on the furan ring. The PIMS of d1-furan alone could determine which form of furan is present but since the products of furan decomposition are well known we can use this information to determine which furan is produced from thermal cracking of furfural. Figure 4.7 presents the decomposition pathway of β-furan and Figure 4.8 shows the decomposition pathway of α-furan. Figures 4.7 and 4.8 show that the only decomposition product that differs between α-furan and β-furan is propargyl radical. If only β-furan was produced then we would expect to see only deuterated propargyl radical (m/z 40). If α-furan is present we expect to see undeuterated propargyl radical (m/z 39). Figure 4.17 shows the two routes to form propargyl radical via α and β furans.

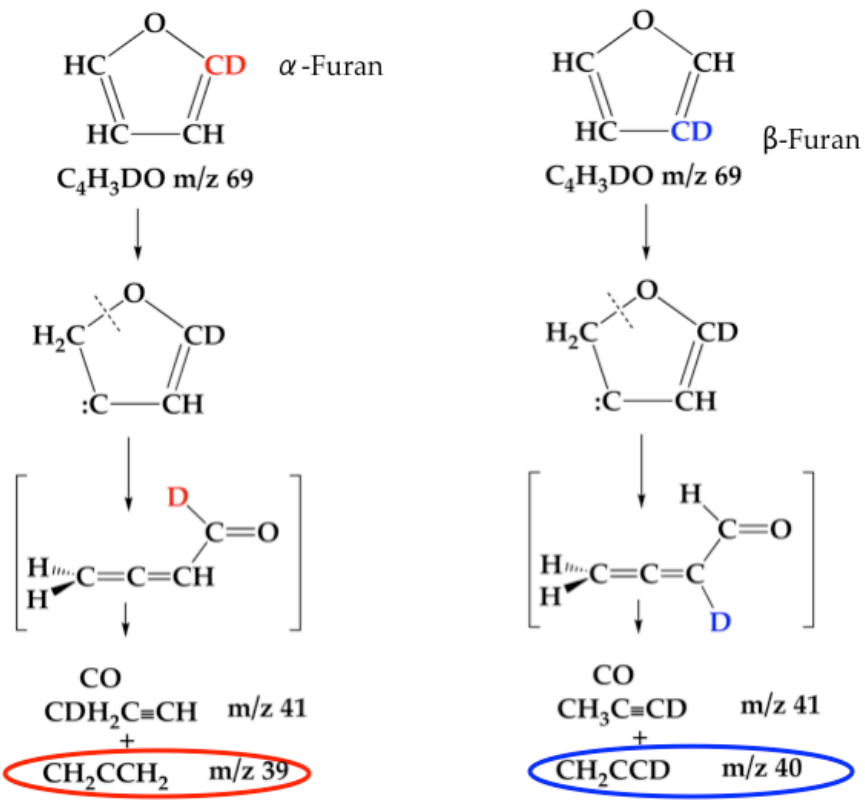

Figure 4.17 Comparison of products from the thermal decomposition of α and β furans

The PIMS in Figures 4.5 and 4.6 show features at m/z 39 and m/z 40. This would indicate that both CH_2CCH and CH_2CCD are present and thermal cracking of d1-furfural results in a combination of α and β furan. Propagyl radical is a trace channel in the decomposition of furan and was difficult to detect in previous furan studies. We were unable to detect propargyl radical in the matrix IR spectra from thermal cracking of furfural.

The thermal cracking of benzaldehyde parallels that of furfural. It is shown in Figures 4.13-4.16 by PIMS, 1 + 1 REMPI and IR that benzaldehyde thermally cracks to form benzene.

All the PIMS and IR spectra of furfural and d1-furfural reveal that furfural and d1-furfural first decompose to furan and then subsequently crack to expected products. Benzaldehyde overwhelmingly supports this mechanistic pathway. The next question is how furfural initially decarbonlaytes to form furan. Figure 4.18 is a proposed mechanism for the thermal cracking of d1-furfural.

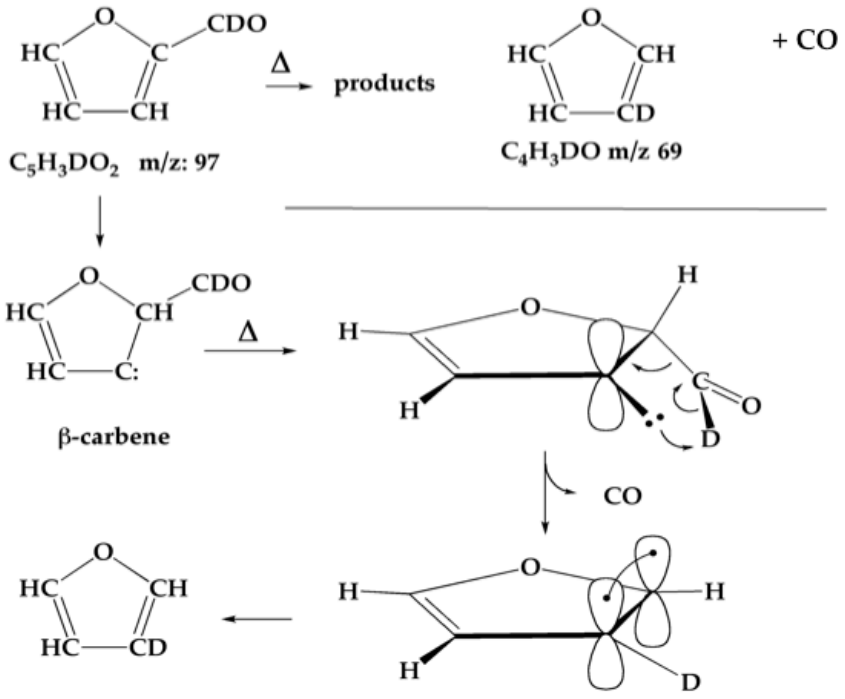

Figure 4.18 Possible mechanism for how furfural decarbonlaytes furfural to furan.

The mechanism presented in Figure 4.18 for d1-furfural would explain the formation of β-furan but not α-furan. Attempts have been made to calculate the pathway from furfural to furan via the β-carbene intermediate but the calculation fails. All the PIMS, IR and REMPI

experiments are conclusive in that furan and benzene are the thermal cracking products of furfural and benzaldehyde. Since current calculations cannot provide insight on the pathway from furfural to furan, we present the mechanism in Figure 4.18 as the most logical pathway. If the mechanism in Figure 4.18 is correct then only the β-furan is formed. Since the PIMS in Figure 4.5 has a feature for propargyl radical at m/z 39 this indicates that α-furan is also formed. An explanation for the presence of the α-furan is that after the β-furan is formed the hydrogen and deuterium exchange positions on the ring, leading to the formation of the α-furan. A microwave experiment would be very helpful in testing the mechanism in Figure 4.18 because the α-furan and β-furan would have different rotational constants and thus could be distinguished from each other and their respective amounts determined.

References for Chapter IV

(1) Deanm F.M. Naturally *Occuring Ring Compounds*, Butterworths, London. **1963**

(2) Robertson, G.L and Samaniego, C.M.L, *J. Food Sci*. **1986**, *51*, 184.

(3) Kaanane, A., Kane, D., and Labuza, T.P., *J. Food Sci*. **1988**, *53*, 1470.

(4) EI-Nemur, S. E., Ismail, I. A., and Askar, A., *Food Chem*. **1988**, *10*, 269

(5) Calvi, J. P. and Francis, F. J., *J. Food Sci*. **1978**, *43*, 1448.

(6) Rapp, A., Guntert, M., and Ullemeyer, H., *Z. Lebensm. Unters. Forsch*. **1985**, *180*, 109.

(7) Simpson, R. F., *J. Sci. Food Agric*. **1980**, 31, 214-222.

(8) Howe, U.S., J. S., Johnston, D., and Vojodic, P. R., *Anal. Proc*. **1988** *25*, 162.

(9) Service, E. G., Shinnie, G. B., and MacLeod, T. M., *J. Clin. Hosp. Pharm*. **1982** *7*, 287.

(10) Hung, C. T., Selkirk, A. B., and Taylor, R. B., *J. Clin. Hosp. Pharm*. **1982** *7*, 17.

(11) Schwald, W., Brownell, H. H., and Saddler, J. N., *J. Wood Chem.* Technol. **1988**, *8*, 543.

(12) Bobleter, O., Schwald, W., Concin, R., and Binder, H., *J. Carbohydr. Chem*. **1986**, *5*, 387.

(13) Bonn, G., and Bobleter, O., *Chromatographia* **1984**, *18*, 445.

(14) Chapman, G. W., Burdick, D., Higman, H. C., and Robertson, J. A., *J. Sci. Food Agric*. **1978**, *29*, 312.

(15) Garrett, E. R. and Dvorchik, B. H., *J. Pharm. Sci.*, **1969**, *58*, 813.

(16) Grohmann, K., Himmel, M., Rivard, C., Tucker, M., and Baker, *J. Biotechnol. Bioeng. Symp.* **1984**, *14*, 138.

(17) Grohmann, K., Torget, R., and Himmel, M., *Biotechnol. Bioeng. Symp.* **1985**, *15*, 59.

(18) Rivard, C. J., Himmel, M. E., and Grohmann, K., *Biotechnol. Bioeng. Symp*. **1985**, *15*, 375.

(19) Grohmann, K., Torget, R., and Himmel, M., *Biotechnol. Bioeng. Symp.* **1986**, *17*, 135.

(20) McCarty, P. L., Young, L. Y., Stuckey, D. C., and Healy, J. B. Jr. *Microbial Energy Conversion*, Schlegel, H. G. and Barnea, J., eds., Pergamon, Oxford **1977**, 179.

(21) Kottke, R. H. In Kirk-Othmer *Encyclopedia of Chemical Technology*, 4th ed.; Kroschwitz J., Howe-Grant M., Eds.; John Wiley and Sons: New York, **1998**; volume supplement.

(22) Hurd, C.D., Goldsby, A.R., and Osborne, E.N., *J. Amer. Chem. Soc.* **1932**, *54*, 2532

(23) Garrett, E. R. and Dvorchik, B. H., *J. Pharm. Sci*. **1969**, 58, 813.

(24) Grohmann, K., Himmel, M., Rivard, C., Tucker, M., and Baker, J., *Biotechnol. Bioeng. Symp.* **1984**, 14, 138-157.

(25) Demirbas, A., *Fuel Processing Technology,* **2007**, *88*, 591.

(26) Antal, M. J.; Leesoboom, T.; Mok, W. S. Richards, G. N., *Carbohydr. Res.* **1991**, *217*, 71.

(27) Evans, R.J., Milne, A., *Energy and Fuels*, **1987**, 1, 123.

(28) Evans, R.J., Milne, A., *Energy and Fuels*, **1987**, 1, 311.

(29) Zeitsch, K. J. *The chemistry and technology of furfural and its many by-products*, 1st ed.; Elsevier: Amsterdam, **2000**; Vol. 13.

(30) Bak, B.; Christensen,D.; Dixon, W. B.; Hansen-Nygaard, L.; Rastrup- Andersen, J.; Schotlander, M., *J. Mol. Spectrosc*. **1962**, *9*, 124.

(31) Rico, M.; Barrachina, M.; Orza, J. M., *J. Mol. Spectrosc.* **1967**, *24*, 133.

(32) Monnig, M.; Dreizler, H.; Rudolph, H. D**.** 2. *Nafurforsch.,* **1965**, *20a*, 1323.

(33) Monnig, H. D.; Dreizler, H.; Rudolph, H. D. 2. *Narurforsch.,* **1966**, *21a*, 1633.

(34) Schultz, G.; Fellegvbry, I.; Kolonits, M.; Kiss, A. I.; Pete, B.; Bbnki, J., *J. Mol. Struct*. **1910**, *50*, 325.

(35) Miller, J.; Fateley, W. G.; Witkowski, R. E., *Spectrochim. Acta,* **1967**, *23a*, 891.

(36) Little, T. S.; Qiu, J.; Durig, J. R., *Spectrochim. Acta* **1989**, *45a*, 789**.**

(37) Grela, M.A. and Colussi, A.J., *J. Phys. Chem*., **1986**, *90*, 434.

(38) Grela, M.A. and Colussi, A.J., *An. Asoc. Quim. Aregent*., **1987**, *75*, 111.

(39) Vasiliou, A.K., Ellison, G.B., Nimlos. M.R., and Daily, J.W., *J. Phys. Chem. A,* **2009**, 13 (30), 8540-8547

(40) Ervin, K. M.; DeTuri, V. F. *J. Phys. Chem. A* **2002**, *106*, 9947. $D_0(C_6H_5\text{-}H) = 111.3 \pm 0.5$ kcal mol^{-1} and $DH_{298}(C_6H_5\text{-}H) = 112.9 \pm 0.5$ kcal mol^{-1}

(41) Chewter, L.A.; Sander, M.; Muller-Dethlefs, K.; Schalg, E.W., *J. Chem*. *Phys*., **1987**, *86*, 4737.

(42) Mukarakate, C., Scheer, A.M., Robichaud, D.J., Jarvis, M.W., David, D.E., Ellison, G.B., Nimlos M.R. and Davis, M.F., *Rev. of Sci. Instr.,* **2011**, *82*, 3104.

(43) Knight, A. E. W.; Parmenter, C. S.; Schuyler, M. W., J. *Am. Chem. Soc*. **1975,** *97***,** 1993**.**

(44) Page, R. H.; Shen, Y. R.; Lee, Y. T., *J. Chem. Phys*. **1988**, *88*, 5362.

Chapter V

Acetaldehyde

5.1 Introduction

This chapter describes the gas phase, thermal decomposition of dilute samples of acetaldehyde in an atomic buffer gas. The goal is to identify the uncatalyzed, unimolecular decomposition products.

$$CH_3CHO + (He \text{ or } Ar) \rightarrow \text{products} \quad \textbf{(5.1)}$$

The experiments in (5.1) are carried out by passing a dilute mixture of CH_3CHO (roughly 0.1%) entrained in a stream of a buffer gas (1 atm of either He or Ar) through a heated 2 cm x 1 mm SiC microtubular (μtubular) reactor. Common pressures in the μtubular reactor are 50 – 200 Torr and the SiC tube is heated in the range of 1175 — 1675 K. Typical transit times through the μtubular reactor are 50 — 100 μsec after which the gas mixture is formed into a skimmed molecular beam in a nominal vacuum of 10^{-5} Torr. The products in (5.1) are identified by vacuum ultraviolet (VUV) photoionization mass spectroscopy (PIMS) as well as by infrared (IR) absorption spectroscopy in a cryogenic matrix. This combination of PIMS and IR spectroscopy enables us to identify the products in (5.1) as: CH_3, CO, CH_2=C=O, CH_2=CHOH, H_2O, and HC≡CH. All efforts to identify CH_4 as a reaction product failed.

The thermal decomposition of acetaldehyde has been extensively studied in shock tubes, flow reactors, and flames over the last 75 years.[1-7] Our present views of the thermal cracking of

CH_3CHO are based on the early analysis of Rice and Herzfeld.[2] The Rice-Herzfeld mechanism for acetaldehyde decomposition is now widely accepted.[8] It consists of an initiation step:

$$CH_3CHO + M \rightarrow CH_3 + HCO + M \quad \textbf{(5.2)}$$

The succeeding radical propagation steps are:

$$HCO + M \rightarrow H + CO + M \quad \textbf{(5.3)}$$

$$H + CH_3CHO \rightarrow H_2 + CH_3CO \quad \textbf{(5.4)}$$

$$CH_3 + CH_3CHO \rightarrow CH_4 + CH_3CO \quad \textbf{(5.5)}$$

$$CH_3CO + M \rightarrow CH_3 + CO + M \quad \textbf{(5.6)}$$

The chain termination step is identified as:

$$CH_3 + CH_3 \rightarrow CH_3CH_3 \quad \textbf{(5.7)}$$

In some of the early research, the thermal disintegration of CH_3CHO was studied by experiments in a static 515 mL quartz bulb which were carried out over a temperature range of 750 — 800 K; the products were identified by gas-chromotography (GC) with flame ionization (FID) detection.[9,10] In the mid 1970s, the high temperature (> 1000 K) pyrolysis of CH_3CHO (approximately 1% in 1 atm of N_2) was examined in a turbulent flow reactor.[3] Total reaction time in the 1 m flow tube was 50 — 100 msec; product detection was by GC-FID analysis. The products detected following acetaldehyde pyrolysis were (in order of decreasing importance): CO, CH_4, H_2, CH_3CH_3, and CH_2CH_2. Small amounts of CH_3COCH_3, $CH_3CH_2CH_3$, CH_3CHCH_2, and HCCH were observed but no traces of CH_2CO were found. It was concluded that if the

essential Rice-Herzfeld scheme, eqs (5.2) — (5.7), was supplemented by an additional set of reactions, eqs (5.8) — (5.12), then a satisfactory account of all of the observed pyrolysis products could be achieved.

$$CH_3 + CH_3CH_3 \rightarrow CH_4 + CH_2CH_3 \quad \textbf{(5.8)}$$

$$H + CH_3CH_3 \rightarrow H_2 + CH_2CH_3 \quad \textbf{(5.9)}$$

$$CH_2CH_3 \rightarrow H + CH_2CH_2 \quad \textbf{(5.10)}$$

$$CH_3 + CH_3CHO \rightarrow CH_4 + CH_2CHO \quad \textbf{(5.11)}$$

$$CH_2CHO + M \rightarrow H + CH_2CO + M \quad \textbf{(5.12)}$$

In addition to pyrolysis studies in static reactors or turbulent flow tubes, acetaldehyde oxidation in a jet-stirred reactor was investigated at high temperature (900 —1300 K) in the pressure range 1-10 atm. Molecular species concentration profiles of O_2, H_2, CO, CO_2, CH_2O, CH_4, HCCH, CH_2CH_2, CH_3CH_3, CH_3CHCH_2 and CH_3CHO were obtained by probe sampling and GC analysis.[11] The classic pyrolytic decomposition of acetaldehyde was further examined at the higher temperatures used in combustion and also lower pressures with 85 laser-schlieren, shock-tube measurements[12] of density gradient covering 40 — 500 Torr and 1550 — 2400 K.

The thermal decomposition of acetaldehyde, eq: (5.2), and the bimolecular reaction, eq. (5.4), have been studied behind reflected shock waves with argon as the bath gas and using H-atom resonance absorption spectrometry as the detection technique.[13] In a related study, the use of an unreversed light source provided an extraordinarily sensitive H atom detection.[14] The thermal dissociation of acetaldehyde has been studied with the reflected shock tube technique

(1151-1354 K) using H(D)-atom atomic resonance absorption spectrometry detection. It was possible to measure both the total CH_3CHO decomposition rate and the branching to radical versus molecular channels. The experimental observations also provide a measure of the rate coefficient for H + CH_3CHO, eq. (5.4).

More recently, the pyrolysis and oxidation of acetaldehyde were studied behind reflected shock waves in the temperature range 1000-1700 K at total pressures between 1.2 and 2.8 atm. The study was carried out using a variety of time-resolved spectroscopic detection techniques. IR-laser absorption at 3.39 μm (2950 cm^{-1}) monitored acetaldehyde decay and UV absorption at 200 nm tracked the CH_2CO and CH_2CH_2 product formation rates. The radicals were detected by UV absorption at 216 nm (CH_3) and UV absorption at 306.7 nm (OH). Time-resolved IR emission at 4.24 μm (2358 cm^{-1}) detected the CO_2 formation rate and emission at 4.68 μm (2137 cm^{-1}) monitored the CO and CH_2CO formation rates.[15] With these techniques it was possible to observe CH_4, CH_3CH_3, CH_2CH_2, and CH_2CO as pyrolysis products.

Acetaldehyde decomposition has also been scrutinized in flames. The combustion of several flames using acetaldehyde as a fuel was measured in three $CH_3CHO/O_2/Ar$ flat premixed flames stabilized at low pressure (50 mbar). The experimental setup consists of a molecular beam mass spectrometer system (MBMS) combined with electron impact ionization (EI).[16]

To understand reaction (5.1), it is important to have a firm grasp of the thermochemistry of acetaldehyde. All of the bond energies of CH_3CHO have been measured. The weakest bond[17] in acetaldehyde is the C-C bond; $DH_{298}(CH_3\text{-}CHO)$ = 84.8 ± 0.2 kcal mol^{-1} while the acyl C-H bond is $DH_{298}(CH_3CO\text{-}H)$ = 89.3 ± 0.4 kcal mol^{-1}. The remaining methyl C-H bond energy must be extracted from the negative ion acidity/*EA* cycle.[18-20] The acidity of acetaldehyde, $\Delta_{acid}H_{298}$(H-

CH_2CHO), has been measured[21,22] as 365.9 ± 2.2 kcal mol^{-1} and the electron affinity of the vinyloxy radical, $EA(CH_2CHO)$, is found[23] to be $1.8248^{+0.0002}_{-0.0006}$ eV. Consequently one finds[24] $DH_{298}(H\text{-}CH_2CHO)$ = 94 ± 2 kcal mol^{-1}. A summary of these bond energies and related processes is collected in Table 5.1.

5.2 Experimental Methods

The studies in this chapter focus on the thermal decomposition of all of the isotopomers of acetaldehyde, CH_3CHO, CH_3CDO, CD_3CHO, and CD_3CDO. We have studied the thermal cracking of all isotopomers in a heated microtubular (μtubular) reactor as explained previously.[18] A dilute sample of acetaldehyde is mixed with an inert carrier gas and passed through the heated SiC tube The general valve was removed for all experiments done at ALS, to allow for a continuous gas flow through nozzle. A continuous flow of gas was needed to obtain reasonable ion signal. Gases exiting the μtubular reactor emerge in an under-expanded jet at roughly 10^{-5} Torr. The translational, vibrational, and rotational temperatures drop rapidly within a few diameters and all chemistry ceases. The products are identified by their photoionization (PIMS) mass spectra as well as their matrix infrared absorption spectra. The PIMS experiment uses a reflectron time-of-flight mass spectrometer to analyze the ions resulting from photoionization by 118.2 nm (10.487 eV) photons.[18] In separate experiments, we send a gas mixture of CH_3CHO entrained in an Ar carrier gas through the μtubular reactor and the resultant molecular beam impinges on a CsI window cooled to 20 K. The matrix frozen onto the CsI window is subsequently analyzed by IR absorption spectroscopy.[19] Additional experiments were carried out at the chemical dynamics beamline (9.0.2) at the LBNL Advanced Light Source (ALS),[20-21]

where PIMS spectra can be obtained as a function of photon energy, which also allows for the recording of photoionization efficiency (PIE) profiles. Figure 5.1 shows the experimental set-up used for the acetaldehyde experiments.

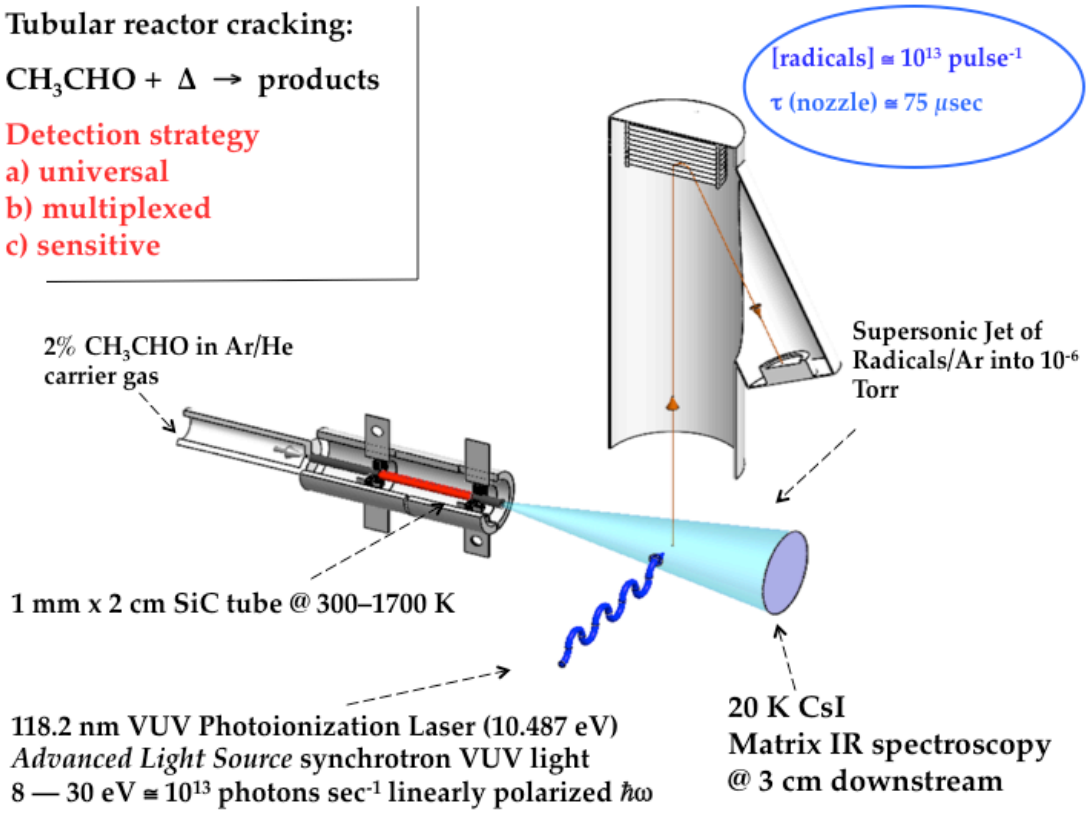

Figure 5.1 Experimental set-up used for acetaldehyde experiments in Boulder and ALS.

5.3 Results

Figure 5.2 shows the PIMS that result from heating CH_3CHO. A 0.3% mixture of acetaldehyde in 2 atm He is expanded through the μtubular reactor at temperatures of 300 K, 975 K, 1375 K, and 1575 K. The scan at room temperature only shows a signal for m/z 44 corresponding[25] to CH_3CHO^+. At higher temperatures, the ions at m/z 15 and 42 are assigned[26,27] to CH_3^+ and $CH_2{=}C{=}O^+$.

The feature at m/z 43 results from dissociative ionization of thermally excited acetaldehyde, $CH_3CHO^* + hw_{118.2nm} \rightarrow (CH_3CHO^*)^+ \rightarrow H + CH_3CO^+$ m/z 43. We can demonstrate this by examining the photoionization efficiency (PIE) curve for acetaldehyde measured at the ALS with its tunable light source. The right panel of Figure 5.3 shows the PIE(CH_3CHO) as it is heated in the μtubular reactor; the mass spectrometer records the appearance of m/z 44 as a function of photon energy. Photoionization of CH_3CHO removes a non-bonding electron from the O=C< group and is a vertical process. This can be seen in the photoelectron spectrum.[28] Consequently the threshold for appearance of m/z 44 remain constant. In contrast, the threshold for observation of the m/z 43 peak at 1175 K was found to be as low as 10.0 eV. Consequently, given both experimental estimates of the room temperature threshold, and the $[CH_3CO\text{-}H]^+$ bond energy that we have calculated to be about 0.6 - 0.7 eV (which implies a 0 K threshold for $CH_3CHO \rightarrow CH_3CO^+ + H$ of about 10.8 - 10.9 eV), this suggests a substantial amount of vibrational excitation (of order 0.7 eV) in the 1175 K acetaldehyde. This large amount of excitation appears to be inconsistent with preliminary studies of heated acetaldehyde vibrational states *via* chirped-pulse mm microwave spectroscopy[29] [Kirill Kuyanov-Prozument and R. W. Field, unpublished results, 2011]. An alternative explanation,

which cannot be excluded at this point, is that the m/z = 43 signal arises from dissociative ionization of vinyl alcohol[30] (CH_2=CH-OH), because $IE(CH_2CHOH) \leq 9.33 \pm 0.05$ eV. The vinyl alcohol is predicted[31] to dissociatively ionize: $CH_2CHOH + \ell_{VUV} \rightarrow CH_2CHOH^+ \rightarrow H + CH_3CO^+$, m/z 43.

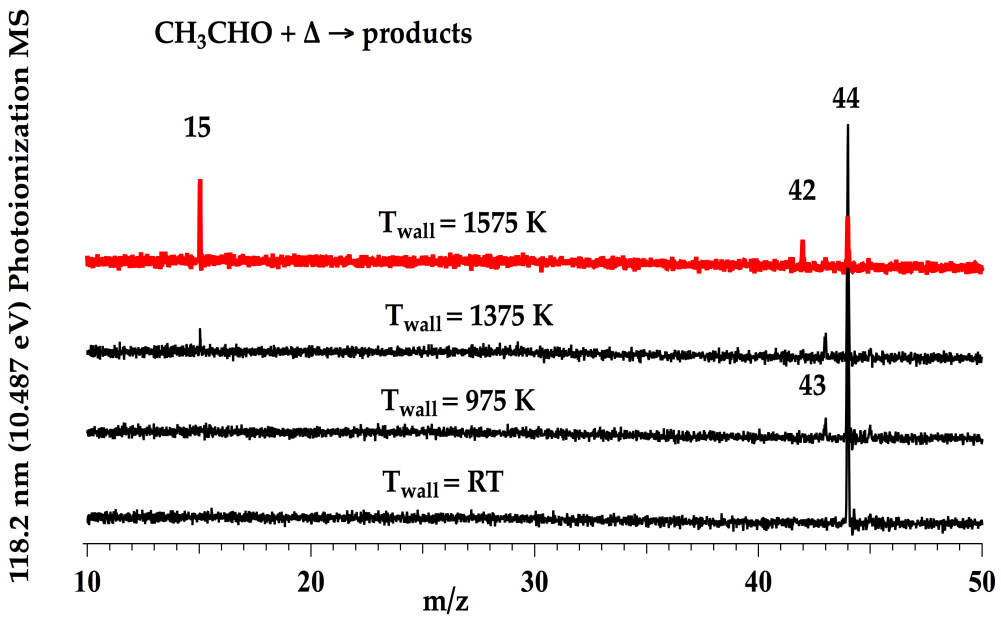

Figure 5.2 Photoionization mass spectra of the thermal cracking products of acetaldehyde are shown. The fixed-frequency PIMS uses the 9th harmonic of a YAG laser, 118.2 nm or 10.487 eV, for photoionization. Typical samples have 0.3% acetaldehyde mixed with 2 atm He. There are 4 different spectra in this figure. Bottom Trace: CH_3CHO traversing the μtubular reactor at room temperature; 2nd Trace is CH_3CHO heated to 975 K by the μtubular reactor: 3rd Trace is CH_3CHO heated to 1375 K in the μtubular reactor, 4th Trace (red) is CH_3CHO t raversing the μtubular reactor heated to 1575 K.

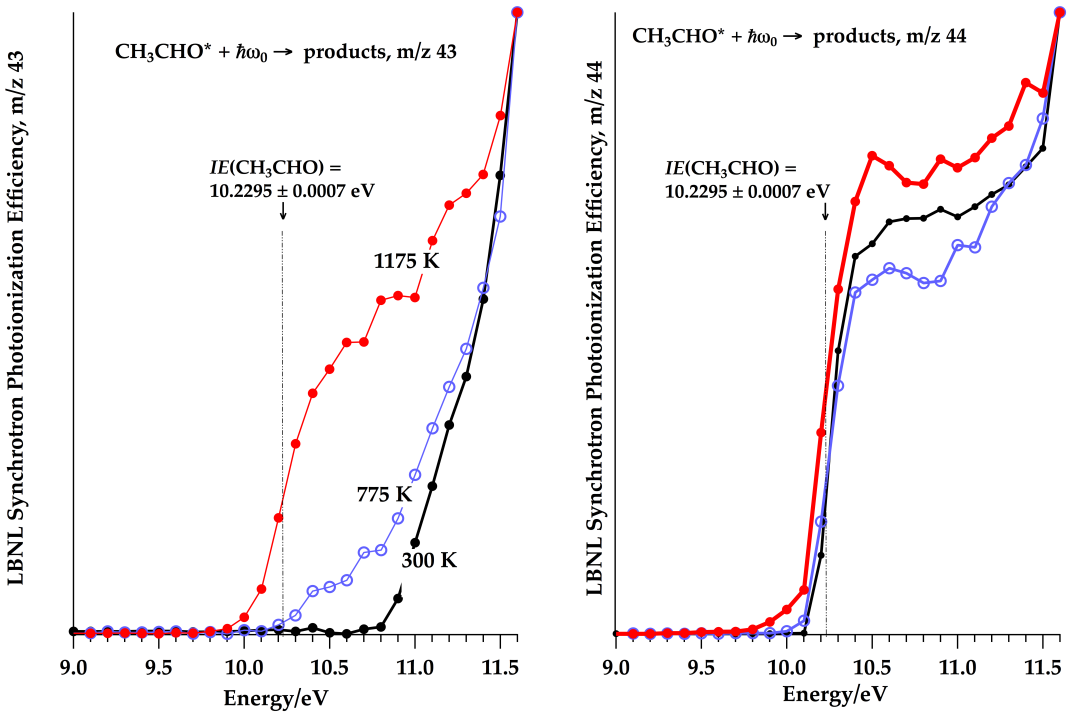

Figure 5.3 The photoionization efficiency (PIE) curves from the LBNL's Advanced Light Source that result from heating CH_3CHO. The three spectra in the right hand panel show the appearance of m/z 44 when samples of CH_3CHO are passed through the SiC tube at 300 K, 775 K, and 1175 K. The ionization energy of acetaldehyde is known[25] to be $10.229_5 \pm 0.0007$ eV. The panel on the left side shows the appearance of m/z 43 when CH_3CHO is heated by the μtubular reactor to 300 K, 775 K, and 1175 K.

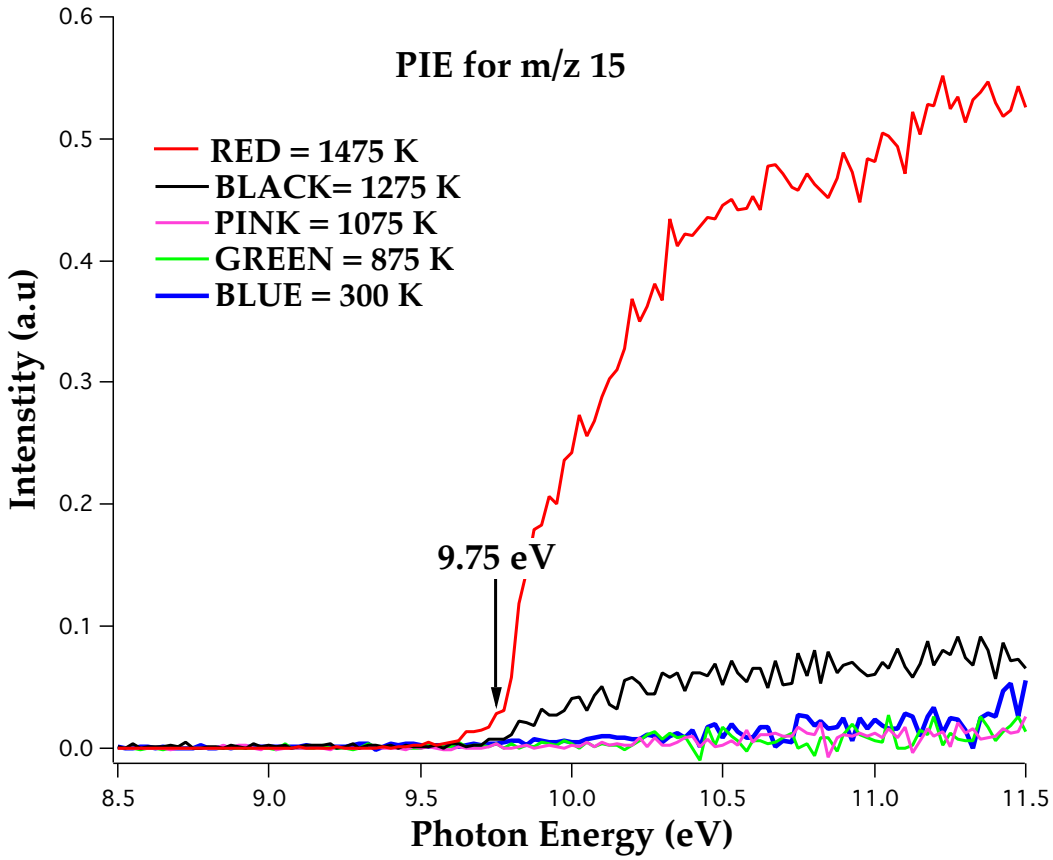

Figure 5.4 PIE curve confirming that 15 m/z is in fact methyl radical from Figure 5.2

When d1-acetaldehyde, m/z 45, flows though the μtubular reactor, the observed PIMS are shown in Figure 5.5A and B. Heating the SiC tube to 1275 K leads to the appearance of ions at m/z 15, 16, 42, 43, and 44. The species at m/z 43 is CH_3CO^+ resulting from dissociative ionization and the feature at m/z 42 is assigned to $CH_2{=}C{=}O^+$. From eq. (5.2), we expect to observe CH_3 radicals from CH_3CDO. Heating the μtubular reactor up to 1475 K shows a set of peaks at m/z 15, 16, and 17. PIE scans of these ions confirm their identity[26] as methyl radicals: CH_3, CH_2D, and CHD_2.

The thermal decomposition of CD_3CHO (m/z 47) is shown in Figure 5.6.A and B. The d3-acetaldehyde sample is contaminated by CD_2HCHO (6%) and gives signals at m/z 46. Dissociative ionization also produces CD_3CO^+ at m/z 46. Heating the sample to 1275 K leads to the appearance of signals for $CD_2{=}C{=}O^+$ (m/z 44) and CD_3^+ (m/z 18). Raising the SiC temperature to 1475 K leads to the appearance of isotopically substituted methyl radicals. Figure 5.6B shows this more clearly at a SiC temperature of 1675 K; PIE scans confirm[26] the presence of CD_3, CD_2H, CHD_2, and CH_3 radicals.

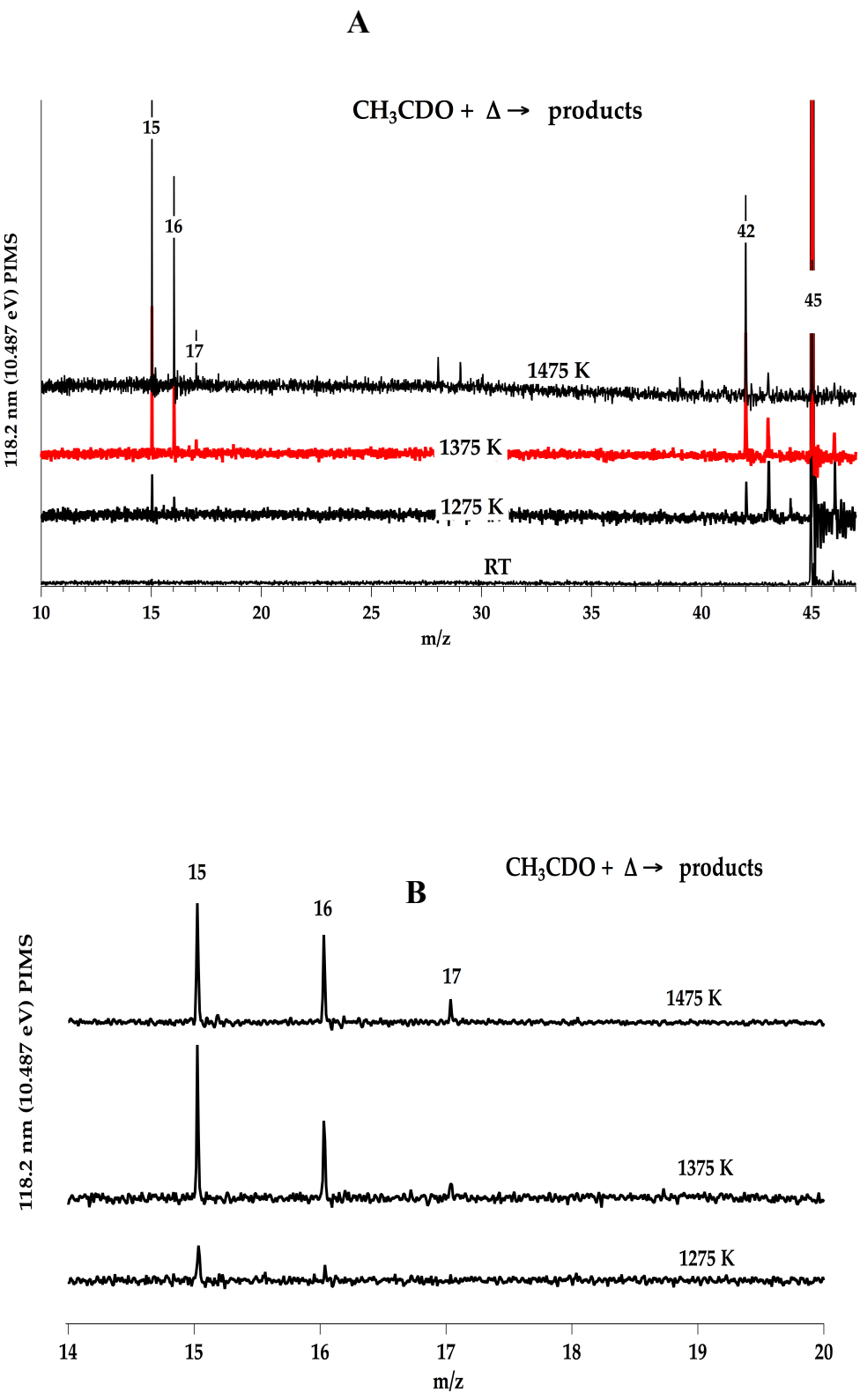

Figure 5.5 A) PIMS of CH_3CDO showing the presence of CH_3, CH_2D, CHD_2, and $CH_2{=}C{=}O$. Dissociative ionization at m/z 43. m/z 44 from CH_3CHO impurity. B) PIMS of methyl region of CH_3CDO

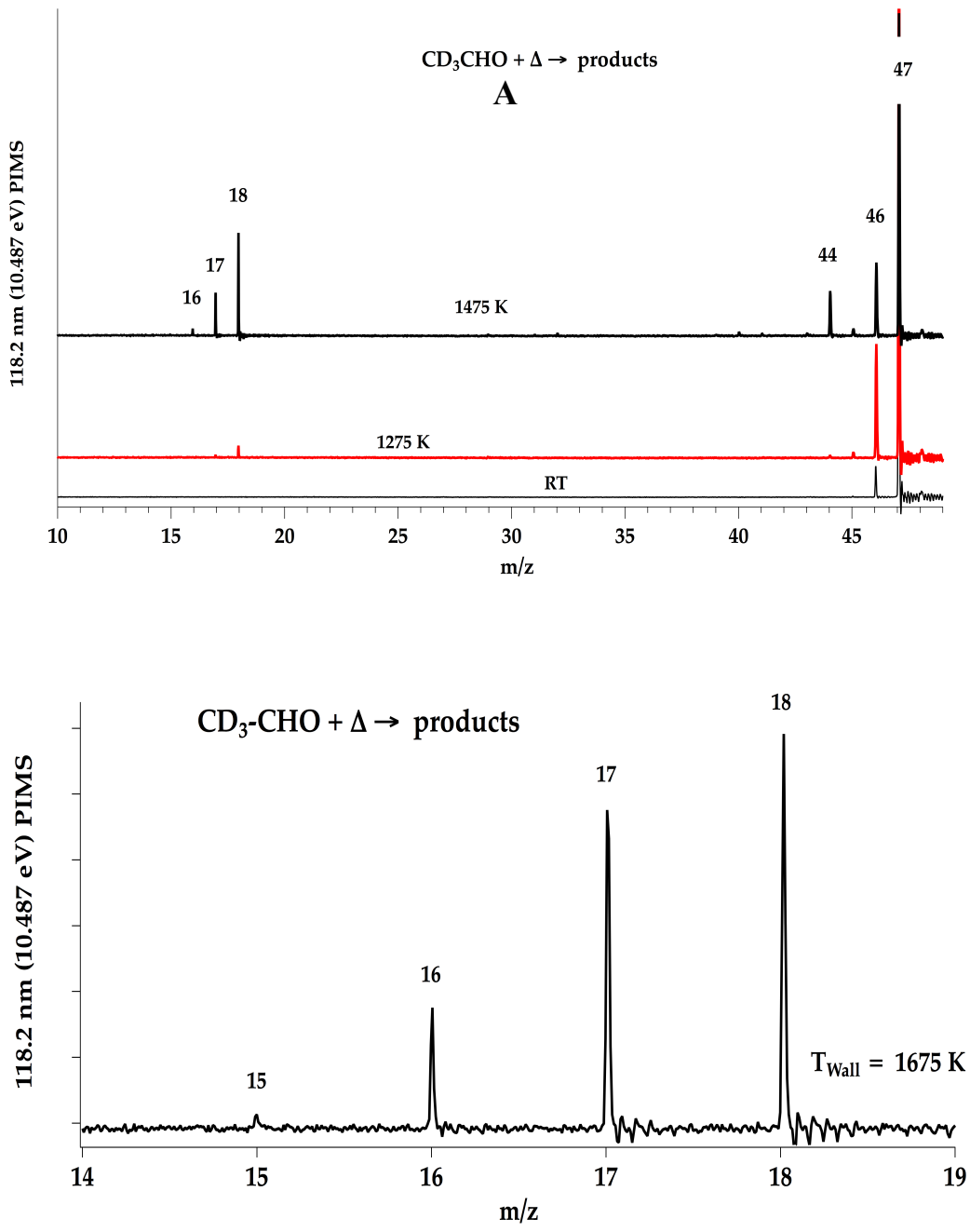

Figure 5.6 A) PIMS of CD_3CHO showing the presence of CD_3, CD_2H, CDH_2, CH_3 and CHD=C=O. Dissociative ionization at m/z 46. CD_2HCHO impurity at m/z 46 and dissociative ionization at m/z 45. B) PIMS methyl region of CD_3CHO

Figure 5.7 shows the PIMS spectra of CD_3CDO heated to 1575 K. Peaks for the parent cation, m/z 48, and that for dissociative ionization, m/z 46, are detected. The weak band at m/z 47 is assigned as CHD_2CDO^+ and arises from a known contamination of the CD_3CDO sample. The band at m/z 44 is that of $CD_2{=}C{=}O^+$ while that at m/z 18 is CD_3^+.

It is important to note that the commercial samples of CH_3CDO, CD_3CHO and CD_3CDO are produced by equilibrating acetaldehyde with D_2O and base. Proton NMR was taken on all samples to determine the isotopic impurtities present. The proton NMR spectrum of CH_3CDO has a small impurity, 0.5% of CH_3CHO in the sample. The proton NMR spectrum of the CD_3CHO sample shows that 6% is CD_2HCHO arising from incomplete proton/deuteron exchange and 1% impurity of CH_2DCHO. This is evident in the 118.2 nm PIMS in Figure 5.6. The black trace for CD_3CHO shows a small feature at m/z 45 which is assigned to CD_2HCO^+ produced by dissociative ionization of CD_2HCHO. The proton NMR spectrum of CD_3CDO reveals CD_2HCDO and CH_3CDO as present impurties.

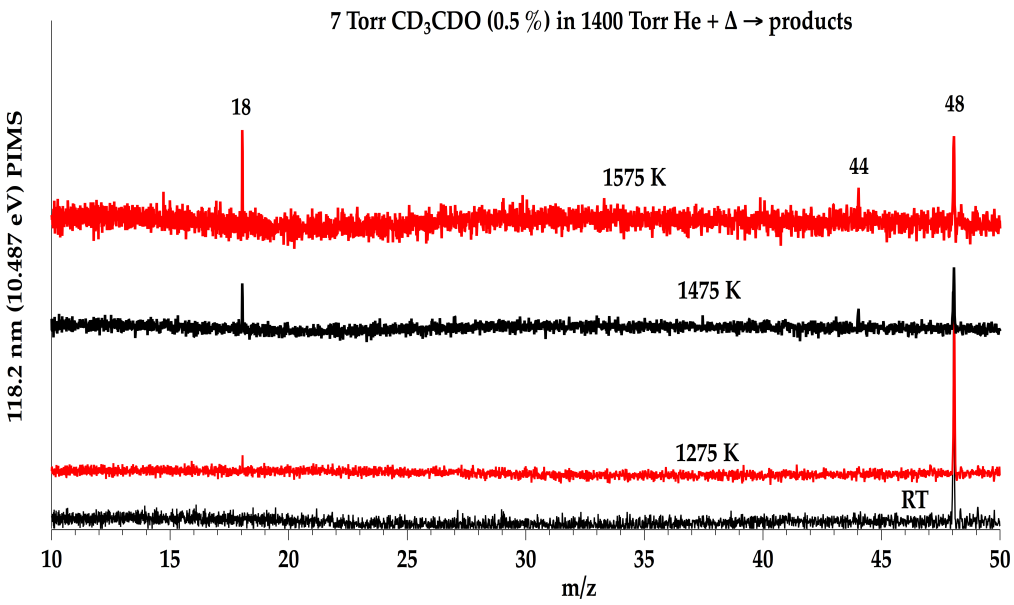

Figure 5.7 PIMS spectra of CD_3CDO showing the presence of CD_3 at m/z 18 and CD_2=C=O at m/z 44.

To corroborate the acetaldehyde PIMS spectra, we used matrix IR spectroscopy. We have observed IR signals from CO as well as CH_2=C=O and CD_2=C=O which further confirm the PIMS assignments at m/z 42 and 44. The VUV laser in Figure 5.1 operates at 118.2 nm (10.487 eV) and cannot[32] ionize CO. But there is no doubt that the thermal cracking of CH_3CHO forms CO.

Figure 5.8 is a matrix IR spectrum and shows the surprising result that heating CH_3CHO to 1675 K leads to the production of acetylene. The green trace is a background scan of Ar heated to 1675 K and the thin black line is a background scan of a 0.3% mixture of CH_3CHO/Ar mixture at 300 K. The vibrational spectra of acetaldehyde has been studied earlier.[33-35] We observe strong IR signals[33] from HC≡CH when CH_3CHO is heated to 1500 K and heating CD_3CDO produces DC≡CD. Pyrolysis of CH_3CDO generates both HC≡CH and HC≡CD while the thermal cracking of CD_3CHO produces a mixture of HC≡CD and DC≡CD. Of course the PIMS in Figure 5.1 cannot detect acetylene because the ionization energy[32] is too high for our VUV source at 10.487 eV. Matrix IR spectra (Figure 5.9) also reveal that heating CH_3CHO to 1000 K triggers a keto-enol isomerization: $CH_3CHO \rightarrow CH_2$=CH-OH. We observe strong IR bands from CH_2=CHOH in an argon matrix that clearly identify the enol. We observe the ν_{OH}, $\nu_{C=C}$, and ν_{CH2} bands of vinyl alcohol.[36] The bands observed for vinyl alcohol match those reported in an argon matrix[37] and the single gas-phase value[38] found for ν_{13}. A PIE of CH_3CHO in Figure 5.10 confirms the formation of vinyl alcohol. Heating CH_3CHO to 1275 K triggers a large shift in the ionization threshold, which is consistent[30] with the known ionization energy of CH_2=CHOH.

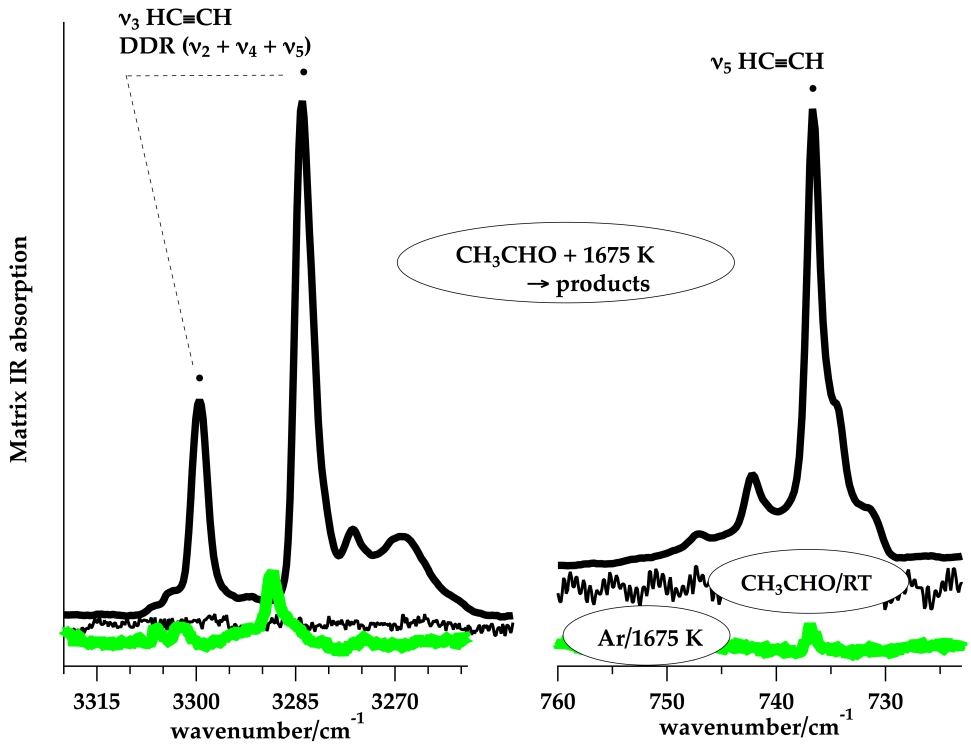

Figure 5.8 Matrix IR absorption spectrum demonstrating the presence of acetylene resulting from the thermal cracking of CH_3CHO at 1675 K. The green trace indicates background absorption of the buffer gas, Ar, heated to 1675 K; the narrow black spectrum is a CH_3CHO at room temperature (1 Torr CH_3CHO in 1.3 atm Ar or a 0.1% mixture); and the thick black spectrum results from heating CH_3CHO to 1675 K. The two IR active vibrational modes[33] of HC≡CH are assigned.

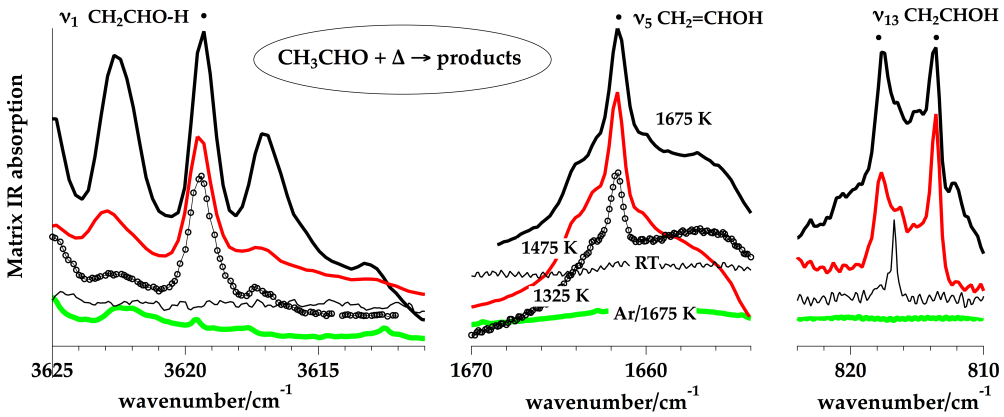

Figure 5.9 Matrix IR absorption spectra demonstrating the presence of vinyl alcohol (CH_2=CH-OH) following the pyrolysis of acetaldehyde. The green trace indicates background absorption of the buffer gas, Ar, heated to 1675 K; the narrow black spectrum is CH_3CHO at room temperature; the knotted trace (- °-°-°-) results from heating to 1325 K, the red scan is 1475 K; and the thick black spectrum results from heating CH_3CHO to 1675 K. Three vibrational fundamentals for vinyl alcohol are assigned: the O-H stretch at $\nu_1(CH_2CHO\text{-}H)$ = 3619 cm^{-1}, the >C=C< stretch at $\nu_5(CH_2{=}CHOH)$ = 1662 cm^{-1}, and the H_2CCHOH out-of-plane deformation at $\nu_{13}(CH_2CHOH)$ = 814 and 818 cm^{-1}. The 817 cm^{-1} band in the CH_3CHO room temperature spectrum is an un-assigned impurity.

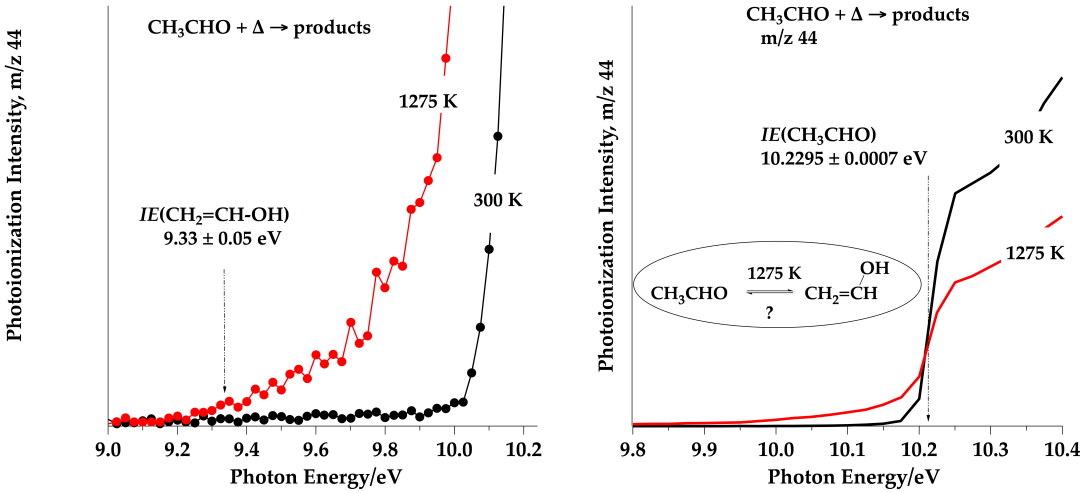

Figure 5.10 Expanded scan of the photoionization origin; the PIE(m/z 43) intensity scales are comparable. Intensity scale of the 300 K scan is (0.0 – 0.5) while that of the 1275 K trace is (0.0 – 0.3). The PIE scan resulting from heating CH_3CHO at 1275 K reveals a threshold consistent with that observed[30] for vinyl alcohol, $IE(CH_2{=}CHOH)$ = 9.33 ± 0.05 eV.

Figure 5.11 is a composite spectrum of the IR bands that are detected when acetaldehyde is cracked at 1675 K. It is observed that heating CH_3CHO produces only[39] CH_2CHO-H and CH_3CDO generates CH_2CDO-H. Decomposition of CD_3CHO forms CD_2CHO-D while CD_2CDO-D is the product from CD_3CDO.

From the IR spectra of the acetylenes and the nature of the vinyl alcohols in Figure 5.11, we have been able to correlate the two. We find:

$$CH_3CHO \rightarrow CH_2{=}CH\text{-}OH \rightarrow HC{\equiv}CH \qquad \textbf{(5.13)}$$

$$CH_3CDO \rightarrow CH_2{=}CD\text{-}OH \rightarrow HC{\equiv}CH + HC{\equiv}CD \qquad \textbf{(5.14)}$$

$$CD_3CHO \rightarrow CD_2{=}CH\text{-}OD \rightarrow HC{\equiv}CD + DC{\equiv}CD \qquad \textbf{(5.15)}$$

$$CD_3CDO \rightarrow CD_2{=}CD\text{-}OD \rightarrow DC{\equiv}CH \qquad \textbf{(5.16)}$$

We interpret the acetylene isotope distributions as resulting from two competing pathways. The vinyl alcohol can undergo a (1, 2) elimination to make acetylene + water or it could undergo a (1, 1) elimination to produce water + the diradical (CH_2=C**:**), vinylidene, which rearranges to acetylene.

Vinylidene is one of the most fundamental carbenes and its properties and the [CH_2=C**:** → HC≡CH] isomerization dynamics have been the subject of many investigations.[40-47] Several previous workers[12,48,49] had suspected the importance of vinyl alcohol in acetaldehyde decomposition. There are few predictions[50,51] of the role of HC≡CH and, especially, CH_2=C**:** in the decomposition of acetaldehyde. Besides vinylidene, we also considered the possibility that

the methylhydroxycarbene,[52] CH_3-C-OH, might be a participant in the thermal decomposition of CH_3CHO; however we believe that this is unlikely.[53]

The matrix IR spectra reveal the decomposition pathways (5.13) — (5.16) and predict that the isotopes of the product water will be correlated with the isotopomers of acetylene:

$$CH_3CDO \rightarrow CH_2{=}CD\text{-}OH \rightarrow H_2O + HC{\equiv}CD \text{ or } [HOD + CH_2{=}C{:}] \rightarrow HOD + HC{\equiv}CH \quad \textbf{(5.17)}$$

$$CD_3CHO \rightarrow CD_2{=}CH\text{-}OD \rightarrow D_2O + HC{\equiv}CD \text{ or } [HOD + CD_2{=}C{:}] \rightarrow HOD + DC{\equiv}CD \quad \textbf{(5.18)}$$

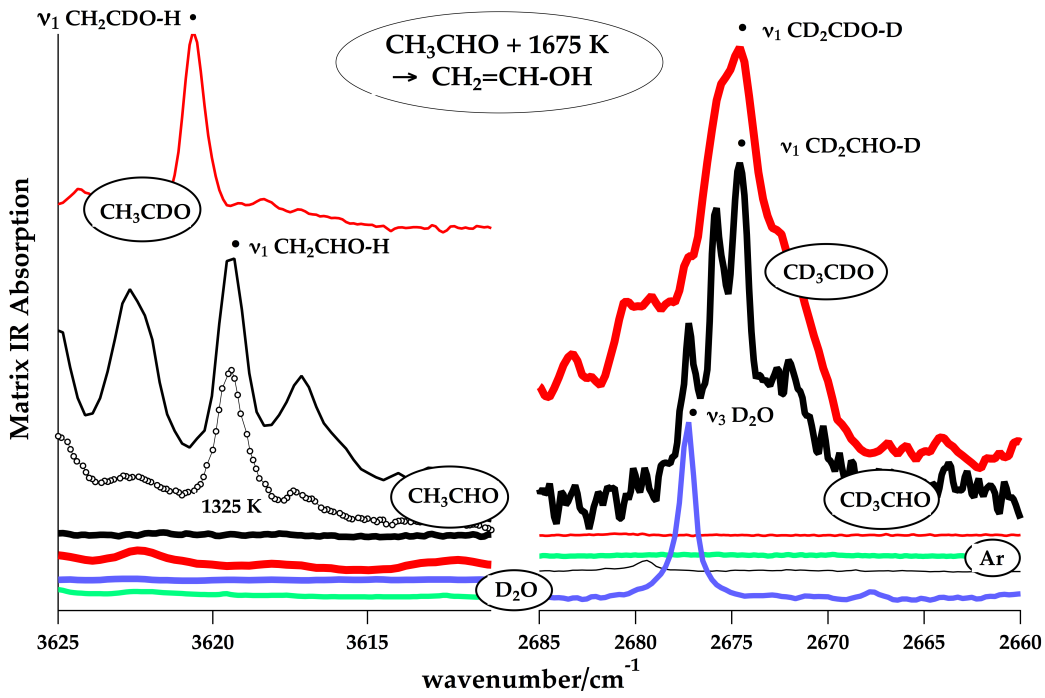

Figure 5.11 Matrix IR absorption spectra tracking the shifts of ν_{OH} or n_{OD} of four vinyl alcohols that result when acetaldehyde is heated to 1675 K in the μtubular reactor. The green trace is that of the carrier gas, Ar, heated to 1675 K while the purple trace is that of D_2O at room temperature. In the left panel is shown that heating CH_3CHO to 1675 K (narrow black spectrum) produces CH_2=CHOH while CH_3CDO (narrow red scan) yields CH_2=CDOH at 1675 K. The assignments for both $n_1(CH_2CHO\text{-}H)$ = 3620 cm^{-1} and $\nu_1(CH_2CDO\text{-}H)$ = 3621 cm^{-1} are marked (•). In the right panel of are the spectra of CD_2=CHOD (thick black) resulting from pyrolyzing CD_3CHO at 1675 K and CD_2=CDOD (thick red) arising from heating CD_3CDO at 1675 K. The assignments for both $\nu_1(CD_2CHO\text{-}D)$ = 2675 cm^{-1} and $\nu_1(CD_2CDO\text{-}D)$ = 2675 cm^{-1} are marked (•). In the left panel it is demonstrated that heating CH_3CHO (the knotted trace -°-°-°-) to 1325 K shows the first appearance of $\nu_1(CH_2CHO\text{-}H)$.

The PIMS in Figure 5.12 is consistent with eq. (5.17) and confirms that the decomposition of CH_3CDO produces H_2O + HOD + HC≡CH + HC≡CD. The red trace in Figure 5.12 is the observed PIMS of CH_3CDO expanded through the μtubular reactor at 300 K. The molecular beam of the products of the SiC tube are irradiated with VUV light from the ALS synchrotron at hw_0 = 12.675 eV. Because[25] *IE*(CH_3CHO) is 10.229_5 ± 0.0007 eV, the d_1-acetaldehyde dissociatively ionizes to produce ethylene, m/z 28. An examination of the PIE curve of m/z 28 in Figure 5.12 confirms[54] that it is due to ethylene. Figure 5.12 demonstrates that heating CH_3CDO to 1675 K leads to the production of ions at m/z 18 (H_2O), 19 (HOD), 26 (HC≡CH) and 27 (DC≡CH). The PIE curves in Figure 5.13 absolutely confirm[32] m/z 18 as H_2O, m/z 19 as HOD, m/z 26 as HC≡CH, and m/z 27 as HC≡CD in Figure 5.12. The case for CD_3CHO, eq. (5.18), has also been confirmed.[1]

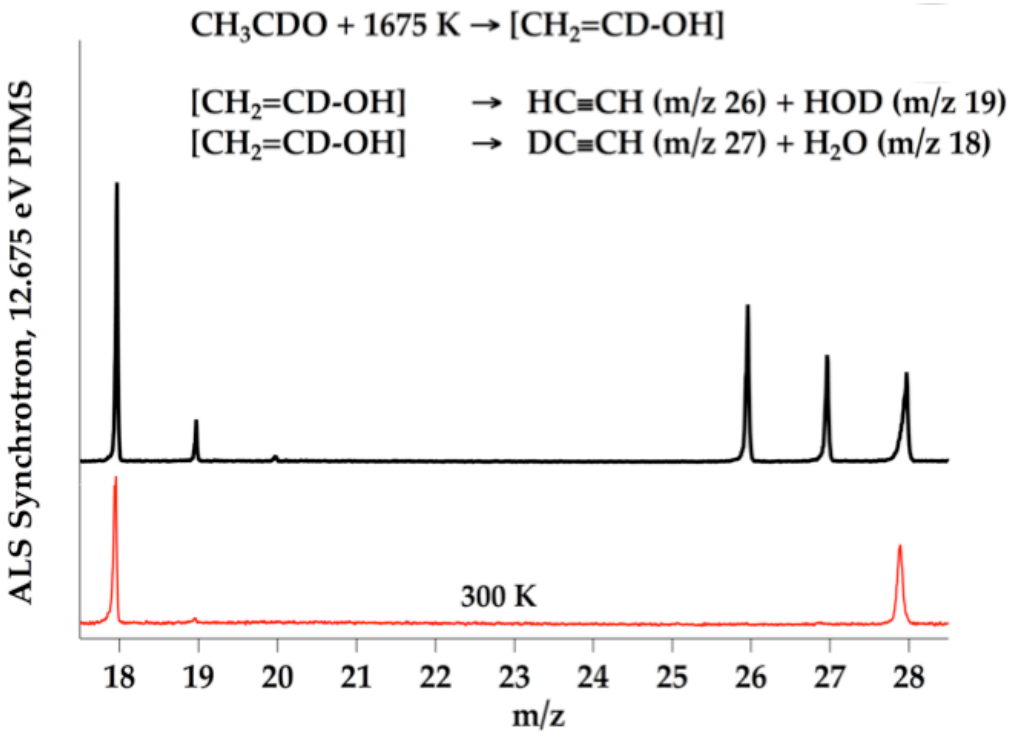

Figure 5.12 PIMS spectra that confirms that the decomposition of CH_3CDO produces H_2O + HOD + HC≡CH + HC≡CD. The red trace is the observed PIMS of CH_3C DO expanded through the μtubular reactor at 300 K. The molecular beam of the products of the SiC tube are irradiated with VUV light from the ALS synchrotron at $\hbar\omega_0$ = 12.675 eV. Because[11] *IE*(CH_3CHO) is $10.229_5 \pm 0.0007$ eV, the d_1-acetaldehyde dissociatively ionizes to produce ethylene, m/z 28. An examination of the PIE curve of m/z 28 confirms that it is due to ethylene. Heating CH_3CDO to 1675 K leads to the production of ions at m/z 18 (H_2O), 19 (HOD), 26 (HC≡CH) and 27 (DC≡CH).

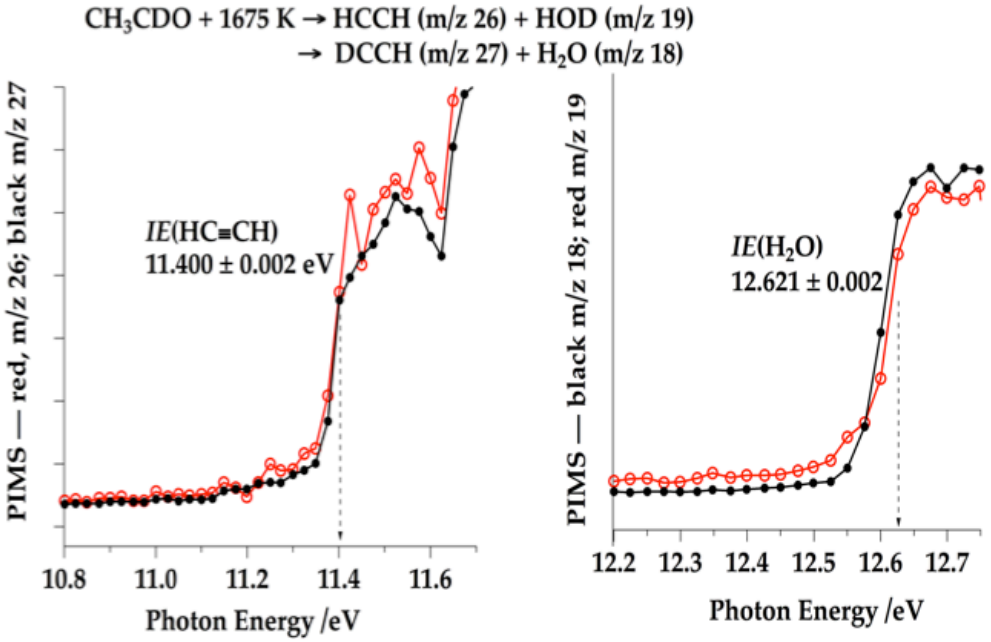

Figure 5.13 The PIE curves of HCCH (left panel) and H_2O (right panel) absolutely confirm m/z 18 as H_2O, m/z 19 as HOD, m/z 26 as HC≡CH, and m/z 27 as HC≡CD in Figure 5.12.

Figure 5.14 shows the PIMS resulting from cracking CD_3CHO at 1375 K when the synchrotron at the Berkeley Advanced Light Source is used to photoionize the pyrolysis products. In Figure 5.14, $\hbar\omega_{VUV}$ is set to 12.9 eV, which is sufficient to ionize acetylene, methane, and water.[22] The features at m/z 19 and 20 are identified by the associated PIE curves as HOD^+ and D_2O^+ as are the peaks at m/z 26, 27, and 28 to $HCCH^+$, $DCCH^+$, and $DCCD^+$. The tiny $HCCH^+$ signal is an artifact arising from the aforementioned impurity in the CD_3CHO sample.

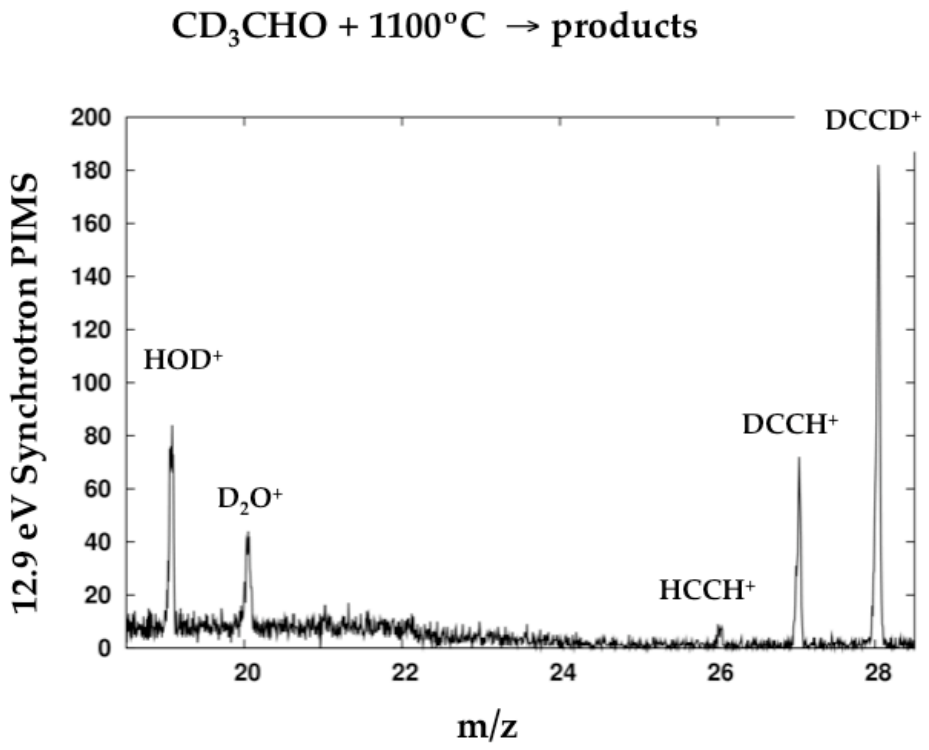

Figure 5.14 The PIMS resulting from cracking CD_3CHO at 1100ºC when the synchrotron at the LBNL's Advanced Light Source is used to photoionize the pyrolysis products. The light source is set to 12.9 eV in order to ionize methane, acetylene and water. Samples of d_3-acetaldehyde entrained in Ar buffer gas are subjected to pyrolysis by a 1 mm x 2 cm SiC tube heated to 1100 ºC. Typical samples have 1 % acetaldehyde mixed with 1 atm Ar. The approximate pressure in the μtubular reactor is 75 Torr and the centerline temperature is within 100 – 200 ºC of the wall temperature. The transit time through the heated SiC tube is roughly 50 — 100 μsec.

5.4 Discussion and Conclusions

A goal of this study is to identify the homogeneous, gas phase products of (5.1). Heat from the SiC walls of the μtubular reactor drives the thermal dissociation in the μtubular reactor. The CH_3CHO is entrained in 1 atm of He or Ar buffer gases as a 0.1% mixture. Collisions of the gases with the hot walls thermally excite the organics and decompose them. The PIMS and IR spectra have identified CH_3, CO, $CH_2{=}C{=}O$, and $HC{\equiv}CH$ as pyrolysis products of CH_3CHO. It is an important concern that some of the thermal dissociations might be catalyzed by heterogeneous processes at the hot walls.

In particular we have seen in Figures 5.5 and 5.6 that the CH_3 and CD_3 radicals are isotopically scrambled to CH_2D and CHD_2. We believe that this scrambling is the result of homogeneous, bimolecular reactions[55] between methyl radicals and hydrogen atoms. Thermal dissociation of CH_3CDO produces equal amounts of CH_3 and D atoms in the μtubular reactor; likewise CD_3CHO will crack to generate identical amounts of CD_3 radicals and H atoms. Therefore the radical/radical reactions are expected.

$$CH_3 + D + M \rightleftharpoons [CH_3D]^* + M \rightleftharpoons CH_2D + H \qquad \textbf{(5.23)}$$

However there is a possibility of radical reactions at the walls of the SiC tube. The isotope exchange could be triggered by methyl radicals with impurities (“dirt”) at the carborundum (SiC) wall as shown with CD_3 in Scheme 1. Because of the high bond energy of methane (see reaction 19 in Table 5.1), H atom abstraction reactions by methyl radicals will be exothermic.

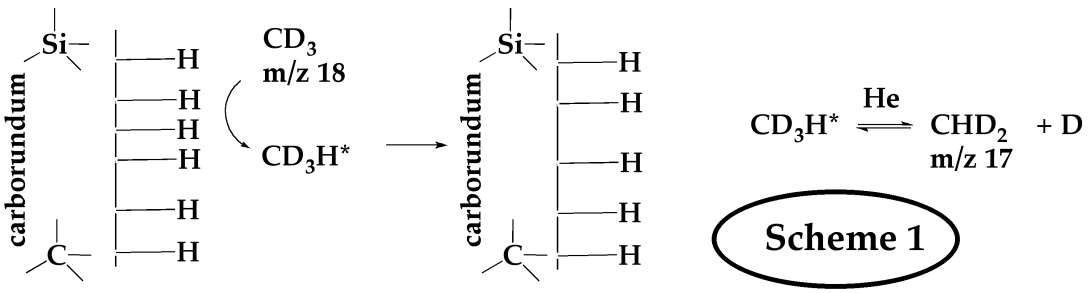

The resulting CD_3H^* will be chemically activated and will not survive the collisions with the hot He buffer gas in the μtubular reactor. Such wall reactions could account for the sequence of products observed in Figure 5.6, m/z 18 → m/z 17 → m/z 16 → m/z 15. But Figure 5.7 shows that the CD_3 radicals (from CD_3CDO pyrolysis) do not scramble isotopes. We expect that wall reactions of impurities shown in Scheme 1 would produce CHD_2 radicals but this is not observed. A lack of isotope scrambling of CD_3 radicals was observed earlier.[56] In this study, $CD_3OC_6D_5$ was pyrolyzed to $CD_3 + OC_6D_5$ radicals.

Besides the chemistry in Scheme 1, one could imagine that the hot SiC walls could act like Lewis acid catalysts. It would be expected[57] that the keto-enol tautermerization of acetaldehyde, $CH_3CHO \rightleftharpoons CH_2$=CH-OH, would be catalyzed by a suitable Lewis acid catalyst such as $AlCl_3$ or Al_2O_3 or BF_3; such a process is sketched in Scheme 2 using boron as a Lewis acid.

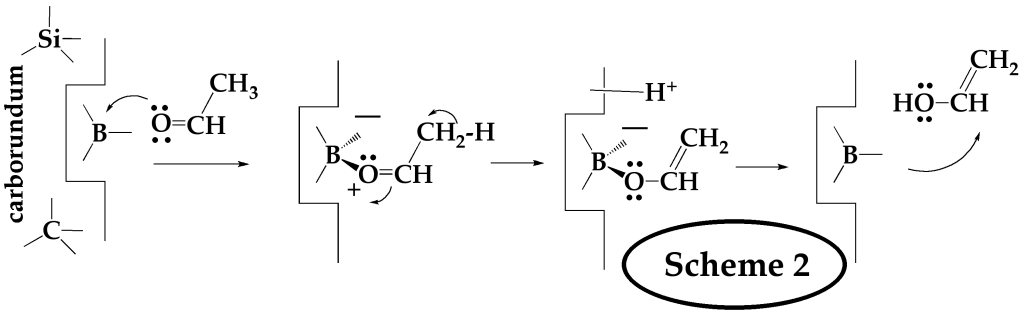

Besides isomerization of the aldehyde, perhaps heterogeneous reactions on the hot SiC

walls catalyze the elimination of water from acetaldehyde to make acetylenes. *E1* elimination reactions of alcohols are well established.[57] Scheme 3 suggests a possible route for the formation of alkynes from vinyl alcohols.

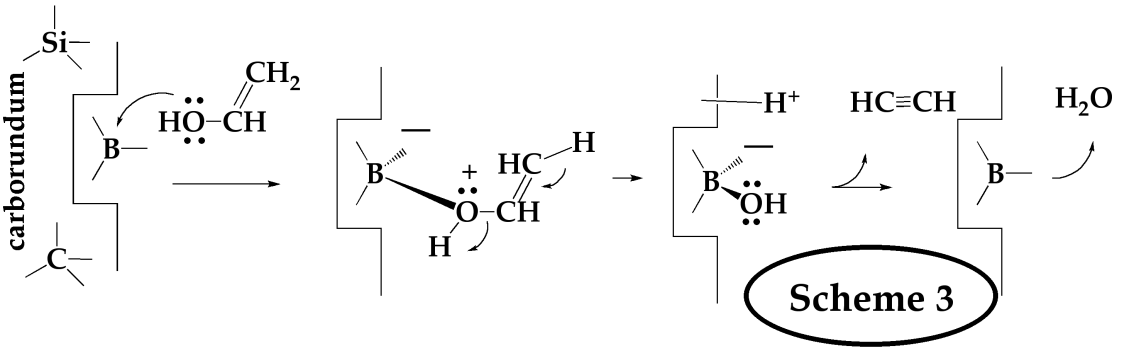

Scheme 3

The μtubular reactors that have been used to thermally crack acetaldehyde are 1 mm x 2 cm SiC tubes. Silicon carbide (SiC), commonly referred to as carborundum, is a tetrahedrally bonded polymer of silicon and carbon.[58] The C—Si distance is 1.89 Å while the Si—Si distance is 3.08 Å. Silicon carbide powder has been mass-produced since the 19th century for use as an abrasive and cutting material. Grains of silicon carbide can be bonded together by sintering to produce very hard ceramics. Silicon carbide is highly inert chemically and does not melt at any known pressure. The high sublimation temperature of SiC (approximately 3000 K) makes it useful for furnace components and bearings. Silicon carbide exists in approximately 250 crystalline forms. These different forms are variations of the same chemical compound that are identical in two dimensions and differ in the third which are layers stacked in a certain sequence.

The tubes of SiC that are used for the μtubular reactors are commercial products commonly used for space-heaters. The SiC is not pure and boron, nitrogen and aluminium are common impurities[59] of carborundum. Strikingly, boron is almost 0.7% of the SiC tube but its "chemical state" is not known. The other prominent impurity is carbon at roughly 0.5% of the

sample. Perhaps the B and C impurities are combined as boron carbide. Boron carbide (chemical formula approximately B_4C) is an extremely hard boron-carbon ceramic material used in tank armor and numerous industrial applications. It is one of the hardest materials known, behind cubic boron nitride and diamond. Boron carbide has a complex crystal structure typical of icosahedron-based borides. The structure is layered: the B_{12} icosahedra and bridging carbons form a network plane that spreads parallel to the *c*-plane and stacks along the *c*-axis. The lattice has two basic structure units – the B_{12} icosahedron and the B_6 octahedron. Because of the B_{12} structural unit, the chemical formula of "ideal" boron carbide is often written as $B_{12}C_3$, and the carbon deficiency of boron carbide described in terms of a combination of the $B_{12}C_3$ and $B_{12}C_2$ units. The melting point of boron carbide is 2763 °C (3036 K).

There are no experiments that we can devise to rule out all heterogeneous reactions of acetaldehyde with the hot SiC walls. One reliable way to exclude wall reactions would be to study acetaldehyde pyrolysis in a shock tube under comparable conditions (1000 K — 1700 K; 50 — 150 Torr). It is possible to eliminate wall reactions with a shock tube. It should be possible for GC-FID or GC-MS spectrometers to carefully examine the reaction products. The results from CH_3CHO decomposition in μtubular reactors show that $CH_2{=}C{=}O$, CO, and HCCH should be present and could be detected by a GC-MS.

5.4.1 Bimolecular Reactions

We believe that bimolecular radical/radical reactions of CH_3 and H are responsible for the isotope scrambling in Figures 5.5 and 5.6. We have observed radical/radical reactions in earlier studies of $HC{\equiv}C\text{-}CH_2CH_2ONO$ decomposition,[60] and the pyrolysis of furan[61] or anisole.[56] There is no doubt that CH_3CHO pyrolysis generates CH_3 radicals and H atoms; consequently we

must consider the reactions of these radicals with CH_3CHO that are listed in Table 5.1 as entries 14 — 17. The reactions of H atoms with CH_3CHO are expected to be very rapid and will produce the acetyl radical, CH_3CO, and the vinyloxy (or formylmethyl) radical, CH_2CHO. Table 5.1 indicates that both of these radicals are unstable and both will decompose in the hot SiC tube to product radicals.

$$CH_3CO + \Delta \rightarrow CH_3 + CO \quad \textbf{(5.25)}$$

$$CH_2CHO + \Delta \rightarrow CH_2{=}C{=}O + H \quad \textbf{(5.26)}$$

It is impossible for us to rule reaction (5.25) out. In an attempt to search for reaction (5.26), a cross-over experiment by monitoring the product hydrogen molecules is needed. A future experiment is need where we pyrolyze a 50:50 mixture of d_0-acetaldehyde and d_4-acetaldehyde.

$$CH_3CHO + \Delta \rightarrow CH_3 + CO + H \text{ and } CH_2{=}C{=}O + H_2 \quad \textbf{(5.27)}$$

$$CD_3CDO + \Delta \rightarrow CD_3 + CO + D \text{ and } CD_2{=}C{=}O + D_2 \quad \textbf{(5.28)}$$

If the ketene products result from unimolecular, homogeneous processes, we should observe only H_2 and D_2. If there are bimolecular reactions of H and D atoms, we will find HD. A crossover experiment such as (5.27) + (5.28) at the ALS where hydrogen can be photoionized[62-64] could reveal the ratio of $[HD]\,[H_2]^{-1}\,[D_2]^{-1}$. If we detect no HD, then there are no important reactions of hydrogen atoms with acetaldehyde in the μtubular reactor.

The mechanism of the high temperature acetaldehyde decomposition is more complicated than a simple radical chain reaction.[8] Our qualitative picture is:

$$CH_3CHO \rightarrow CH_3 + [HCO] \rightarrow CH_3 + H + CO \quad \textbf{(5.29)}$$

$CH_3CHO \rightarrow [H_2] + CH_2{=}C{=}O$ **(5.30)**

$CH_3CHO \rightarrow CH_2{=}CHOH \rightarrow HC{\equiv}CH + H_2O$ **(5.31)**

We have used PIMS and IR spectroscopy to detect CH_3, CO, $CH_2{=}C{=}O$, $CH_2{=}CHOH$, $HC{\equiv}CH$ and H_2O. Besides these species, we have made a careful search for CH_4 as a decomposition product from CH_3CHO with IR spectroscopy.[65-67] Searches for methane with PIMS and IR spectroscopy were all negative (Figures 5.15 and 5.16).

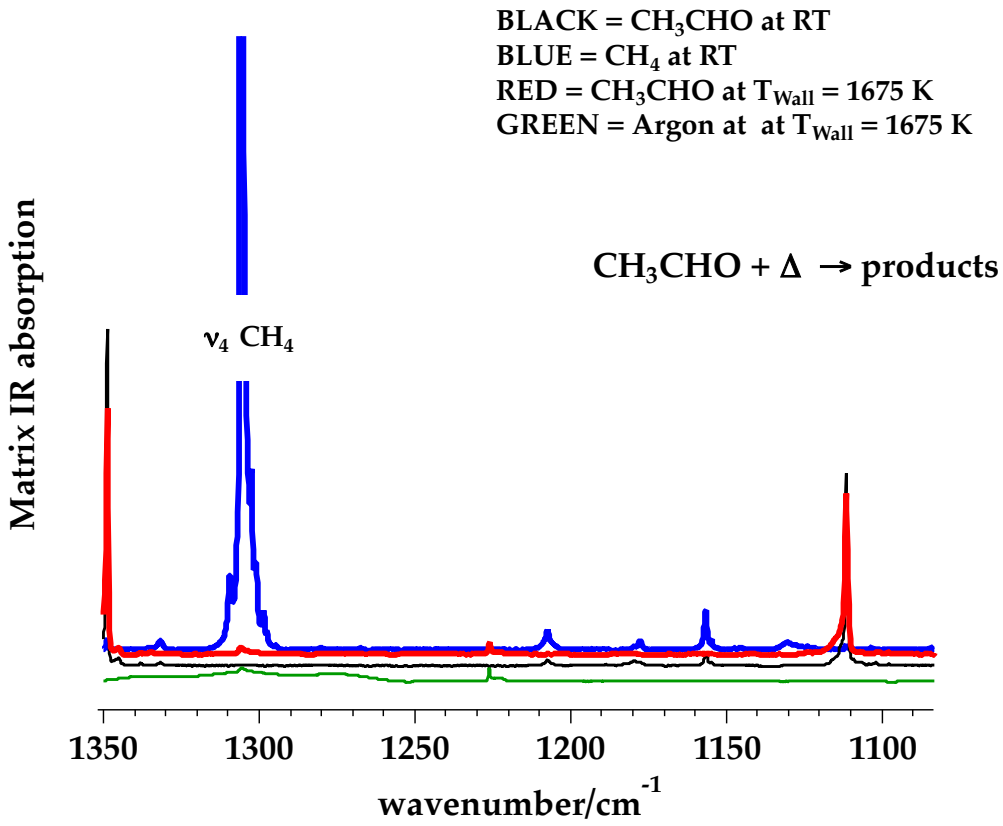

Figure 5.15 IR spectra of CH_3CHO superimposed on pure IR spectrum of methane. This figure shows that no methane is observed from the thermal decomposition of CH_3CHO.

Green = CD_3CDO at RT
Blue = CH_3-N=N-CH_3 at RT
Red = 5 torr CH_3-N=N-CH_3 + 5 torr CD_3CDO at T_{Wall} = 1325 K
Black = CH_3D at RT

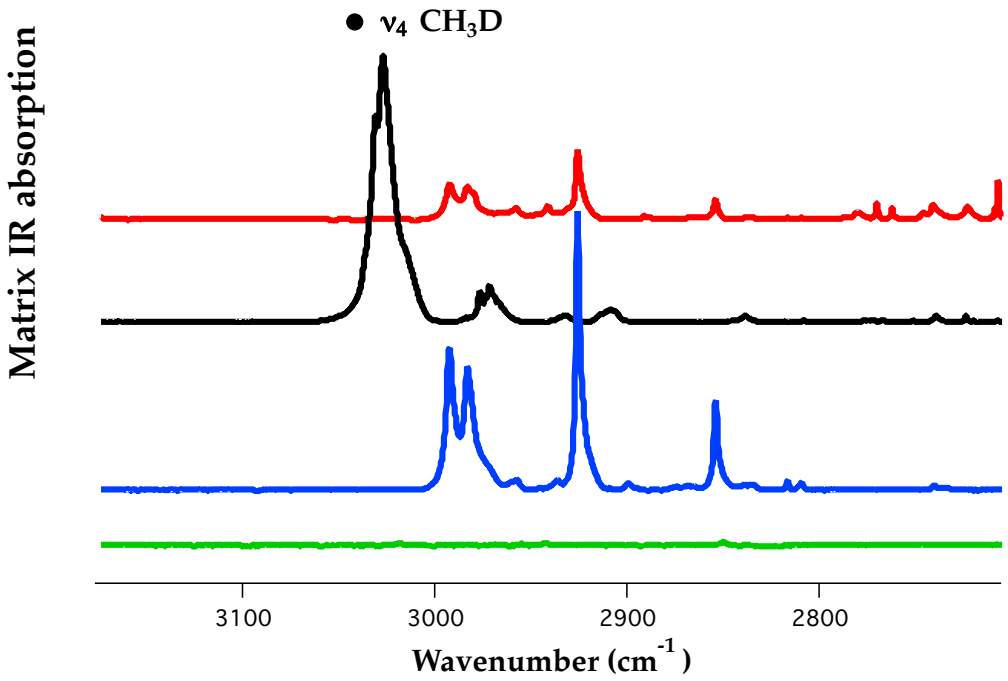

Figure 5.16 IR spectra of CD_3CDO superimposed on pure IR spectrum of CH_3D.This figure shows that no methane is observed from the thermal decomposition of CD_3CDO.

5.4.2 Branching Ratios

One of the advantages of the ALS is that absolute branching ratios for a given decomposition channel can be determined. The PIMS and matrix IR experiments located in Colorado only allow for a qualitative analysis of products. Consider the decomposition pathway of CH_3CDO via elimination:

$$CH_3CDO + \Delta(1675\ K) \rightarrow [CH_2{=}CH\text{-}OD] \rightarrow HC{\equiv}CH + HOD \quad \textbf{(5.32)}$$

The ALS provides the information needed to determine the mole fraction of HCCH and HOD from the thermal decomposition of CH_3CDO. This is accomplished by modifying the methods previously described by Cool and co-workers.[85] The expression for the normalized ion signal or counts (every ion that hits the detector is a count) to a first approximation in the ALS instrument is given by:

$$S_i^+ \propto (D_i\, n_i)\sigma_i(E_i)\Phi_i(E_i) \quad \textbf{(5.33)}$$

The normalized ion signal S_i^+ for a given species i, is related to the incident photon power, $\Phi_i(E_i)$ at a given photon energy. The photon power, $\Phi_i(E_i)$, given in photons sec^{-1} is derived from the photodiode current measured at the terminal end. QE, is the quantum efficiency of the photodiode as given by the company (NIST calibration). The photoionization cross section $\sigma_i(E_i)$ at a given photon energy, if available, is obtained from the literature. The number density of species i in the interaction region is given by n_i. A mass discrimination factor, D_i, is needed to correct for imperfect transmission through the apparatus. The value for D_i is measured at the start of every experimental run, and is a function of the molecular weight of the ion. A complete

derivation of equation of 5.33 can be found in Appendix D. Certain constants have been omitted from equation 5.33, since the final expression is given in ratios and constants will cancel out, thus the use of the proportional sign. Rearranging equation 5.33 for n_i gives:

$$n_i \propto S_i^+ [D_i \sigma_i(E_p)\Phi_i(E_p)]^{-1} \quad \textbf{(5.34)}$$

It is important to have an internal phototionization standard to determine branching ratios. An ideal standard to use is a small amount of Xe, which is an inert, neutral target with no rotational or vibrational structure. Ionization of Xe at 12.12987 ± 0.00001 eV produces a distribution of ions: $^{129}Xe^+$ (26%), $^{131}Xe^+$ (21%),$^{132}Xe^+$ (27%),$^{134}Xe^+$ (10%), and $^{136}Xe^+$ (9%). If a mixture of CH_3CDO and Xe is flowed through the μtubular reactor at room temperature, one could[68] measure a "normalization" factor at different photon energies (E_p).

$$\left(\frac{n_{CH3CDO}}{n_{xe}}\right)_{300K} = \frac{(S_{45}^+)}{(S_{Xe}^+)} \left[\frac{D_{Xe}\sigma_{Xe}(E_p)\phi_{Xe}(E_p)}{D_{45}\,\sigma_{CH3CDO}(E_p)\phi_{CH3CDO}(E_p)}\right] = Carbon/Xe \quad \textbf{(5.35)}$$

From here the fraction of CH_3CDO that has decomposed to produce HCCH from (5.32) and all other thermal decomposition products, can be determined by equation 5.36:

$$\left(\frac{n_{HCCH}}{n_{xe}}\right)_{1675\,K} = \frac{(S_{26}^+)}{(S_{Xe}^+)} \left[\frac{D_{Xe}\sigma_{Xe}(E_p)\phi_{Xe}(E_p)}{D_{26}\,\sigma_{HCCH}(E_p)\phi_{HCCH}(E_p)}\right] \quad \textbf{(5.36)}$$

Unfortunately, the acetaldehyde studies in this work lacked Xe as an internal standard. At this time it is not possible to determine the fraction of CH_3CDO that decomposes to HCCH but a comparison of product ratios can be established with respect to each other. For example in the case of CH_3CDO decomposing to HCCH + HOD (5.32) a ratio can be taken of HCCH to HOD:

$$\left(\frac{n_{HCCH}}{n_{HOD}}\right) = \frac{(S_{26}^{+})}{(S_{19}^{+})} \left[\frac{D_{HCCH}\sigma_{HCCH}(E_p)\phi_{HCCH}(E_p)}{D_{19}\,\sigma_{HOD}(E_p)\phi_{HOD}(E_p)}\right] \quad \textbf{(5.37)}$$

If the values in Table 5.2 are submitted into equation 5.37 then a ratio of HCCH/HOD is found to be 0.73 ± 0.11. This ratio is close to one, which means that for every HCCH molecule produced from CH_3CDO decomposition, a corresponding HOD molecule is also produced. This strongly suggests that acetylene and HOD are in fact formed by the elimination of the intermediate vinyl alcohol.

Table 5.1
Thermochemistry of CH_3CHO

	Bond Energies/kcal mol^{-1}	DH_{298}	D_0
1	$CH_3CHO \rightarrow CH_3 + HCO$	84.8 ± 0.2	83.0 ± 0.2
2	$CH_3CHO \rightarrow CH_3CO + H$	89.3 ± 0.4	87.9 ± 0.4
3	$CH_3CHO \rightarrow CH_2CHO + H$	95.6 ± 0.4	94.3 ± 0.4
4	$HCHO \rightarrow H + HCO$	88.144 ± 0.008	86.713 ± 0.001
5	$HCO \rightarrow H + CO$	15.6 ± 0.1	14.4 ± 0.1
6	$CH_3CO \rightarrow CH_2{=}C{=}O + H$	43.2 ± 0.6	41.5 ± 0.5
7	$CH_3CO \rightarrow CH_3 + CO$	11.1 ± 0.4	9.5 ± 0.4
8	$CH_2CHO \rightarrow CH_2{=}C{=}O + H$	36.9 ± 0.5	35.1 ± 0.4
9	$CH_3CHO \rightarrow H_2 + CH_2{=}C{=}O$	28.3 ± 0.4	26.2 ± 0.2
10	$CH_3CHO \rightarrow CH_4 + CO$	-5.1 ± 0.1	-6.0 ± 0.1
11	$CH_3CHO \rightarrow HC^{o}CH + H_2O$	36.2 ± 0.2	34.5 ± 0.2
12	$CH_3CHO \rightarrow CH_2{=}CHOH$	9.5 ± 0.3	9.7 ± 0.3
13	$CH_2{=}CH\text{-}OH \rightarrow CH_2CHO + H$	86.1 ± 0.4	84.7 ± 0.4
	Reaction Enthalpies/kcal mol^{-1}	$\Delta_{rxn}H_{298}$	$\Delta_{rxn}H_0$
14	$H + CH_3CHO \rightarrow H_2 + CH_3CO$	-14.9 ± 0.4	-15.4 ± 0.4
15	$H + CH_3CHO \rightarrow H_2 + CH_2CHO$	-8.6 ± 0.4	-8.9 ± 0.4
16	$CH_3 + CH_3CHO \rightarrow CH_4 + CH_3CO$	-16.2 ± 0.5	-15.5 ± 0.5
17	$CH_3 + CH_3CHO \rightarrow CH_4 + CH_2CHO$	-9.9 ± 0.4	-9.1 ± 0.4
18	$H + H \rightarrow H_2$	-104.206 ± 0.001	-103.267 ± 0.001
19	$H + CH_3 \rightarrow CH_4$	-105.5 ± 0.1	-103.4 ± 0.1
20	$CH_3 + CH_3 \rightarrow CH_3\text{-}CH_3$	-90.2 ± 0.1	-88.0 ± 0.1

Auxiliary Thermochemistry	$\Delta_f H_{298}$/kcal mol^{-1}	$\Delta_f H_0$/kcal mol^{-1}
H	52.103 ± 0.001	51.633 ± 0.001
CO	-26.42 ± 0.01	-27.20 ± 0.01
H_2O	-57.80 ± 0.01	-57.10 ± 0.01
HCºCH	54.3 ± 0.2	54.5 ± 0.2
CH_3CHO	-39.6 ± 0.1	-37.1 ± 0.1
CH_2CHO	3.8 ± 0.4	5.6 ± 0.4
CH_3CO	-2.5 ± 0.4	-0.9 ± 0.4
CH_2=C=O	-11.4 ± 0.4	-10.9 ± 0.1
CH_4	-18.3 ± 0.1	-15.9 ± 0.1
CH_3	35.1 ± 0.1	35.9 ± 0.1
CH_2	93.5 ± 0.4	93.4 ± 0.4
CH_3CH_3	-20.1 ± 0.1	-16.3 ± 0.1
HCO	10.1 ± 0.1	10.0 ± 0.1
HCHO	-26.0 ± 0.1	-25.1 ± 0.1
CH_2=CHOH	-30.1 ± 0.2	-27.4 ± 0.2
CH_3-C-OH	17 ± 6	

	k^{II}/cm^3 molecule^{-1} sec^{-1}
$H + CH_3CHO \rightarrow H_2 + CH_3CO$	$2 \times 10^{-10} \exp(-7\ [\text{kcal/mole}]/RT)$[15]
$H + CH_3CHO \rightarrow H_2 + CH_2CHO$	$7 \times 10^{-10} \exp(-10\ [\text{kcal/mole}]/RT)$[15]
$CH_3 + CH_3CHO \rightarrow CH_4 + CH_3CO$	$3 \times 10^{-12} \exp(-8\ [\text{kcal/mole}]/RT)$[15]
$CH_3 + CH_3CHO \rightarrow CH_4 + CH_2CHO$	$10 \times 10^{-12} \exp(-11\ [\text{kcal/mole}]/RT)$[15]

Table 5.2
Parameters used for acetaldehyde branching ratios

Species	HCCH	HOD
m/z (i)	26.04	19.02
±	0.0001063	0.0001034
Temperature (K)	1675	1675
Photon Energy (eV)	12.68	12.68
σ (E_i) PI Cross Section(mb) at RT	32.42	6
±	8	0.54
Reference	85	86
ϕ(E_i) Photon Power or Photon Flux = (Photocurrent/photodiode Efficiency)	5.948	5.948
±	1.1897	1.1897
D_i Mass Discrimination Factor (√amu)	5.103	4.362
±	0.001042	0.001186
S^+_i Ion Signal at interaction Region	9211	2007
Uncertainty from Poisson Statistics $\sqrt{(S_i^+)}/ S_i^+$	0.01042	0.02232
Uncertainty in percent from Poisson Statistics($\sqrt{(S_i^+)}/ S_i^+$) x 100	0.01042	0.02232
n_i Number Density at interaction region(True Counts)	9.360	12.893
± Overall Uncertainty	0.1009	0.04811
± Overall Uncertainty in Percent	10.09	4.811
Species	HCCH	HOD

References for Chapter V

(1) A. Vasiliou, K. M. Piech, X. Zhang, M. R. Nimlos, M. Ahmed, A. Golan, O. Kostko, D. L. Osborn, J. W. Daily, J. F. Stanton, and G. B. Ellison, J. Chem. Phys. 2011, **135**, 14366.

(2) F. O. Rice and K. F. Herzfeld, J. Am. Chem. Soc. **56**, 284-289 (1934).

(3) M. B. Colket, D. W. Naegeli, and I. Glassman, Int. J. Chem. Kinetics **7**, 223-247 (1975).

(4) J. Ernst and K. Spindler, Berichte Der Bunsen-Gesellschaft-Physical Chemistry Chemical Physics **79**, 1163-1163 (1975).

(5) J. Ernst, K. Spindler, and H. G. Wagner, Berichte Der Bunsen-Gesellschaft-Physical Chemistry Chemical Physics **80**, 645-650 (1976).

(6) E. W. Kaiser, C. K. Westbrook, and W. J. Pitz, Int. J. Chem. Kinetics **18**, 655-688 (1986).

(7) J. Cavanagh, R. A. Cox, and G. Olson, Combustion and Flame **82**, 15-39 (1990).

(8) P. L. Houston, *Chemical Kinetics and Reaction Dynamics*, Dover Ed. ed. (Dover Publications, Inc., Mineola, New York, 2006). Example 2.7: The Rice Herzfeld Mechanism for Decomposition of Acetaldehyde, p. 74

(9) K. J. Laidler and M. T. H. Liu, Proc. Roy. Soc. (London) **297**, 365-375 (1967).

(10) M. T. H. Liu and K. J. Laidler, Canadian Journal of Chemistry **46**, 479-& (1968).

(11) P. Dagaut, M. Reuillon, D. Voisin, M. Cathonnet, M. McGuinness, and J. M. Simmie, Combustion Science and Technology **107**, 301-316 (1995).

(12) K. S. Gupte, J. H. Kiefer, R. S. Tranter, S. J. Klippenstein, and L. B. Harding, Proc. Comb. Inst. **31**, 167-174 (2007).

(13) T. Bentz, F. Striebel, and M. Olzmann, J. Phys. Chem. A **112**, 6120-6124 (2008).

(14) R. Sivaramakrishnan, J. V. Michael, and S. J. Klippenstein, J. Phys. Chem. A **114**, 755-764 (2010).

(15) K. Yasunaga, S. Kubo, H. Hoshikawa, T. Kamesawa, and Y. Hidaka, Int. J. Chem. Kinetics **40**, 73-102 (2008).

(16) N. Leplat and J. Vandooren, Combustion Science and Technology **182**, 436-448 (2010).

(17) B. Ruscic, J. E. Boggs, A. Burcat, A. G. Csaszar, R. Janoschek, J. Demaison, J. M. L. Martin, M. L. Morton, M. J. Rossi, J. F. Stanton, P. G. Szalay, P. R. Westmoreland, F. Zabel, and T. Berces, Journal of Physical and Chemical Reference Data **34**, 573-656 (2005). The heats of formation have been measured: $\Delta_f H_{298}(CH_3CHO)$ = -39.6 ± 0.1 kcal mol^{-1}, $\Delta_f H_{298}(CH_3)$ = 35.9 ± 0.1 kcal mol^{-1}, and $\Delta_f H_{298}(HCO)$ = 10.0 ± 0.1 kcal mol^{-1}. Consequently $DH_{298}(CH_3\text{-}CHO)$ = 84.8 ± 0.2 kcal mol^{-1}

(18) C. R. Moylan and J. I. Brauman, Annu. Rev. Phys. Chem. **34**, 187 (1983).

(19) J. Berkowitz, G. B. Ellison, and D. Gutman, J. Phys. Chem. **98**, 2744-2765 (1994).

(20) S. J. Blanksby and G. B. Ellison, Acct. Chem. Res. **36**, 255-263 (2003).

(21) J. E. Bartmess, J. A. Scott, and R. T. McIver, Jr., J. Am. Chem. Soc. **101**, 6047 (1979).

(22) J. E. Bartmess, SRB Database 19B, NIST Negative Ion Energetics Database, (Office of Standard Reference Data, NIST, Gaithersburg, MD 20899, April 1990).

(23) R. D. Mead, K. R. Lykke, W. C. Lineberger, J. Marks, and J. I. Brauman, J. Chem. Phys. **81**, 4883 (1984).

(24) The acidity/EA cycle uses negative ion chemistry to measure bond enthalpy, $DH_{298}(RH)$, for a species, RH. The working relationship is: $DH_{298}(R\text{-}H) = \Delta_{acid}H_{298}(R\text{-}H) + EA_0(R) - IE_0(H)$ + [thermal correction]. The [thermal correction] = $\int dT\ [C_p(R) - C_p(R^-) + C_p(H) - C_p(H^+)]$ and is roughly 0.3 kcal mol^{-1}. For the case of CH_3CHO, we find $DH_{298}(H\text{-}CH_2CHO)$ = (365.9 ± 2.2 kcal mol^{-1}) + (1.8248 ± 0.0006 eV) - (13.5984 ± 0.0001 eV) = 94 ± 2 kcal mol^{-1}.

(25) D. J. Knowles and A. J. C. Nicholson, J. Chem. Phys. **60**, 1180-1181 (1974). The ionization energy of acetaldehyde was measured by photoionization mass spectroscopy and $IE(CH_3CHO)$ was found to be 10.229_5 ± 0.0007 eV.

(26) J. A. Blush, P. Chen, R. T. Wiedmann, and M. G. White, J. Chem. Phys. **98**, 3557-3559 (1993). $IE(CH_3)$ = 79349 ± 3 cm^{-1} (9.8386 ± 0.0004 eV)

(27) S. Willitsch, A. Haldi, and F. Merkt, Chem. Phys. Lett. **353**, 167-177 (2002). $IE(CH_2CO)$ = 77538.7 ± 0.7 cm^{-1}, $IE(CD_2CO)$ = 77533.4 ± 0.7 cm^{-1}

(28) S. P. McGlynn and J. L. Meeks, Journal of Electron Spectroscopy and Related Phenomena **6**, 269-279 (1975).

(29) R. W. Field, J. Chem. Phys. (2009).

(30) C. A. Taatjes, N. Hansen, A. McIlroy, J. A. Miller, J. P. Senosiain, S. J. Klippenstein, F. Qi, L. S. Sheng, Y. W. Zhang, T. A. Cool, J. Wang, P. R. Westmoreland, M. E. Law, T. Kasper, and K. Kohse-Hoinghaus, Science **308**, 1887-1889 (2005). $IE(CH_2{=}CH\text{-}OH) \leq$ 9.33 ± 0.05 eV

(31) T. H. Osterheld and J. I. Brauman, J. Am. Chem. Soc. **115**, 10311-10316 (1993).

(32) K. C. Lau and C.-Y. Ng, Acct. Chem. Res. **39**, 823-829 (2006). *IE*(HCCH) = 11.4006 ± 0.0006 eV; *IE*(H_2O) = 12.61737 ± 0.00025 eV

(33) T. Shimanouchi, *Tables of Vibrational Frequencies, Consolidated Vol. I*. (NSRDS-NBS 39, 1972). Of the 5 modes of HC≡CH, only the asymmetric CH stretch, σ_u ν_3, and the asymmetric HCCH bend, π_u ν_5, are IR active. In the gas-phase ν_3 HCCH is observed at 3294.9 cm^{-1} and 3281.9 cm^{-1} and is split by a Darling-Dennison resonance (DDR) of 13 cm^{-1}. In an Ar matrix, ν_3 shifts to 3302 cm^{-1} and 3288 cm^{-1}; the DDR is 14 cm^{-1} in the cryogenic matrix. The gas phase value for ν_5 is 730.3 cm^{-1} and shifts to 736.8 cm^{-1} in an Ar matrix.

(34) V. A. Walters, S. D. Colson, D. L. Snavely, K. B. Wiberg, and B. M. Jamison, J. Phys. Chem. **89**, 3857-3861 (1985).

(35) K. B. Wiberg, Y. Thiel, L. Goodman, and J. Leszczynski, J. Phys. Chem. **99**, 13850-13864 (1995).

(36) We observe ν_1(CH_2CHO-H) = 3620 cm-1; ν_5(CH_2=CHOH) = 1662 cm^{-1}; and the out-of-plane wag, ν_{13}(CH_2=CHOH), appears as a complex doublet at 814 and 818 cm^{-1}.

(37) M. Rodler, C. E. Blom, and A. Bauder, J. Am. Chem. Soc. **106**, 4029-4035 (1984). Vinyl alcohol was produced by pyrolysis of cyclobutanol into an argon matrix. Strong fundamental bands were found for ν_1(CH_2CHOH) = 3619.9 cm^{-1}, ν_5(CH_2CHOH) = 1661.9 and 1663.0 cm^{-1} (FR with $2\nu_{13}$), and ν_{13}(CH_2CHOH) = 813.7 cm^{-1} with shoulders at 813 and 818 cm^{-1}.

(38) D. L. Joo, A. J. Merer, and D. J. Clouthier, J. Mol. Spectry **197**, 68-75 (1999).

(39) Actual frequencies that are observed are ν_1(CH_2CHO-H) = 3620 cm^{-1}; ν_1(CH_2CDO-H) = 3621 cm^{-1}; ν_1(CD_2CHO-D) = 2675 cm^{-1}; ν_1(CD_2CDO-D) = 2675 cm^{-1}. The values observed for ν_{OH} agree closely with those reported by Rodler *et al*. There are no literature values published for us to compare the frequencies of CD_2CHOD and CD_2CDOD detected here. But Rodler *et al*. find ν_1(CH_2CHO-D) = 2672 cm^{-1}.

(40) S. M. Burnett, A. E. Stevens, C. S. Feigerle, and W. C. Lineberger, Chem. Phys. Lett. **100**, 124-128 (1983).

(41) K. M. Ervin, J. Ho, and W. C. Lineberger, J. Chem. Phys. **91**, 5974-5992 (1989).

(42) M. K. Gilles, W. C. Lineberger, and K. M. Ervin, J. Am. Chem. Soc. **115**, 1031-1038 (1993).

(43) R. F. Gunion, H. Koppel, G. W. Leach, and W. C. Lineberger, J. Chem. Phys. **103**, 1250-1262 (1995).

(44) R. F. Gunion and W. C. Lineberger, J. Phys. Chem. **100**, 4395-4399 (1996).

(45) Y. Q. Chen, D. M. Jonas, J. L. Kinsey, and R. W. Field, J. Chem. Phys. **91**, 3976-3987 (1989).

(46) M. P. Jacobson and R. W. Field, J. Phys. Chem. A **104**, 3073-3086 (2000).

(47) R. L. Hayes, E. Fattal, N. Govind, and E. A. Carter, J. Am. Chem. Soc. **123**, 641-657 (2001).

(48) H. Schuchma and K. J. Laidler, Canadian Journal of Chemistry **48**, 2315-& (1970).

(49) G. da Silva and J. W. Bozzelli, J. Phys. Chem. A **110**, 13058-13067 (2006).

(50) B. C. Shepler, B. J. Braams, and J. M. Bowman, J. Phys. Chem. A **111**, 8282–8285 (2007).

(51) B. C. Shepler, B. J. Braams, and J. M. Bowman, J. Phys. Chem. A **112** 9344–9351 (2008).

(52) X. P. Liu, M. L. Gross, and P. G. Wenthold, J. Phys. Chem. A **109**, 2183-2189 (2005).

(53) Acetaldehyde could rearrange to the vinyl alcohol *via* the methylhydroxycarbene: $CH_3CHO \rightarrow [CH_3\text{-}C\text{-}OH] \rightarrow CH_2{=}CH\text{-}OH$. But this pathway would predict that the vinyl alcohol resulting from CH_3CDO would be $CH_3CDO \rightarrow [CH_3\text{-}C\text{-}OD] \rightarrow CH_2{=}CH\text{-}OD$. Fig. 6 shows that the vinyl alcohol resulting from CH_3CDO is $CH_2{=}CD\text{-}OH$. Likewise, when CD_3CHO rearranges, we observe $CD_2{=}CHOD$ and not $CD_2{=}CD\text{-}OH$.

(54) X. Xing, B. Reed, M. K. Bahng, and C. Y. Ng, J. Phys. Chem. A **112**, 2572-2578 (2008). $IE(CH_2CH_2) = 10.51268 \pm 0.00025$ eV

(55) D. M. Golden, Int. J. Chem. Kinetics (2008).

(56) A. M. Scheer, C. Mukarakate, D. J. Robichaud, G. B. Ellison, and M. R. Nimlos, J. Phys. Chem. A **114**, 9043-9056 (2010).

(57) A. Streitwieser , C. H. Heathcock, and E. M. Kosower, *Introduction to Organic Chemistry*, 4th Ed. ed. (Prentice Hall, Upper Saddle River, NJ 07458, 1977). The mechanism for acid catalyzed keto-enol tautermization of CH_3CHO is described on p. 424. In aqueous solution at 300 K, $K_{equi}(CH_3CHO, CH_2{=}CHOH)$ is 6×10^{-7}. The discussion of *E1* reactions that are catalyzed by Al_2O_3 is found on p 269.

(58) F. A. Cotton and G. Wilkenson, *Advanced Inorganic Chemistry: A Comprehensive Text*, 2nd ed. (Wiley-Interscience, New York, 1966).

(59) The manufacturer (Saint-Gobain Ceramics) of the carborandum tubes lists the typical impurities as: SiC 98.0 (wt. %) Al (132 ppm), B (6900 ppm), C either graphite or "dirt" (5300 ppm), Ca (7 ppm), Cr (< 0.3 ppm), Cu (< 1 ppm), Fe (6 ppm), K (< 1.3 ppm), Na (< 0.6 ppm), Ni (< 3 ppm), Ti (18 ppm), V (17 ppm), Zn (1 ppm), Zr (5 ppm)

(60) E. B. Jochnowitz, X. Zhang, M. R. Nimlos, M. E. Varner, J. F. Stanton, and G. B. Ellison, J. Phys. Chem. A **109**, 3812-3821 (2004).

(61) A. Vasiliou, M. R. Nimlos, J. W. Daily, and G. B. Ellison, J. Phys. Chem. A **113**, 8540-8547 (2009).

(62) E. McCormack, J. M. Gilligan, C. Cornaggia, and E. E. Eyler, (1989). $IE(H_2)$ = 15.425932 ± 0.000002 eV

(63) K. P. Huber and G. Herzberg, (1979). $IE(D_2)$ = 15.4666 ± 0.0001 eV

(64) D. Shiner, J. M. Gilligan, B. M. Cook, and W. Lichten, (1993). *IE*(HD) = 15.44465 ± 0.00001 eV

(65) R. Signorell and F. Merkt, J. Chem. Phys. **110**, 2309-2311 (1999). Because of the pre-dissociation effects and Jahn-Teller dynamics of the cation, observation of CH_4^+ (m/z 16) by PIMS is not easy.

(66) R. Signorell, M. Sommavilla, and F. Merkt, Chem. Phys. Lett. **312**, 139-148 (1999).

(67) T. Shimanouchi, *Tables of Vibrational Frequencies. Consolidated Volume I*. (NSRDS-NBS 39, 1972). Methane has four vibrational modes but only the degenerate CH stretch, f_2 ν_3, and the degenerate deformation, f_2 ν_4, are IR active. In the gas-phase ν_3 CH_4 is observed at 3019.9 cm^{-1} and ν_4 CH_4 is found at 1306.2 cm^{-1}. These values shift in an Ar matrix to ν_3 = 3032 cm^{-1} and ν_4 = 1305 cm^{-1}. The signal from ν_4 is very intense and easy to detect in an cryogenic matrix.

(68) P. L. Houston and S. H. Kable, Proceedings of the National Academy of Sciences of the United States of America **103**, 16079-16082 (2006).

(69) B. R. Heazlewood, M. J. T. Jordan, S. H. Kable, T. M. Selby, D. L. Osborn, B. C. Shepler, B. J. Braams, and J. M. Bowman, Proceedings of the National Academy of Sciences of the United States of America **105**, 12719-12724 (2008).

(70) B. R. Heazlewood, A. T. Maccarone, D. U. Andrews, D. L. Osborn, L. B. Harding, S. J. Klippenstein, M. J. T. Jordan, and S. H. Kable, Nature Chemistry **3**, 443-448 (2011).

(71) L. B. Harding, Y. Georgievskii, and S. J. Klippenstein, J. Phys. Chem. A **114**, 765-777 (2010).

(72) B. C. Shepler, Y. C. Han, and J. M. Bowman, Journal of Physical Chemistry Letters **2**, 834-838 (2011).

(73) Y. C. Han, B. C. Shepler, and J. M. Bowman, Journal of Physical Chemistry Letters **2**, 1715-1719 (2011).

(74) J. M. Bowman and B. C. Shepler, in *Annual Review of Physical Chemistry*, edited by S. R. Leone, P. S. Cremer, J. T. Groves, and M. A. Johnson (2011), Vol. 62, pp. 531-553.

(75) L. V. Gurvich, I. V. Veyts, C. B. Alcock, and V. S. Iorish, *Thermodynamic Properties of Individual Substances*, 4th ed. (Hemisphere, New York City, 1991).

(76) T. Ichino and J. F. Stanton, (2010).

(77) A. Tajti, P. G. Szalay, A. G. Csaszar, M. Kallay, J. Gauss, E. F. Valeev, B. A. Flowers, J. Vazquez, and J. F. Stanton, J. Chem. Phys. **121**, 11599-11613 (2004).

(78) B. Ruscic, J. E. Boggs, A. Burcat, A. G. Csaszar, J. Demaison, R. Janoschek, M. L. Morton, J. M. L. Martin, M. J. Rossi, J. F. Stanton, P. G. Szalay, P. R. Westmoreland, F. Zabel, and T. Berces, Journal of Physical and Chemical Reference Data **34**, 573-656 (2005). The heats of formation have been measured: $\Delta_f H_{298}(CH_3CHO)$ = -39.6 ± 0.1 kcal mol^{-1}, $\Delta_f H_{298}(CH_3CO)$ = -2.5 ± 0.4 kcal mol^{-1}, and $\Delta_f H_{298}(H)$ = 52.103 ± 0.001 kcal mol^{-1}. Consequently $DH_{298}(CH_3CO\text{-}H)$ = 89.3 ± 0.4 kcal mol^{-1}

(79) J. B. Pedley, R. D. Naylor, and S. P. Kirby, *Thermochemistry of Organic Compounds*, 2 ed. (Chapman and Hall, New York, 1986). $\Delta_f H_0(CH_2CO)$ from JFS

(80) B. Ruscic, J. E. Boggs, A. Burcat, A. G. Csaszar, J. Demaison, R. Janoschek, J. M. L. Martin, M. L. Morton, M. J. Rossi, J. F. Stanton, P. G. Szalay, P. R. Westmoreland, F. Zabel, and T. Berces, Journal of Physical and Chemical Reference Data **34**, 573-656 (2005).

(81) B. Ruscic, M. Litorja, and R. L. Asher, J. Phys. Chem. A **104**, 8600-8600 (2000). $\Delta_f H_{298}(CH_3)$ = 35.05 ± 0.07 kcal mol^{-1}

(82) K. M. Ervin and V. F. DeTuri, J. Phys. Chem. A **106**, 9947-9956 (2002).

(83) A. C. Terentis and S. H. Kable, Chem. Phys. Lett. **258**, 626-632 (1996). D_0(H-HCO) = 30328.5 ± 0.5 cm^{-1}; $\Delta_f H_0$(HCO) = 42.5 ± 0.5 kJ mol-1

(84) K. C. Thompson, D. L. Crittenden, S. H. Kable, and M. J. T. Jordan, J. Chem. Phys. **124**, 044302 (2006).

(85) Cool, T.A. et al. A photoionization mass spectrometer for stuides of flame chemistry with a synchrotron light source. Review of Scientific Instruments. American Institute of Physics.

(86) Katayama, D.H., Huffman, R.E. and Obryan, C.L., *J. Chem. Phys.* **1973**, *59*, 4309

Bibliography

Biofuels in the European Union: *A Vision for 2030 and Beyond*; **2006**.

In U. S. Department of Energy, Office of the Biomass Program (OBP) 30 x 30 Workshop, http://www.30x30workshop.biomass.govtools.us/, L'Enfant PlazaHotel, Washington, D. C., August 1-2, **2006**; L'Enfant Plaza Hotel, Washington, D. C., August 1-2, 2006.

Evans, R. J.; Milne, T. A.; Soltys, M. N. *Journal of Analytical and Applied Pyrolysis,* **1986**, 9, 207.

Evans, R. J.; Milne, T. A. *Energy & Fuels*, **1987**, 1, 123.

Evans, R. J.; Milne, T. A. *Energy & Fuels*, **1987**, 1, 311.

A Survey of Biomass Gasification; Reed, T. B., Ed.; Solar Energy Research Institute: Golden, CO, 1979; Vol. **II** *Principles of Gasification*.

Bridgewater, A. V. *Fuel* **1995**, *74*, 631.

Yaman, S. *Energy Conversion and Management* **2004**, *45*, 651.

Shafizadeh, F. *J. Anal. Appl. Pyrolysis* **1982**, *3*, 283.

Antal, M. J.; Varhegyi, G.; Jakab, E. *Ind. Eng. Chem. Res.* **1998**, *37*, 1267.

Diebold, J. P. *Biomass & Bioenergy* **1994**, *7*, 75.

Antal, M. J.; Varhegyi, G. *Ind. Eng. Chem. Res.* **1995**, *34*, 703.

O'Sullivan, A. C. *Cellulose* **1997**, *4*, 173.

Matthews, J. F.; Skopec, C. E.; Mason, P. E.; Zuccato, P.; Torget, R. W.; Sugiyama, J.; Himmel, M. E.; Brady, J. W. *Carbohydr. Res.* **2006**, *341*, 138.

Chen, P.; Chupka, W.A.; Berson, J.A. *J.Phys. Chem.* **1986**, 90. 2319.

Zhang, X.; Friderichsen, A.V.; Nandi, S.; Ellison, G.B.; David, D.E.; McKinnon, J.T.; Lindeman, T.G.; Dayton, D.C.; Nimlos, M.R. *Rev Sci. Instrum.* **2003**, 74, 3077.

Meyer, B. *Low Temperature Spectroscopy*; Elsevier: New York **1971**.

Norrish, R.G.W.; Porter, G. *Nature* **1949**, 164, 658.

Daily, J.W.; Guan, Q.; Vasiliou, A.K.; Nimlos, M.R.; Ellison, G.B. Int.. J. Chem. Kin. (to be submitted)

Miller, D.R. *In Atomic and Molecular Beam Methods*, edited by Scoles, G.; Oxford University Press, New York, **1988**, Vol. 1.

Shapiro, A. *The Dynamics and Thermodynamics of Compressible Fluid Flow*, The Ronald Press CO., **1953**, Vol 1.

Anderson, J. *AIAA Journal* **1972,** 10, 112.

Bier, K.; Schmidt, B.; *Z. Angew* **1961**, 13, 493

Instruction Manual AREF Time of Flight Power Supply from Jordon TOF products, Inc.; Grass Valley,

Guilhaus, M. *J. Mass Spectrom*. **1995,** 30, 1519.

Evan, U.; Dick. D. *Rev. Sci. Instrum.* **2000**, 71, 4415.

Whittle, E.; Dows, D.A.; Pimentel, G.C.; *J. Chem. Phys*. **1954**, 22, 1943

Nandi, S.; *PhD. Thesis*, University of Colorado, **2001**

Smith, M.H.; Rinsland, C.P.; Fridovich, B.; Rao, K.N. Intensities and Collision Broadening Parameters from Infrared Spectra. In Molecular Spectroscopy: A Modern Research; Academic Press, **1985**, Vol III

Nandi, S.; Blanksby, S.J.; Zhang, X.; Nimlos, M.R.; Dayton, D.C.; Ellison, G.B. *J. Phys. Chem. A*. **2002**, 106, 7547.

Jachnowitz, E.B.; *PhD Thesis*, University of Colorado, **2004.**

Maccarone, A.T.; *PhD Thesis*, University of Colorado, **2007**

http://www-als.lbl.gov/

http://www.chemicaldynamics.lbl.gov/btw.html

Beaumont, O. *Wood and Fiber Science* **1985**, *17*, 228.

Piskorz, J.; Radlein, D.; Scott, D. S. *J. Anal. Appl. Pyrolysis* **1986**, *9*, 121.

Evans, R. J.; Milne, T. A. *Energy & Fuels* **1987**, *1*, 123.

Evans, R. J.; Milne, T. A. *Energy & Fuels* **1987**, *1*, 311.

Shafizadeh, F.; Lai, Y. Z. *J. Org. Chem.* **1972**, *37*, 278.

Shafizadeh, F.; McGinnis, G. D.; Philpot, C. W. *Carbohydr. Res.* **1972**, *25*, 23.

Shafizadeh, F.; Lai, Y. Z.; McIntyre, C. R. *J. Appl. Polymer Sci.* **1978**, *22*, 1183.

Phillips, S. D. *Ind. Eng. Chem. Res.* **2007**, *46*, 8887.

Grela, M. A.; Amorebieta, V. T.; Colussi, A. J. *J. Phys. Chem.* **1985**, *89*, 38.

Hore, N. R.; Russell, D. K. *New J. Chem.* **2004**, *28*, 606.

Fulle, D.; Dib, A.; Kiefer, J. H.; Zhang, Q.; Yao, J.; Kern, R. D. *J. Phys. Chem. A* **1998**, *102*, 7480.

Organ, P. P.; Mackie, J. C. *J. Chem. Soc. - Faraday Trans.* **1991**, *87*, 815.

Bruinsma, O. S. L.; Tromp, P. J. J.; Nolting, H.; Moulijn, J. A. *Fuel* **1988**, *67*, 334.

Lifshitz, A.; Bidani, M.; Bidani, S. *J. Phys. Chem.* **1986**, *90*, 5373.

Friderichsen, A. V.; Shin, E. J.; Evans, R. J.; Nimlos, M. R.; Dayton, D. C.; Ellison, G. B. *Fuel* **2001**, *80*, 1747.

Jochnowitz, E. B.; Zhang, X.; Nimlos, M. R.; Varner, M. E.; Stanton, J. F.; Ellison, G. B. *J. Phys. Chem. A* **2004**, *109*, 3812.

Rohrs, H. W.; Wickham-Jones, C. T.; Berry, D.; Ellison, G. B.; Argrow, B. M. *Rev. Sci. Instrum.* **1995**, *66*, 2430.

Zhang, X.; Friderichsen, A. V.; Nandi, S.; Ellison, G. B.; David, D. E.; McKinnon, J. T.; Lindeman, T. G.; Dayton, D. C.; Nimlos, M. R. *Rev. Sci. Inst.* **2003**, *74*, 3077.

Friderichsen, A. V.; Radziszewski, J. G.; Nimlos, M. R.; Winter, P. R.; Dayton, D. C.; David, D. E.; Ellison, G. B. *J. Am. Chem. Soc.* **2001**, *123*, 1977.

Nandi, S.; Arnold, P. A.; Carpenter, B. K.; Nimlos, M. R.; Dayton, D. C.; Ellison, G. B. *J. Phys. Chem. A* **2001**, *105*, 7514.

Nandi, S.; Blanksby, S. J.; Zhang, X.; Nimlos, M. R.; Dayton, D. C.; Ellison, G. B. *J. Phys. Chem. A* **2002**, *106*, 7547.

Chen, P.; Colson, S. D.; Chupka, W. A.; Berson, J. A. *J. Phys. Chem.* **1986**, *90*, 2319.

Brown, A. L.; Dayton, D. C.; Nimlos, M. R.; Daily, J. W. *Energy & Fuels* **2001**, *15*, 1276.

Blanksby, S. J.; Ellison, G. B. *Acct. Chem. Res.* **2003**, *36*, 255.

Pedley, J. B.; Naylor, R. D.; Kirby, S. P. *Thermochemistry of Organic Compounds*, 2 ed.; Chapman and Hall: New York, 1986. The 298 K enthalpies of formation are: CO (-26.42 ± 0.04 kcal mol^{-1}), CH_3CCH (44.2 ± 0.2 kcal mol^{-1}), HCCH (54.3 ± 0.2 kcal mol^{-1}), and CH_2CO (-11.4 ± 0.4 kcal mol^{-1}).

Herzberg, G. H. *Molecular Spectra and Molecular Structure: Electronic Spectra and Electronic Structure of Polyatomic Molecules*; D. Van Nostrand: Princeton, New Jersey, 1967; Vol. III.

Baker, C.; Turner, D. W. *Proc. Roy. Soc. (London)* **1968**, *308*, 19. *IE*(CH_3CCH) = 10.37 ± 0.01 eV

Hall, D.; Maier, J. P.; Rosmus, P. *Chem. Phys.* **1977**, *24*, 373.

Niu, B. H.; Bai, Y.; Shirley, D. A. *J. Chem. Phys.* **1993**, *99*, 2520. *IE*(CH_2CO) = 9.6191 ± 0.0004 eV

Gilbert, T.; Pfab, R.; Fischer, I.; Chen, P. *J. Chem. Phys.* **2000**, *112*, 2575.

Lau, K. C.; Ng, C. Y. *Acct. Chem. Res.* **2006**, *39*, 823.

Erman, P.; Karawajczyk, A.; Rachlewkallne, E.; Stromholm, C.; Larsson, J.; Persson, A.; Zerne, R. *Chem. Phys. Lett.* **1993**, *215*, 173.

Chewter, L. A.; Sander, M.; Müller-Dethlefs, K.; Schlag, E. W. *J. Chem. Phys.* **1987**, *86*, 4737. $IE(C_6H_6)$ = 9.24372 ± 0.00005 eV

Lipert, R. J.; Colson, S. D. *J. Phys. Chem.* **1990**, *94*, 2358. $IE(C_6H_5OH)$ = 8.508 ± 0.001 eV

Dyke, J. M.; Ozeki, H.; Takahashi, M.; Cockett, M. C. R.; Kimura, K. *J. Chem. Phys.* **1992**, *97*, 8926. $IE(C_6H_5CH{=}CH_2)$ = 8.464 ± 0.001 eV

Robinson, M. S.; Polak, M. L.; Bierbaum, V. M.; DePuy, C. H.; Lineberger, W. C. *J. Am. Chem. Soc.* **1995**, *117*, 6766. DH_{298}(H-CH_2CCH) = 90 ± 3 kcal mol^{-1}; enthalpy of formation (298K) (CH_2CCH) = 82.5 ± 3.0 kcal mol^{-1}

Alkemade, U.; Homann, K. H. *Zeitsch. Phys. Chem.* **1989**, *161*, 19.

Morter, C. L.; Farhat, S. K.; Adamson, J. D.; Glass, G. P.; Curl, R. F. *J. Phys. Chem.* **1994**, *98*, 7029.

Atkinson, D. B.; Hudgens, J. W. *J. Phys. Chem. A* **1999**, *103*, 4242.

Fahr, A.; Nayak, A. *Int. J. Chem. Kinetics* **2000**, *32*, 118.

Scherer, S.; Just, T.; Frank, P. *Proc. Comb. Inst.* **2000**, *28*, 1511.

Miller, J. A.; Klippenstein, S. J. *J. Phys. Chem. A* **2001**, *105*, 7254.

DeSain, J. D.; Taatjes, C. A. *J. Phys. Chem. A* **2003**, *107*, 4843.

Miller, J. A.; Klippenstein, S. J. *J. Phys. Chem. A* **2003**, *107*, 7783.

Shafir, E. V.; Slagle, I. R.; Knyazev, V. A. *J. Phys. Chem. A* **2003**, *107*, 8893.

Tang, W. Y.; Tranter, R. S.; Brezinsky, K. *J. Phys. Chem. A* **2005**, *109*, 6056.

Tang, W. Y.; Tranter, R. S.; Brezinsky, K. *J. Phys. Chem. A* **2006**, *110*, 2165.

Sendt, K.; Bacskay, G. B.; Mackie, J. C. *J. Phys. Chem. A* **2000**, *104*, 1861.

Ervin, K. M.; DeTuri, V. F. *J. Phys. Chem. A* **2002**, *106*, 9947. $D_0(C_6H_5\text{-}H) = 111.3 \pm 0.5$ kcal mol^{-1} and $DH_{298}(C_6H_5\text{-}H) = 112.9 \pm 0.5$ kcal mol^{-1}

Deanm F.M Naturally Occuring Ring Compounds, Butterworths, London. **1963**

Robertson, G.L and Samaniego, C.M.L, *J. Food Sci*. **1986**, *51*, 184.

Kaanane, A., Kane, D., and Labuza, T.P., *J. Food Sci*. **1988**, *53*, 1470.

EI-Nemur, S. E., Ismail, I. A., and Askar, A., *Food Chem*. **1988**, *10*, 269

Calvi, J. P. and Francis, F. J., *J. Food Sci*. **1978**, *43*, 1448.

Rapp, A., Guntert, M., and Ullemeyer, H., *Z. Lebensm. Unters. Forsch*. **1985**, *180*, 109.

Simpson, R. F., *J. Sci. Food Agric*. **1980**, 31, 214-222.

HoweUs, J. S., Johnston, D., and Vojodic, P. R., *Anal. Proc*. **1988** *25*, 162.

Service, E. G., Shinnie, G. B., and MacLeod, T. M., *J. Clin. Hosp. Pharm*. **1982** *7*, 287.

Hung, C. T., Selkirk, A. B., and Taylor, R. B., *J. Clin. Hosp. Pharm*. **1982** *7*, 17.

Schwald, W., Brownell, H. H., and Saddler, J. N., *J. Wood Chem. Technol*. **1988**, *8*, 543.

Bobleter, O., Schwald, W., Concin, R., and Binder, H., *J. Carbohydr. Chem*. **1986**, *5*, 387.

Bonn, G., and Bobleter, O., Chromatographia **1984**, *18*, 445.

Chapman, G. W., Burdick, D., Higman, H. C., and Robertson, J. A., *J. Sci. Food Agric*. **1978**, *29*, 312.

Garrett, E. R. and Dvorchik, B. H., *J. Pharm. Sci.*, **1969**, *58*, 813.

Grohmann, K., Himmel, M., Rivard, C., Tucker, M., and Baker, *J. Biotechnol. Bioeng. Symp.* **1984**, *14*, 138.

Grohmann, K., Torget, R., and Himmel, M., *Biotechnol. Bioeng. Symp.* **1985**, *15*, 59.

Rivard, C. J., Himmel, M. E., and Grohmann, K., *Biotechnol. Bioeng. Symp*. **1985**, *15*, 375.

Grohmann, K., Torget, R., and Himmel, M., *Biotechnol. Bioeng. Symp.* **1986**, *17*, 135.

McCarty, P. L., Young, L. Y., Stuckey, D. C., and Healy, J. B. Jr. *Microbial Energy Conversion*, Schlegel, H. G. and Barnea, J., eds., Pergamon, Oxford **1977**, 179.

Kottke, R. H. In Kirk-Othmer *Encyclopedia of Chemical Technology*, 4th ed.; Kroschwitz J., Howe-Grant M., Eds.; John Wiley and Sons: New York, **1998**; volume supplement.

Hurd, C.D., Goldsby, A.R., and Osborne, E.N., J. Amer. Chem. Soc. **1932**, *54*, 2532

Garrett, E. R. and Dvorchik, B. H., *J. Pharm. Sci*. **1969**, 58, 813.

Grohmann, K., Himmel, M., Rivard, C., Tucker, M., and Baker, J., *Biotechnol. Bioeng. Symp.* **1984**, 14, 138-157.

Demirbas, A., Fuel Processing Technology, **2007**, *88*, 591.

Antal, M. J.; Leesoboom, T.; Mok, W. S. Richards, G. N., *Carbohydr. Res.* **1991**, *217*, 71.

Evans, R.J., Milne, A., *Energy and Fuels*, **1987**, 1, 123.

Evans, R.J., Milne, A., *Energy and Fuels*, **1987**, 1, 311.

Zeitsch, K. J. *The chemistry and technology of furfural and its many by-products*, 1st ed.; Elsevier: Amsterdam, **2000**; Vol. 13.

Bak, B.; Christensen,D.; Dixon, W. B.; Hansen-Nygaard, L.; Rastrup- Andersen, J.; Schotlander, M., *J. Mol. Spectrosc*. **1962**, *9*, 124.

Rico, M.; Barrachina, M.; Orza, J. M., *J. Mol. Spectrosc.* **1967**, *24*, 133.

Monnig, M.; Dreizler, H.; Rudolph, H. D**.** 2. Nafurforsch., **1965**, *20a*, 1323.

Monnig, H. D.; Dreizler, H.; Rudolph, H. D. 2. Narurforsch., **1966**, *21a*, 1633.

Schultz, G.; Fellegvbry, I.; Kolonits, M.; Kiss, A. I.; Pete, B.; Bbnki, J., *J. Mol. Struct*. **1910**, *50*, 325.

Miller, J.; Fateley, W. G.; Witkowski, R. E., *Spectrochim. Acta,* **1967**, *23a*, 891.

Little, T. S.; Qiu, J.; Durig, J. R., *Spectrochim. Acta* **1989**, *45a*, 789**.**

Grela, M.A. and Colussi, A.J., *J. Phys Chem*., **1986**, *90*, 434.

Grela, M.A. and Colussi, A.J., *An. Asoc. Quim. Aregent*., **1987**, *75*, 111.

Vasiliou, A.K., Ellison, G.B., Nimlos. M.R., and Daily, J.W., *J. Phys. Chem. A,* **2009**, 13 (30), 8540-8547

Ervin, K. M.; DeTuri, V. F. *J. Phys. Chem. A* **2002**, *106*, 9947. $D_0(C_6H_5\text{-}H) = 111.3 \pm 0.5$ kcal mol^{-1} and $DH_{298}(C_6H_5\text{-}H) = 112.9 \pm 0.5$ kcal mol^{-1}

Chewter, L.A.; Sander, M.; Muller-Dethlefs, K.; Schalg, E.W., *J. Chem*. *Phys*., **1987**, *86*, 4737.

Mukarakate, C., Scheer, A.M., Robichaud, D.J., Jarvis, M.W., David, D.E., Ellison, G.B., Nimlos M.R. and Davis, M.F., Rev. of Sci. Instr., **2011**, *82*, 3104.

Knight, A. E. W.; Parmenter, C. S.; Schuyler, M. W., J. *Am. Chem. Soc*. **1975,** *97***,** 1993**.**

Page, R. H.; Shen, Y. R.; Lee, Y. T., *J. Chem. Phys*. **1988**, *88*, 5362.

A. Vasiliou, K. M. Piech, X. Zhang, M. R. Nimlos, M. Ahmed, A. Golan, O. Kostko, D. L. Osborn, J. W. Daily, J. F. Stanton, and G. B. Ellison, J. Chem. Phys. 2011, **135**, 14366 .

F. O. Rice and K. F. Herzfeld, J. Am. Chem. Soc. **56**, 284-289 (1934).

M. B. Colket, D. W. Naegeli, and I. Glassman, Int. J. Chem. Kinetics **7**, 223-247 (1975).

J. Ernst and K. Spindler, Berichte Der Bunsen-Gesellschaft-Physical Chemistry Chemical Physics **79**, 1163-1163 (1975).

J. Ernst, K. Spindler, and H. G. Wagner, Berichte Der Bunsen-Gesellschaft-Physical Chemistry Chemical Physics **80**, 645-650 (1976).

E. W. Kaiser, C. K. Westbrook, and W. J. Pitz, Int. J. Chem. Kinetics **18**, 655-688 (1986).

J. Cavanagh, R. A. Cox, and G. Olson, Combustion and Flame **82**, 15-39 (1990).

P. L. Houston, *Chemical Kinetics and Reaction Dynamics*, Dover Ed. ed. (Dover Publications, Inc., Mineola, New York, 2006). Example 2.7: The Rice Herzfeld Mechanism for Decomposition of Acetaldehyde, p. 74

K. J. Laidler and M. T. H. Liu, Proc. Roy. Soc. (London) **297**, 365-375 (1967).

M. T. H. Liu and K. J. Laidler, Canadian Journal of Chemistry **46**, 479-& (1968).

P. Dagaut, M. Reuillon, D. Voisin, M. Cathonnet, M. McGuinness, and J. M. Simmie, Combustion Science and Technology **107**, 301-316 (1995).

K. S. Gupte, J. H. Kiefer, R. S. Tranter, S. J. Klippenstein, and L. B. Harding, Proc. Comb. Inst. **31**, 167-174 (2007).

T. Bentz, F. Striebel, and M. Olzmann, J. Phys. Chem. A **112**, 6120-6124 (2008).

R. Sivaramakrishnan, J. V. Michael, and S. J. Klippenstein, J. Phys. Chem. A **114**, 755-764 (2010).

K. Yasunaga, S. Kubo, H. Hoshikawa, T. Kamesawa, and Y. Hidaka, Int. J. Chem. Kinetics **40**, 73-102 (2008).

N. Leplat and J. Vandooren, Combustion Science and Technology **182**, 436-448 (2010).

B. Ruscic, J. E. Boggs, A. Burcat, A. G. Csaszar, R. Janoschek, J. Demaison, J. M. L. Martin, M. L. Morton, M. J. Rossi, J. F. Stanton, P. G. Szalay, P. R. Westmoreland, F. Zabel, and T. Berces, Journal of Physical and Chemical Reference Data **34**, 573-656 (2005). The heats of formation have been measured: $\Delta_f H_{298}(CH_3CHO) = -39.6 \pm 0.1$ kcal mol^{-1}, $\Delta_f H_{298}(CH_3) = 35.9 \pm 0.1$ kcal mol^{-1}, and $\Delta_f H_{298}(HCO) = 10.0 \pm 0.1$ kcal mol^{-1}. Consequently $DH_{298}(CH_3\text{-}CHO) = 84.8 \pm 0.2$ kcal mol^{-1}

C. R. Moylan and J. I. Brauman, Annu. Rev. Phys. Chem. **34**, 187 (1983).

J. Berkowitz, G. B. Ellison, and D. Gutman, J. Phys. Chem. **98**, 2744-2765 (1994).

S. J. Blanksby and G. B. Ellison, Acct. Chem. Res. **36**, 255-263 (2003).

J. E. Bartmess, J. A. Scott, and R. T. McIver, Jr., J. Am. Chem. Soc. **101**, 6047 (1979).

J. E. Bartmess, SRB Database 19B, NIST Negative Ion Energetics Database, (Office of Standard Reference Data, NIST, Gaithersburg, MD 20899, April 1990).

R. D. Mead, K. R. Lykke, W. C. Lineberger, J. Marks, and J. I. Brauman, J. Chem. Phys. **81**, 4883 (1984).

The acidity/EA cycle uses negative ion chemistry to measure bond enthalpy, $DH_{298}(RH)$, for a species, RH. The working relationship is: $DH_{298}(R\text{-}H) = \Delta_{acid}H_{298}(R\text{-}H) + EA_0(R) - IE_0(H) +$ [thermal correction]. The [thermal correction] $= \int dT\ [C_p(R) - C_p(R^-) + C_p(H) - C_p(H^+)]$ and is roughly 0.3 kcal mol^{-1}. For the case of CH_3CHO, we find $DH_{298}(H\text{-}CH_2CHO) = (365.9 \pm 2.2$ kcal mol^{-1}) + (1.8248 ± 0.0006 eV) - (13.5984 ± 0.0001 eV) = 94 ± 2 kcal mol^{-1}.

D. J. Knowles and A. J. C. Nicholson, J. Chem. Phys. **60**, 1180-1181 (1974). The ionization energy of acetaldehyde was measured by photoionization mass spectroscopy and $IE(CH_3CHO)$ was found to be $10.229_5 \pm 0.0007$ eV.

J. A. Blush, P. Chen, R. T. Wiedmann, and M. G. White, J. Chem. Phys. **98**, 3557-3559 (1993). $IE(CH_3) = 79349 \pm 3$ cm^{-1} (9.8386 ± 0.0004 eV)

S. Willitsch, A. Haldi, and F. Merkt, Chem. Phys. Lett. **353**, 167-177 (2002). $IE(CH_2CO) = 77538.7 \pm 0.7$ cm^{-1}, $IE(CD_2CO) = 77533.4 \pm 0.7$ cm^{-1}

S. P. McGlynn and J. L. Meeks, Journal of Electron Spectroscopy and Related Phenomena **6**, 269-279 (1975).

R. W. Field, J. Chem. Phys. (2009).

C. A. Taatjes, N. Hansen, A. McIlroy, J. A. Miller, J. P. Senosiain, S. J. Klippenstein, F. Qi, L. S. Sheng, Y. W. Zhang, T. A. Cool, J. Wang, P. R. Westmoreland, M. E. Law, T. Kasper, and K. Kohse-Hoinghaus, Science **308**, 1887-1889 (2005). $IE(CH_2{=}CH\text{-}OH) \leq 9.33 \pm 0.05$ eV

T. H. Osterheld and J. I. Brauman, J. Am. Chem. Soc. **115**, 10311-10316 (1993).

K. C. Lau and C.-Y. Ng, Acct. Chem. Res. **39**, 823-829 (2006). $IE(HCCH) = 11.4006 \pm 0.0006$ eV; $IE(H_2O) = 12.61737 \pm 0.00025$ eV

T. Shimanouchi, *Tables of Vibrational Frequencies, Consolidated Vol. I.* (NSRDS-NBS 39, 1972). Of the 5 modes of HC≡CH, only the asymmetric CH stretch, σ_u ν_3, and the asymmetric HCCH bend, π_u ν_5, are IR active. In the gas-phase ν_3 HCCH is observed at 3294.9 cm^{-1} and 3281.9 cm^{-1} and is split by a Darling-Dennison resonance (DDR) of 13 cm^{-1}. In an Ar matrix, ν_3 shifts to 3302 cm^{-1} and 3288 cm^{-1}; the DDR is 14 cm^{-1} in the cryogenic matrix. The gas phase value for ν_5 is 730.3 cm^{-1} and shifts to 736.8 cm^{-1} in an Ar matrix.

V. A. Walters, S. D. Colson, D. L. Snavely, K. B. Wiberg, and B. M. Jamison, J. Phys. Chem. **89**, 3857-3861 (1985).

K. B. Wiberg, Y. Thiel, L. Goodman, and J. Leszczynski, J. Phys. Chem. **99**, 13850-13864 (1995).

We observe $\nu_1(CH_2CHO\text{-}H) = 3620$ cm-1; $\nu_5(CH_2{=}CHOH) = 1662$ cm^{-1}; and the out-of-plane wag, $\nu_{13}(CH_2{=}CHOH)$, appears as a complex doublet at 814 and 818 cm^{-1}.

M. Rodler, C. E. Blom, and A. Bauder, J. Am. Chem. Soc. **106**, 4029-4035 (1984). Vinyl alcohol was produced by pyrolysis of cyclobutanol into an argon matrix. Strong fundamental bands were found for $\nu_1(CH_2CHOH) = 3619.9$ cm^{-1}, $\nu_5(CH_2CHOH) = 1661.9$ and 1663.0 cm^{-1} (FR with $2\nu_{13}$), and $\nu_{13}(CH_2CHOH) = 813.7$ cm^{-1} with shoulders at 813 and 818 cm^{-1}.

D. L. Joo, A. J. Merer, and D. J. Clouthier, J. Mol. Spectry **197**, 68-75 (1999).

Actual frequencies that are observed are $\nu_1(CH_2CHO\text{-}H) = 3620\ cm^{-1}$; $\nu_1(CH_2CDO\text{-}H) = 3621\ cm^{-1}$; $\nu_1(CD_2CHO\text{-}D) = 2675\ cm^{-1}$; $\nu_1(CD_2CDO\text{-}D) = 2675\ cm^{-1}$. The values observed for ν_{OH} agree closely with those reported by Rodler *et al*. There are no literature values published for us to compare the frequencies of CD_2CHOD and CD_2CDOD detected here. But Rodler *et al*. find $\nu_1(CH_2CHO\text{-}D) = 2672\ cm^{-1}$.

S. M. Burnett, A. E. Stevens, C. S. Feigerle, and W. C. Lineberger, Chem. Phys. Lett. **100**, 124-128 (1983).

K. M. Ervin, J. Ho, and W. C. Lineberger, J. Chem. Phys. **91**, 5974-5992 (1989).

M. K. Gilles, W. C. Lineberger, and K. M. Ervin, J. Am. Chem. Soc. **115**, 1031-1038 (1993).

R. F. Gunion, H. Koppel, G. W. Leach, and W. C. Lineberger, J. Chem. Phys. **103**, 1250-1262 (1995).

R. F. Gunion and W. C. Lineberger, J. Phys. Chem. **100**, 4395-4399 (1996).

Y. Q. Chen, D. M. Jonas, J. L. Kinsey, and R. W. Field, J. Chem. Phys. **91**, 3976- 3987 (1989).

M. P. Jacobson and R. W. Field, J. Phys. Chem. A **104**, 3073-3086 (2000).

R. L. Hayes, E. Fattal, N. Govind, and E. A. Carter, J. Am. Chem. Soc. **123**, 641- 657 (2001).

H. Schuchma and K. J. Laidler, Canadian Journal of Chemistry **48**, 2315-& (1970).

G. da Silva and J. W. Bozzelli, J. Phys. Chem. A **110**, 13058-13067 (2006).

B. C. Shepler, B. J. Braams, and J. M. Bowman, J. Phys. Chem. A **111**, 8282–8285 (2007).

B. C. Shepler, B. J. Braams, and J. M. Bowman, J. Phys. Chem. A **112** 9344–9351 (2008).

X. P. Liu, M. L. Gross, and P. G. Wenthold, J. Phys. Chem. A **109**, 2183-2189 (2005).

Acetaldehyde could rearrange to the vinyl alcohol *via* the methylhydroxycarbene: $CH_3CHO \rightarrow [CH_3\text{-}C\text{-}OH] \rightarrow CH_2{=}CH\text{-}OH$. But this pathway would predict that the vinyl alcohol resulting from CH_3CDO would be $CH_3CDO \rightarrow [CH_3\text{-}C\text{-}OD] \rightarrow CH_2{=}CH\text{-}OD$. Fig. 6 shows that the vinyl alcohol resulting from CH_3CDO is $CH_2{=}CD\text{-}OH$. Likewise, when CD_3CHO rearranges, we observe $CD_2{=}CHOD$ and not $CD_2{=}CD\text{-}OH$.

X. Xing, B. Reed, M. K. Bahng, and C. Y. Ng, J. Phys. Chem. A **112**, 2572-2578 (2008). *IE*(CH_2CH_2) = 10.51268 ± 0.00025 eV

D. M. Golden, Int. J. Chem. Kinetics (2008).

A. M. Scheer, C. Mukarakate, D. J. Robichaud, G. B. Ellison, and M. R. Nimlos, J. Phys. Chem. A **114**, 9043-9056 (2010).

A. Streitwieser , C. H. Heathcock, and E. M. Kosower, *Introduction to Organic Chemistry*, 4th Ed. ed. (Prentice Hall, Upper Saddle River, NJ 07458, 1977). The mechanism for acid catalyzed keto-enol tautermization of CH_3CHO is described on p. 424. In aqueous solution at 300 K, K_{equi}(CH_3CHO, CH_2=CHOH) is 6 x 10^{-7}. The discussion of *E1* reactions that are catalyzed by Al_2O_3 is found on p 269.

F. A. Cotton and G. Wilkenson, *Advanced Inorganic Chemistry: A Comprehensive Text*, 2nd ed. (Wiley-Interscience, New York, 1966).

E. B. Jochnowitz, X. Zhang, M. R. Nimlos, M. E. Varner, J. F. Stanton, and G. B. Ellison, J. Phys. Chem. A **109**, 3812-3821 (2004).

A. Vasiliou, M. R. Nimlos, J. W. Daily, and G. B. Ellison, J. Phys. Chem. A **113**, 8540-8547 (2009).

E. McCormack, J. M. Gilligan, C. Cornaggia, and E. E. Eyler, (1989). *IE*(H_2) = 15.425932 ± 0.000002 eV

K. P. Huber and G. Herzberg, (1979). *IE*(D_2) = 15.4666 ± 0.0001 eV

D. Shiner, J. M. Gilligan, B. M. Cook, and W. Lichten, (1993). *IE*(HD) = 15.44465± 0.00001 eV

R. Signorell and F. Merkt, J. Chem. Phys. **110**, 2309-2311 (1999). Because of the pre-dissociation effects and Jahn-Teller dynamics of the cation, observation of CH_4^+ (m/z 16) by PIMS is not easy.

R. Signorell, M. Sommavilla, and F. Merkt, Chem. Phys. Lett. **312**, 139-148 (1999).

T. Shimanouchi, *Tables of Vibrational Frequencies. Consolidated Volume I*. (NSRDS-NBS 39, 1972). Methane has four vibrational modes but only the degenerate CH stretch, f_2 ν_3, and the degenerate deformation, f_2 ν_4, are IR active. In the gas-phase ν_3 CH_4 is observed at 3019.9 cm^{-1} and ν_4 CH_4 is found at 1306.2 cm^{-1}. These values shift in an Ar matrix to ν_3 = 3032 cm^{-1} and ν_4 = 1305 cm^{-1}. The signal from ν_4 is very intense and easy to detect in an cryogenic matrix.

P. L. Houston and S. H. Kable, Proceedings of the National Academy of Sciences of the United States of America **103**, 16079-16082 (2006).

B. R. Heazlewood, M. J. T. Jordan, S. H. Kable, T. M. Selby, D. L. Osborn, B. C. Shepler, B. J. Braams, and J. M. Bowman, Proceedings of the National Academy of Sciences of the United States of America **105**, 12719-12724 (2008).

B. R. Heazlewood, A. T. Maccarone, D. U. Andrews, D. L. Osborn, L. B. Harding, S. J. Klippenstein, M. J. T. Jordan, and S. H. Kable, Nature Chemistry **3**, 443-448 (2011).

L. B. Harding, Y. Georgievskii, and S. J. Klippenstein, J. Phys. Chem. A **114**, 765-777 (2010).

B. C. Shepler, Y. C. Han, and J. M. Bowman, Journal of Physical Chemistry Letters **2**, 834-838 (2011).

Y. C. Han, B. C. Shepler, and J. M. Bowman, Journal of Physical Chemistry Letters **2**, 1715-1719 (2011).

J. M. Bowman and B. C. Shepler, in *Annual Review of Physical Chemistry*, edited by S. R. Leone, P. S. Cremer, J. T. Groves, and M. A. Johnson (2011), Vol. 62, pp. 531-553.

L. V. Gurvich, I. V. Veyts, C. B. Alcock, and V. S. Iorish, *Thermodynamic Properties of Individual Substances*, 4th ed. (Hemisphere, New York City, 1991).

T. Ichino and J. F. Stanton, (2010).

A. Tajti, P. G. Szalay, A. G. Csaszar, M. Kallay, J. Gauss, E. F. Valeev, B. A. Flowers, J. Vazquez, and J. F. Stanton, J. Chem. Phys. **121**, 11599-11613 (2004).

B. Ruscic, J. E. Boggs, A. Burcat, A. G. Csaszar, J. Demaison, R. Janoschek, M. L. Morton, J. M. L. Martin, M. J. Rossi, J. F. Stanton, P. G. Szalay, P. R. Westmoreland, F. Zabel, and T. Berces, Journal of Physical and Chemical Reference Data **34**, 573-656 (2005). The heats of formation have been measured: $\Delta_f H_{298}(CH_3CHO) = -39.6 \pm 0.1$ kcal mol^{-1}, $\Delta_f H_{298}(CH_3CO) = -2.5 \pm 0.4$ kcal mol^{-1}, and $\Delta_f H_{298}(H) = 52.103 \pm 0.001$ kcal mol^{-1}. Consequently $DH_{298}(CH_3CO\text{-}H) = 89.3 \pm 0.4$ kcal mol^{-1}

J. B. Pedley, R. D. Naylor, and S. P. Kirby, *Thermochemistry of Organic Compounds*, 2 ed. (Chapman and Hall, New York, 1986). $\Delta_f H_0(CH_2CO)$

B. Ruscic, J. E. Boggs, A. Burcat, A. G. Csaszar, J. Demaison, R. Janoschek, J. M. L. Martin, M. L. Morton, M. J. Rossi, J. F. Stanton, P. G. Szalay, P. R. Westmoreland, F. Zabel, and T. Berces, Journal of Physical and Chemical Reference Data **34**, 573-656 (2005).

B. Ruscic, M. Litorja, and R. L. Asher, J. Phys. Chem. A **104**, 8600-8600 (2000). $\Delta_f H_{298}(CH_3) = 35.05 \pm 0.07$ kcal mol^{-1}

K. M. Ervin and V. F. DeTuri, J. Phys. Chem. A **106**, 9947-9956 (2002).

A. C. Terentis and S. H. Kable, Chem. Phys. Lett. **258**, 626-632 (1996). D_0(H-HCO) = 30328.5 ± 0.5 cm^{-1}; $\Delta_f H_0$(HCO) = 42.5 ± 0.5 kJ mol-1

K. C. Thompson, D. L. Crittenden, S. H. Kable, and M. J. T. Jordan, J. Chem. Phys. **124**, 044302 (2006).

Cool, T.A. et al. A photoionization mass spectrometer for stuides of flame chemistry with a synchrotron light source. Review of Scientific Instruments. American Institute of Physics.

Katayama, D.H., Huffman, R.E. and Obryan, C.L., *J. Chem. Phys.* **1973**, *59*, 43

Appendix A

Ketene Production

A ketene generator was designed and built after the original device by Hurd and Fieser. [1,2] The design was sent to Ace Glassware for construction. (Figure A.1)

Chromel wire was used as the heating element and the element was kept taut by a means of 20 gram weight suspended at the lower ends. A separatory funnel was connected to the boiling flask and the flask was filled half way with acetone. The acetone was then heated and refluxed from the condenser for 5 mintutes to drive out air from element chamber. Current was then applied through a variac until the heating element had a red glow(700-750°C). The ketene that was produced was trapped in a liquid nitrogen cooled trap.

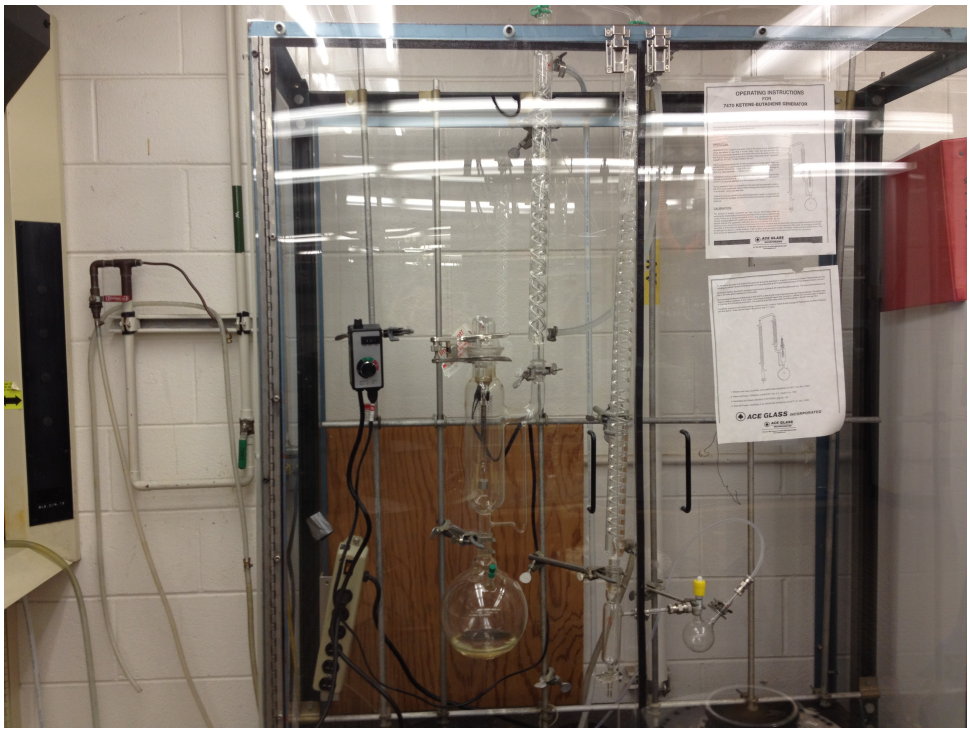

Figure A.1 Ketene generator designed and built for experiments in this thesis.

(1) Williams and Hurd, Journal of American Chemical Society, **1936** ,*58,* 965.

(2) Fieser and Fieser, Organic Chemistry, **1944**, *D.C. Heath & Co* 192.

Appendix B

Synthesis of D1-furfural: C_4H_3-CDO

The synthetic procedure for d1-furfural was modified from the original synthesis by Ramalingam and coworkers[1]. A solution of 1,3-propane dithiol (0.15 moles) and furfural(A) (0.15 moles) in 100 mL of CH_2Cl_2 was chilled to 0°C, while stirring under a nitrogen atmosphere. Once chilled $BF_3 \bullet Et_2O$ (0.15 moles) was added slowly. The reaction mixture is allowed to slowly warm to 25°C and the mixture was then stirred for 18 hours. The solution is washed with 50 mL saturated $NaHCO_3$ twice and the organic layer dried over Na_2SO_4. After filtration and evaporation of the solvent under reduced pressure, the solid formed is recrystallized from benzene. The solid, 2-(2-furyl)-1,3-dithiane (B), is a colorless liquid.

To the stirred solution of 2-(2-furyl)-1,3-dithiane 220 mL of THF is added, under a nitrogen atmosphere, cooled to -78°C. Over a period of an hour a solution of n-butyllithium in hexane was slowly added. After the mixture stood for 6 hours at a temperature of -78°C, 20 mL of deuterium oxide was added and the mixture was slowly warmed to 25°C. The LiOD salt was removed by decantation and the THF was removed under reduced pressure. The residue was then dissolved in 350 mL diethyl ether and washed twice with 50 mL an aqueous solution of NH_4OH/NH_4Cl, water and dried $MgSO_4$. The ether was removed under reduced pressure yielding a reddish oil which solidified overnight. The solid was then dissolved in acetone and treated with charcoal. After filtering and removing the solvent yields the white needle like product 2-(d)-2-(2-furyl)-1,3-dithiane(C) was isolated.

A methanol-water solution was used to dissolve product 2-(d)-2-(2-furyl)-1,3-dithiane. After 2-(d)-2-(2-furyl)-1,3-dithiane was dissolved, mercuric oxide (40.7 mmols) and mercuric chloride (90.4 mmols) were slowly added under a nitrogen atmosphere. A white precipitate formed and the mixture was heated to reflux for 4 hours, still under nitrogen atmosphere, and then cooled to 25°C. The solid was then removed by suction and the filtrate was extracted with dichloromethane. The organic layer was washed consecutively with first a saturated aqueous ammonium acetate solution followed by a brine solution. After drying over Na_2SO_4, and removal of the solvent under reduced pressure, the final product, d1-furfural (D), was isolated as a yellowish liquid.

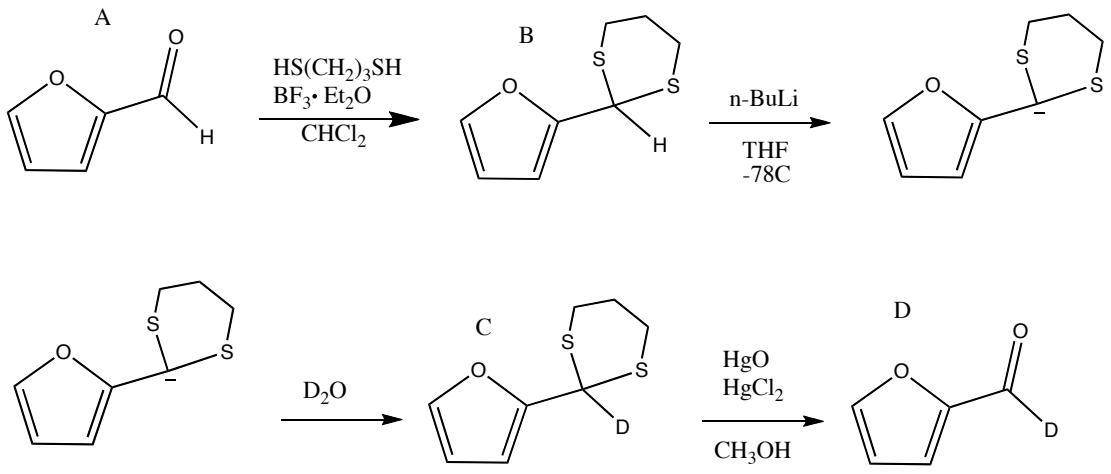

Figure B.1 d1-Furfural Synthesis

(1) Ramalingam, K., Nanjappan, P., Kalvin, D.M. and Woodard R.W. *Tetrahedron* **1988**, *44*, 5597.

Appendix C

Synthesis of Azomethane

Azomethane was prepared using standard methods.[1] Dimethylhydrazine hydrochloride was dissolved in the minimum amount of water, and was neutralized by the addition of potassium hydroxide pellets. The resulting solution was added dropwise over two hours, under a stream of nitrogen to a stirred suspension of mercuric oxide in water. The nitrogen passed though the reaction vessel, through a water cooled condenser, and into a glass trap connected to a glass manifold. The gas traps were kept in a dry ice/ethanol bath at -78°C. After all the dimethylhydrazine was added the mixture was stirred for an hour and then heated to 50°C for 30 minutes. The mixture was then heated to 60°C for another half hour. The glass traps were cooled and isolated from the reaction vessel. The white solid formed in the traps was transferred by trap to trap distillation via a short drying tube filled with drierite. The white solid, azomethane (CH_3-N=N-CH_3), was stored in the chemical freezer.

The purpose in making azomethane was to create clean source of methyl radical:

$$CH_3\text{-}N{=}N\text{-}CH_3 \rightarrow 2CH_3 + N_2$$

The matrix IR spectrum in Figure C.1 provides evidence that the thermal decomposition of azomethane produces methyl radical.

CH_3 free radical can rotate in an argon matrix at temperatures near 14 K with only minor perturbations of its low-J rotational levels from those characteristic of the gas phase.

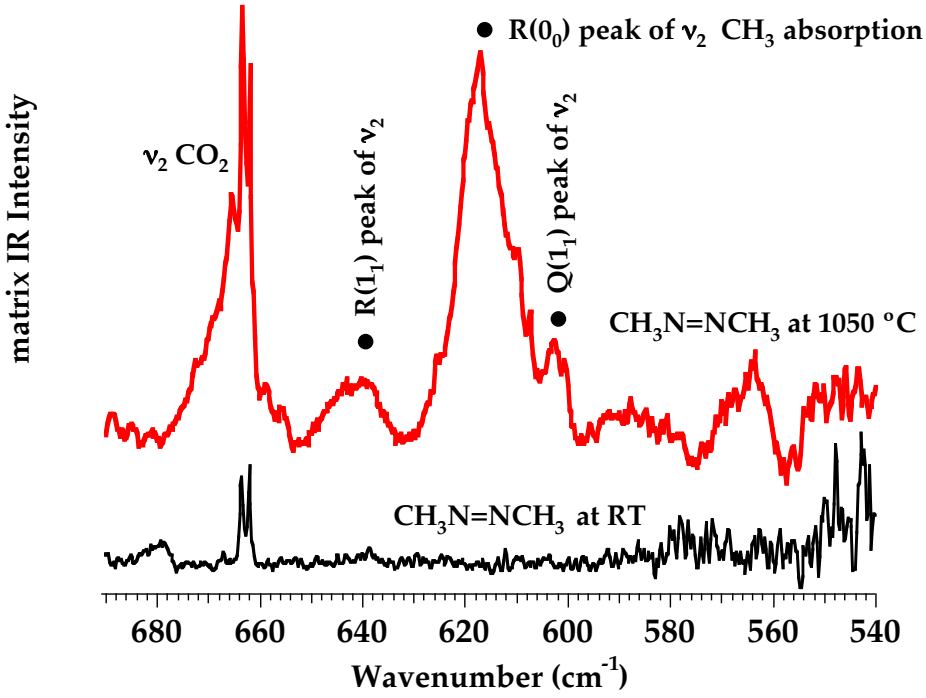

Figure C.1 Matrix IR spectrum of heated azomethane. The black trace is azomethane at room temperature and the red trace with observable features from CH_3 is azomethane heated to 1050°C. The methyl radical assignments are based on those by Jacox.[2]

(1) Renaud, R., Leitch, L. *Can. J. Chem.* **1954**, *32*, 545.

(2) Milligan, D.E.; Jacox, M.E., *J. Chem. Phys.,* **1967**, 47, 5146.

Appendix D

Quantification of ALS Data

Beer's law for photoionization

$$A + \hbar\omega \rightarrow A^+ + e^-$$

$I(\omega)$ = transmitted radiation/photons sec^{-1}

$I_0(\omega)$ = incident radiation/photons sec^{-1}

n_A = density of target species/molecules cm^{-3}

$\sigma_A(\omega)$ = photoionization cross section/cm^2

ℓ = path length/cm

$$I(\omega) = I_0(\omega)\, e^{-n_A \sigma_A(\omega)\ell} \qquad (1)$$

Since the VUV radiation is photoionizing the targets, the ion current, J^+, is the difference between the incident and transmitted radiation.

$$J^+ = (I_0 - I) = (I_0 - I_0\, e^{-n\sigma\lambda}) \qquad (2)$$

Typical radical densities are roughly 1 mTorr and the path length is about ½ cm. Cross sections for radicals are approximately 5 x 10(-18) cm^2. Consequently ($n\sigma\lambda$) is on the order of (3 x 10^{13} x 5 x 10^{-18} x 0.5) ≅ 7 x 10^{-5}. Thus: $e^{-n\sigma\lambda} \cong 1 - n\sigma\lambda$

For the i^{th} species

$$J_i^+ = n_i \sigma_i(E_i) \ell\, I_0(E_i) \qquad (3)$$

If we normalize the signals over a definite interval, the ion signal S_i^+ is related to the incident photon power, Φ_0, by an empirical constant, C.

$$S_i^+ = C\, n_i \sigma_i(E_i) \Phi_0(E_i) \tag{4}$$

The photon power, Φ_0, given in photons sec^{-1} is derived from the photodiode current measured at the terminal end. QE is the quantum efficiency of the photodiode as given by the company (NIST calibration).

$$\Phi_{o[ph/s]}(E_i) = \frac{PhotoDiode_{[Amp=C/s]}(E_i)}{QE_{[e/ph]}(E_i) \cdot e_{[C/e]}} \tag{5}$$

A mass discrimination factor, D_i, is needed to correct for imperfect transmission through the apparatus.

$$S_i^+ = C\, (D_i\, n_i) \sigma_i(E_i) \Phi_0(E_i) \tag{6}$$

Solving for the number density at the laser/beam interaction region:

$$n_i = S_i^+ [C\, D_i\, \sigma_i(E_i) \Phi_0(E_i)]^{-1} \tag{7}$$

The number density at the end of the reactor, n^o_i, is required rather than n_i. These two values are related by a complex function that depends on the properties of the flow reactor such as the nature of the buffer gas, the temperature, T_L, and pressure, P_L. This complex function will be called $F(T_L,P_L)$.

Consequently: $F(T_L,P_L)\, n^o_i = n_i$; expression (6) becomes:

$$n^o_i = S_i^+ [C\, F(T_L,P_L)\, D_i\, \sigma_i(E_i) \Phi_0(E_i)]^{-1} \tag{8}$$

The strategy is to avoid measurement of absolute n^o_i values but to examine ratios. To quantify the decomposition pathways of acetaldehyde, consider:

$$CH_3CHO + \Delta \rightarrow CH_3 + H + CO \quad (9a)$$

$$CH_3CHO + \Delta \rightarrow CH_2{=}C{=}O + H_2 \quad (b)$$

$$CH_3CHO + \Delta \rightarrow [CH_2{=}CHOH] \rightarrow HC{\equiv}CH + H_2O \quad (c)$$

We must measure the populations, n^o_i, at the exit of the μtubular reactor:

$$n^o_{CH3CHO} = S_{44}^{+}\,[C\,F(T_L,P_L)\,D_i\,\sigma_{CH3CHO}(E_i)\Phi_0(E_i)]^{-1} \quad (10a)$$

$$n^o_{CH2=CHOH} = S_{44}^{+}\,[C\,F(T_L,P_L)\,D_i\,\sigma_{CH2=CHOH}(E_i)\Phi_0(E_i)]^{-1} \quad (b)$$

$$n^o_{CH3} = S_{15}^{+}\,[C\,F(T_L,P_L)\,D_i\,\sigma_{CH3}(E_i)\Phi_0(E_i)]^{-1} \quad (c)$$

$$n^o_{CH2CO} = S_{42}^{+}\,[C\,F(T_L,P_L)\,D_i\,\sigma_{CH2CO}(E_i)\Phi_0(E_i)]^{-1} \quad (d)$$

$$n^o_{HCCH} = S_{26}^{+}\,[C\,F(T_L,P_L)\,D_i\sigma_{HCCH}(E_i)\Phi_0(E_i)]^{-1} \quad (e)$$

Ratios of decomposition products are:

$$\frac{n^o_{CH3}}{n^o_{CH3CHO}} = \frac{S^+_{15}}{S^+_{44}}\left[\frac{D_{44}\sigma_{CH3CHO}\Phi_{CH3CHO}}{D_{15}\sigma_{CH3}\Phi_{CH3}}\right] \quad (11a)$$

$$\frac{n^o_{CH2CO}}{n^o_{CH3CHO}} = \frac{S^+_{42}}{S^+_{44}}\left[\frac{D_{44}\sigma_{CH3CHO}\Phi_{CH3CHO}}{D_{42}\sigma_{CH2CO}\Phi_{CH2CO}}\right] \quad (11b)$$

$$\frac{n^o_{HCCH}}{n^o_{CH3CHO}} = \frac{S^+_{26}}{S^+_{44}}\left[\frac{D_{44}\sigma_{CH3CHO}\Phi_{CH3CHO}}{D_{26}\sigma_{HCCH}\Phi_{HCCH}}\right] \quad (11c)$$

A difficulty will be the isomerization of acetaldehyde to vinyl alcohol as the μtubular reactor is heated: $CH_3CHO \rightleftharpoons CH_2{=}CHOH$. We must estimate the fraction of S_{44}^+ due to CH_3CHO or CH_2CHOH and $\sigma_{CH2CHOH}$ will be required in addition to σ_{CH3CHO}. Dissociative ionization of both CH_3CHO and $CH_2{=}CHOH$ produce the acetyl cation, CH_3CO^+, at m/z 43. Consequently these ions must be considered along with m/z 44.